Thermoresponsive Materials for Dehumidification in Air Conditioning

by

Ashish Rana

A Dissertation Presented in Partial Fulfillment
of the Requirements for the Degree
Doctor of Philosophy

Approved October 2023 by the
Graduate Supervisory Committee:

Robert Wang, Chair
Matthew Green
Ryan Milcarek
Liping Wang
Patrick Phelan

ARIZONA STATE UNIVERSITY

December 2023

ABSTRACT

Air conditioning is a significant energy consumer in buildings, especially in humid regions where a substantial portion of energy is used to remove moisture rather than cool the air. Traditional dehumidification methods, which cool air to its dew point to condense water vapor, are energy intensive. This process unnecessarily overcools the air, only to reheat it to the desired temperature.

This research introduces thermoresponsive materials as efficient desiccants to reduce energy demand for dehumidification. A system using lower critical solution temperature (LCST) type ionic liquids (ILs) as dehumidifiers is presented. Through the Flory-Huggins theory of mixtures, interactions between ionic liquids and water are analyzed. LCST ionic liquids demonstrate superior performance, with a coefficient of performance (COP) four times higher than non-thermoresponsive desiccants under similar conditions. The efficacy of ionic liquids as dehumidifiers is assessed based on properties like LCST temperature and enthalpic interaction parameter.

The research also delves into thermoresponsive solid desiccants, particularly polymers, using the Vrentas-Vrentas model. This model offers a more accurate depiction of their behaviors compared to the Flory-Huggins theory by considering elastic energy stored in the polymers. Moisture absorption in thin film polymers is studied under diverse conditions, producing absorption isotherms for various temperatures and humidities. Using temperature-dependent

interaction parameters, the behavior of the widely-used thermoresponsive polymer (TRP) PNIPAAm and hypothetical TRPs is investigated. The parameters from the model are used as input to do a finite element analysis of a thermoresponsive dehumidifier. This model demonstrates the complete absorption-desorption cycle under varied conditions such as polymer absorption temperature, relative humidity, and air speed. Results indicate that a TRP with enhanced absorption capacity and an LCST of 50℃ achieves a peak moisture removal efficiency (MRE) of 0.9 at 75% relative humidity which is comparable to other existing thermoresponsive dehumidification systems. But other TRPs with even greater absorption capacity can produce MRE as high as 3.6. This system also uniquely recovers water in liquid form.

DEDICATION

To my parents, for always believing in me, loving me unconditionally, and instilling in me the right values. This work is a testament to the strength of your teachings and the depth of your love.

ACKNOWLEDGMENTS

First and foremost, I would like to express my deepest gratitude to my advisor, Robert Wang, for their unwavering support, guidance, and mentorship throughout my PhD journey at Arizona State University. His expertise and insights have been invaluable, and I am truly fortunate to have had the opportunity to work under his tutelage. I would also like to extend my heartfelt thanks to the esteemed members of my committee. Your feedback, constructive criticism, and encouragement have been instrumental in shaping my research and ensuring its success.

A special mention to my group mates, Zhongyong Wang, Yanan Zhang, Wilson Kong, Aastha Uppal, Ming-Hsien Sun, Prathamesh Vartak, Najam Hasan, Shreyas Kanitkar, Rohit Gandhi for making this journey enjoyable and memorable. I would also like to extend my thanks to Brad Grim from Dr Matt Green's lab for helping me with experiments.

To my parents and siblings, words cannot express how grateful I am for your love, patience, and unwavering belief in my capabilities. You have been my rock, providing emotional and moral support throughout this endeavor. Lastly, to my friends, both within and outside the confines of the university, thank you for being my sounding board, for the laughter, the distractions, and for reminding me that there's a world outside the lab. Your friendship has been a source of strength and joy. In conclusion, this work stands as a testament to the collective efforts, support, and faith of all the individuals mentioned above. I am deeply humbled and eternally grateful.

TABLE OF CONTENTS

Page

LIST OF TABLES

LIST OF FIGURES

Figure Page

Figure Page

Figure Page

Figure Page

Figure Page

1. INTRODUCTION AND LITERATURE REVIEW

1.1. Motivation

Air conditioning is one of the most important energy consumers in buildings today. When we talk about comfort due to air conditioning, we often talk about the temperature read by the thermometer. But another component that contributes to comfort is the amount of moisture in the air or humidity. Therefore, a hot summer day in Miami, Florida and Tempe, Arizona might feel different even when the temperature is the same. Dry air feels more comfortable because it helps us cool through the sweat much more easily than humid air. The two factors associated with air comfort are its temperature (sensible load) and relative humidity (latent load). Figure 1-1 shows the U.S. average residential air-conditioning expenditures by climate region for the year 2015. It categorizes different regions of the U.S. based on climate—hot-humid, mixed-dry/hot-dry, mixed-humid, very cold/cold, and marine. Notably, the hot-humid regions stand out with the highest expenditure at 27% which is 10% higher than the next highest for hot-dry regions. Humid regions have higher air-conditioning expenditures because the combined heat and humidity increase the need for cooling. The air conditioners in these areas also work to reduce moisture, consuming more energy in the process.

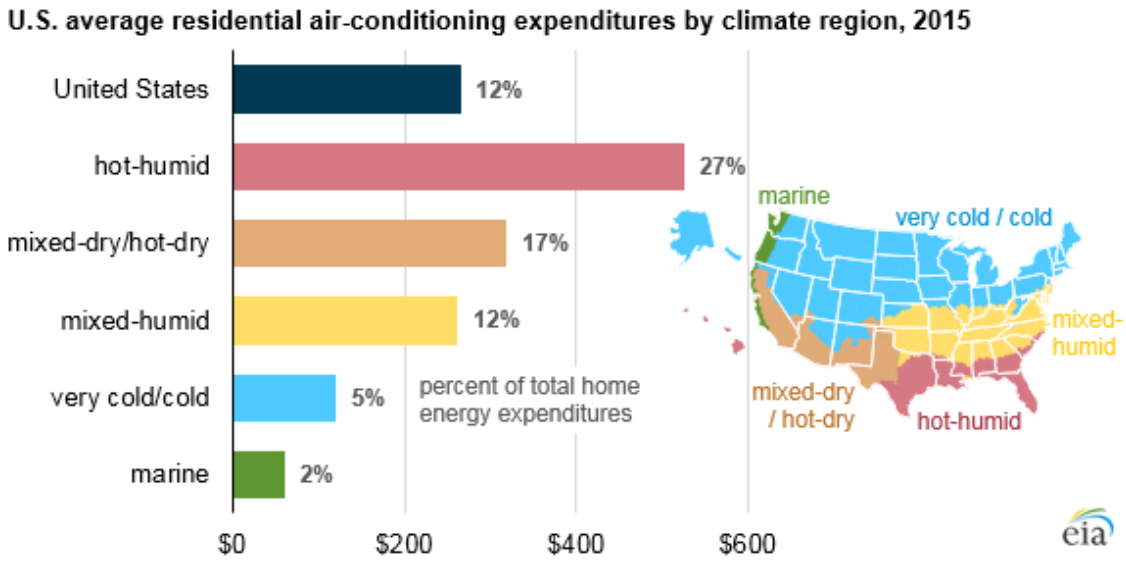

Figure 1-1: US average residential air-conditioning expenditure by climatic region for 2015 (Reprinted with permission from U.S. Energy Information Administration, 2015 Residential Energy Consumption Survey[1])

The most commonly used method of air conditioning is the vapor compression air conditioning (VCAC) system that delivers air in one single step with the air cooling and the moisture removal happening at the same time. The VCAS uses a low boiling point liquid as the refrigerant to remove heat from one region to another. The refrigerant used in the air conditioning have a global warming potential (GWP) of 10,000 which means that they will generate 10,000 times more heat into the atmosphere over a period of 100 years[2,3]. Air conditioning is also a major contributor to greenhouse gases in the atmosphere [4].

Another problem with vapor compression system is that it does not offer very good humidity control since both the cooling and dehumidification happen in one single step. The air is first cooled to its dew point to remove the moisture by condensation on the

cooling coils and then heated back to the desired temperature at which air needs to be delivered. This warrants a system that can control dehumidification (latent load) and the cooling (sensible load) independently.

The other method that can be used to control the moisture is by using desiccants to absorb water from the air. This method not only eliminates the need to reheat the air (in the VCAC system) but also enables the use of renewable sources like solar energy for evaporative cooling for the sensible part for reducing the air temperature. The desiccant needs to be regenerated which is achieved by heating it with a heat source. In the dehumidification system, the heat source can be waste heat or from renewable sources like solar to regenerate the desiccant material. But most of the desiccants require a massive amount of energy to remove the absorbed water from the desiccant because the water needs to be boiled off from the desiccant solution. This presents a potential for the reduction of this regeneration heat. This can be potentially achieved by using thermoresponsive desiccants such as some hydrogel polymers (like PNIPAAM polymer) and some ionic liquids. One of the characteristics that some of these thermoresponsive desiccants possess is called lower critical solution temperature (LCST) which is causing a sudden change in miscibility with water above this temperature. It can be defined as the temperature which causes the behavior of the polymer/ ionic liquid to become hydrophobic from hydrophilic. PNIPAAM polymer is a solid sponge that can change its behavior from hydrophilic to

hydrophobic above LCST. Ionic liquids are bulky salts that exist as liquids and LCST ionic liquids (IL) separate into two-phase solutions with water-rich and IL-rich phases above LCST. In this work, we have studied these polymer and ionic liquids as air dehumidifier to potentially prove why they work better than vapor compression air conditioning systems and traditional desiccants.

1.2. Background on Air Dehumidification Techniques

1.2.1. Vapor Compression Air Conditioning System

A vapor compression refrigeration compression of mainly four components as shown in Figure 1-2. The air that needs to be cooled/dehumidified enters the evaporator at high temperature and high relative humidity and gives off its heat to the refrigerant (low boiling point fluid). The refrigerant evaporates and cools the cooling coils by giving off its latent heat of vaporization. The temperature of the cooling coils is low enough to condense the water vapor from the air as well as cooling the incoming air sensibly. So, air temperature is adjusted to the desired temperatures by heating the dehumidified air which is then delivered into the space. So, air leaves the evaporator as cold and dehumidified and refrigerant leaves as vapor. To regenerate the refrigerant, it is passed through a compressor that raises its pressure which can make it easier to condense in the condenser. The low temperature, high-pressure refrigerant is passed through an expansion valve to lower its

pressure for the evaporation in the evaporator.

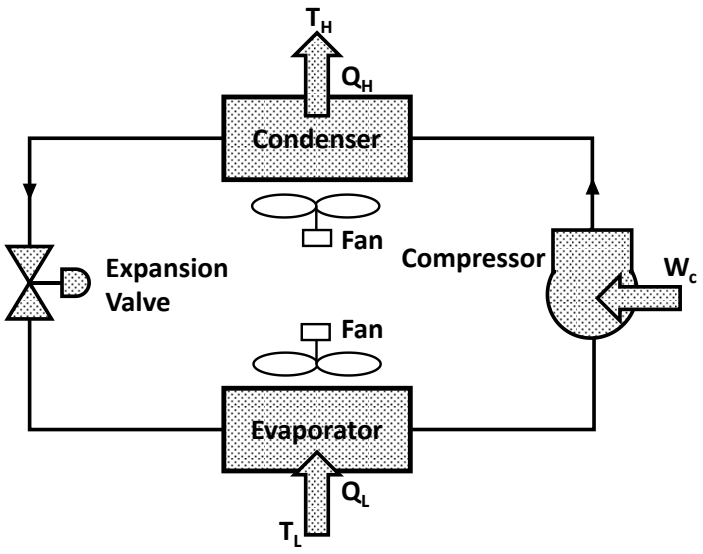

Figure 1-2: A simple schematic of vapor compression refrigeration cycle

The cooling and dehumidification process of air in the evaporator is shown in the psychrometric chart in Figure 1-3. If the incoming air is at 35 ℃ and RH=75% (Point 1) and the desired air temperature is 25 ℃ and RH=50% (Point 4), then there is no direct path from the 1 to 4 using a condensation method. Therefore, to remove the moisture, the air is cooled to its dew point where relative humidity becomes 100% (Point 2). Process 2-3 follows the RH=100% line to remove the moisture from the air. This moisture removal process overcools the air to a temperature much lower than the desired temperature and therefore needs to be reheated to the desired temperature at 4. It is clear from Figure 1-3 that latent load (dehumidification process causes the significantly greater enthalpy change than the sensible load (Cooling + reheating process). Therefore, to reduce the energy

required for dehumidification, we need to find better methods that are described in the following sections.

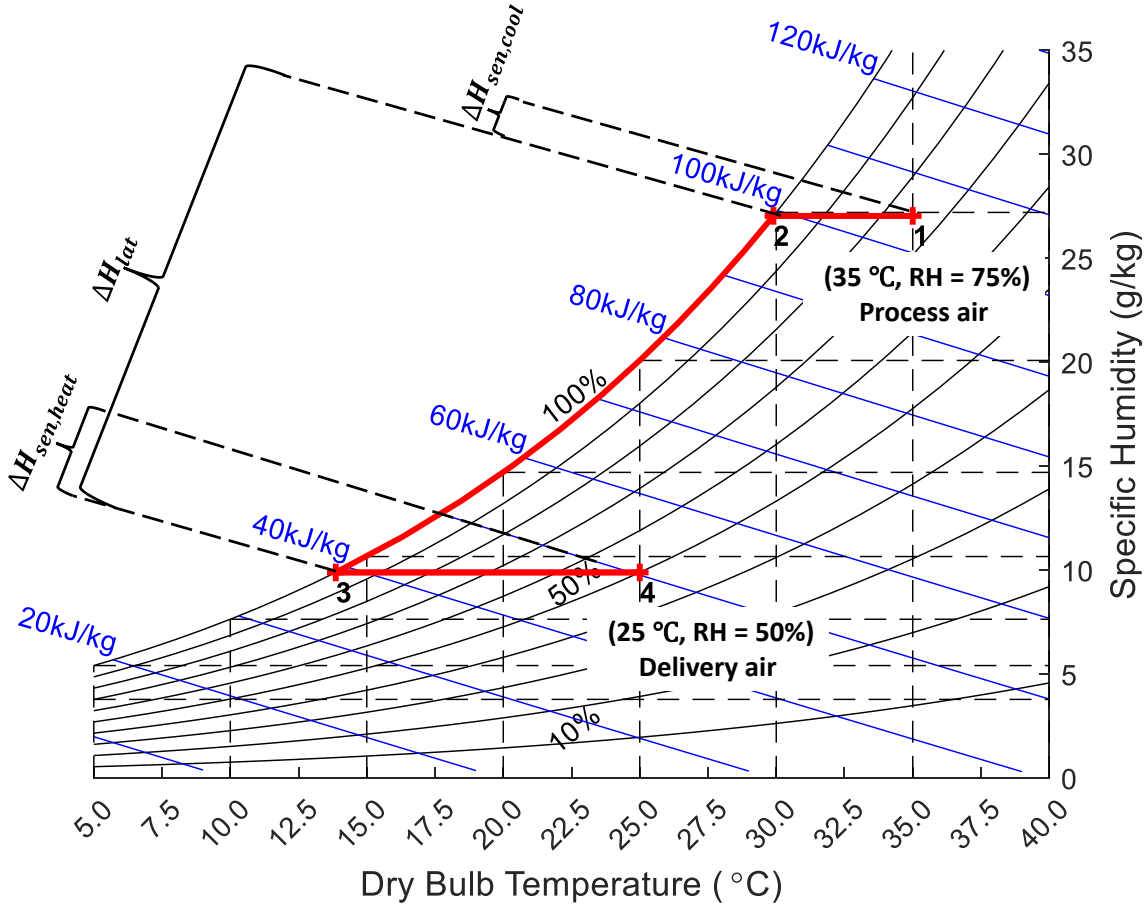

Figure 1-3: Psychrometric chart showing cooling/dehumidification process in Vapor compression air conditioning (VCAC) system.

1.2.2. Desiccant Dehumidification

Desiccant dehumidification is a process in which a hygroscopic substance called a desiccant removes moisture from the air. The absorption process in desiccants is caused by the difference in the concentration of the water vapor in the air and desiccant or the

difference in the vapor pressure of water between air and the desiccant surface. Figure 1-4 shows the different processes involved in dehumidification and the regeneration of the desiccant. Absorption (1-2) happens at low temperatures because of a higher affinity for water at low temperatures. The desorption process, also known as regeneration (2-3) involves heating the desiccant solution to remove the absorbed water and the final step is to cool the desiccant so it can be reused again to absorb more water from air. The desiccant may be liquid or solid. Typical solid desiccants include material such as silica gel, activated charcoal, zeolites, *etc*. Typical liquid desiccants include aqueous solutions of lithium chloride (LiCl), triethylene glycol (TEG), lithium bromide, and calcium chloride.

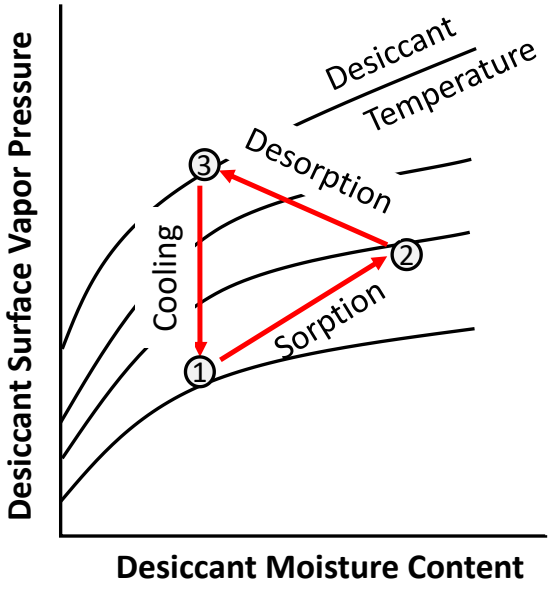

Figure 1-4: Desiccant dehumidification and regeneration process

1.2.2.1. Solid Desiccant Dehumidification Systems:

Different technologies are employed to use solid desiccants to remove water vapor from air. Some of the desiccant dehumidification techniques are described below:

A. Rotary Desiccant (Solid) Dehumidifiers:

One of the oldest techniques of dehumidification is the use of rotating desiccant wheel impregnated with a desiccant. The wheel rotates slowly through the air stream to be dehumidified, as well as through a separate regeneration air stream which is heated to release moisture from the desiccant.

One of the earliest examples of this was shown in a report for the Department of Energy by Shelpuk and Hooker in 1979.[5] This report describes an axial flow desiccant rotor that consists of a cylinder with air channels with walls coated with solid desiccant material. A typical desiccant rotor is divided into two with one half of the wheel receiving the process air and the other half receiving the regeneration air as is shown in Figure 1-5. The process air is humid air that is dehumidified by absorbing moisture from it. The regeneration stream delivers the heated air to vaporize the absorbed moisture from the other side of the wheel. The wheel is rotated slowly so that the entire cylinder can be used for absorption and the other half be regenerated for fresh absorption.

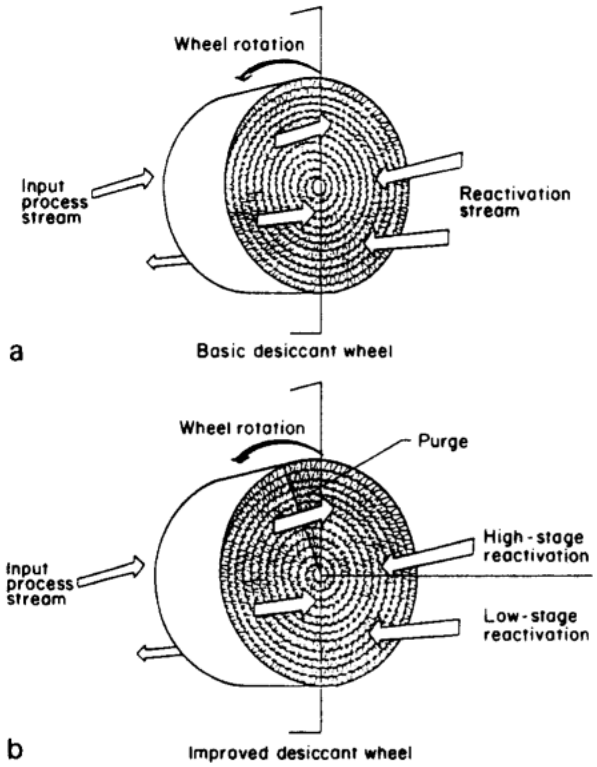

Figure 1-5: Rotary axial flow dehumidifier (a) Basic desiccant wheel (b) Improved desiccant wheel (Reprinted with Permission from Ref [5],Copyright 1979 International Journal of Refrigeration).

The most common solid desiccant used in many studies is the silica-gel as desiccant wheel coupled with a sensible heat exchanger and evaporative coolers[6–8]. Typically for these systems the dehumidification COP was under 1 and it was higher for lower regeneration temperature if the air for other parameters being the same.

Al-Alili et al.[9] have used a desiccant material called Functional Adsorbent Material Zeolite 01(FAM-Z01) that can have an S-shaped isotherm as shown in Figure 1-6. Since the change in relative humidity can easily alter the absorption capacity at lower relative humidities, there is no need to heat the regeneration air to a very high temperature to desorb

the absorbed water. They were able to obtain the highest latent coefficient of performance for the desiccant wheel of about 1.3 which was obtained for the lowest regeneration temperature case.

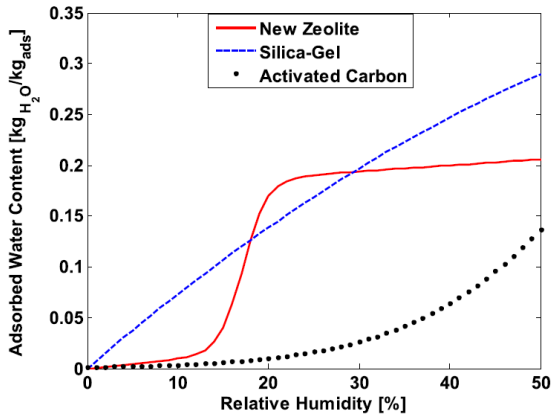

Figure 1-6: Isotherms of different adsorbents at 25 °C (Reprinted with Permission from Ref [9], Copyright 2015 Energy).

B. Desiccant Coated Heat Exchanger:

Desiccant-coated heat exchangers (DCHEs) were made to enhance dehumidification and thermal efficiency, containing fins coated with desiccants like silica gel and polymer materials, and using aluminum and copper tubes for cooling fluid circulation as seen in Figure 1-7. Studies, such as those by Ge et al.[10], highlight that silica gel coatings on these exchangers achieve optimal dehumidification at a regeneration temperature of 70°C. Weixing et al[11] designed a new cross-cooled dehumidifier offering a 12.4% improvement in moisture removal efficiency.

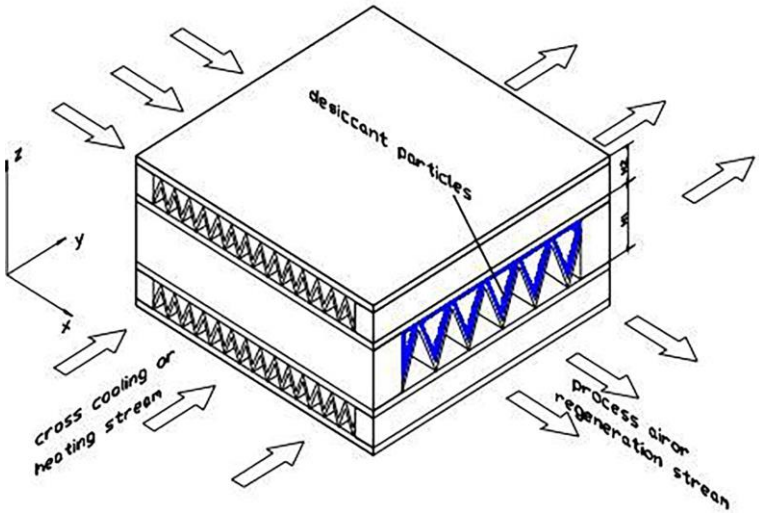

Figure 1-7: Desiccant-coated cross-cooled compact dehumidifier (Reprinted with Permission from Ref[11], Copyright 2008 Applied Thermal Engineering)

1.2.2.2. Liquid Desiccant Dehumidification Systems

Although solid desiccant systems, have the advantages of their design simplicity, simple regeneration using dry air, and lower energy use in drying processes, liquid desiccant systems have the upper hand in terms of higher absorption capabilities and the benefit of functioning effectively at lower regeneration temperatures.[12] One of the earlier research projects on liquid desiccants was done by Peng and Howell[13] who analyzed a liquid desiccant dehumidification system for a warehouse application. They installed a flat plate solar collector on the roof of the warehouse to use solar energy for the regeneration of the liquid desiccant which was a triethylene glycol-water solution in this case. The mathematical model simulation results showed that the proposed solar-powered liquid desiccant system offered significant savings in operating cost over a conventional

dehumidification system for long term warehouse storage applications.

Ahmed et al.[14] used classical thermodynamics to study the vapor pressure of the liquid desiccant with lithium chloride as the desiccant. They found that predicted values for lithium chloride agreed well with the experiments. They also tested the mixture of lithium chloride and calcium chloride and found that vapor pressure of calcium chloride to be higher making it a poor liquid desiccant.

Gandhidasan[15] developed a simple model using liquid desiccant through dimensionless vapor pressure and temperature difference ratios. They derived an expression using these ratios to predict the water condensation rate from the air to the desiccant solution in terms of known operating parameters. The model predictions were in good agreement with a reliable set of experimental data available from the literature. The effects of the desiccant-to-water heat exchanger effectiveness and cooling water inlet temperature on the performance of the dehumidifier are also studied and the results are presented in their paper. Some of the liquid desiccant systems are summarized below.

A. Spray tower liquid dehumidification system

The spray tower technique is used with liquid desiccants because it is easy to design and operate, and there is a small pressure drop across the tower. It works by spraying a liquid desiccant into small droplets from the top using nozzles, while humid air flows in

from the bottom as shown in Figure 1-8. This kind of design facilitates greater contact between the air and the solution. But its main drawback is that it tends to carry a lot of solution droplets with air which can be harmful to human health. Moreover, these towers have low efficiency[16]. Kumar et al.[17] addressed this issue by creating a spray tower that includes a "zero carryover area" at the top, effectively preventing the liquid from being carried away with the air. They did so by adding a mesh at the top of the tower to stop liquid desiccant carryover.

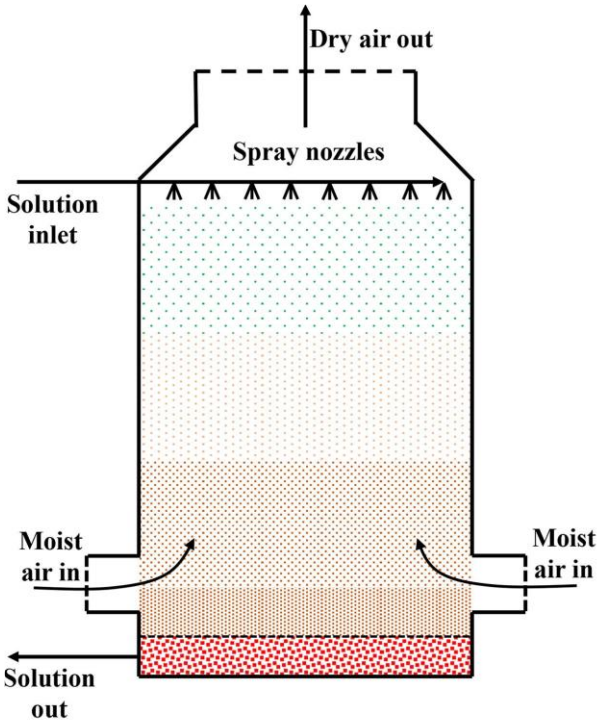

Figure 1-8: Schematic of a liquid desiccant dehumidification using spray tower (Reprinted with Permission from Ref[16], Copyright 2021 International Journal of Energy Research)

B. Packed Bed Tower Liquid Dehumidification System

A packing-bed tower is designed to maximize the contact area and contact time between air and solution. This tower is filled with packing materials that increase the interaction between the air and the liquid desiccant. The desiccant solution is sprayed at the top over the packing using nozzles and air enters from bottom to interact with desiccant over the packing as can be seen in Figure 1-9. Although it improves air and desiccant interaction, the air pressure drop is increased due to the packing. A more structured packing design is used to reduce the pressure drop and also enhance the dehumidification capacity of the tower.[18–20] Martin and Goswami[21] experimentally studied the heat and mass transfer between a liquid desiccant (triethylene glycol) and air in a packed bed regenerator using high liquid flow rates. They found a good agreement was shown to exist between the experimental findings and the predictions from finite-difference modelling. The design variables like air flow rate and the humidity ratio, the desiccant temperature and concentration and the packed bed height were found to have the greatest impact on the performance of the regenerator. The liquid flow rate and the inlet air temperature did not have a significant effect on the regenerator performance.

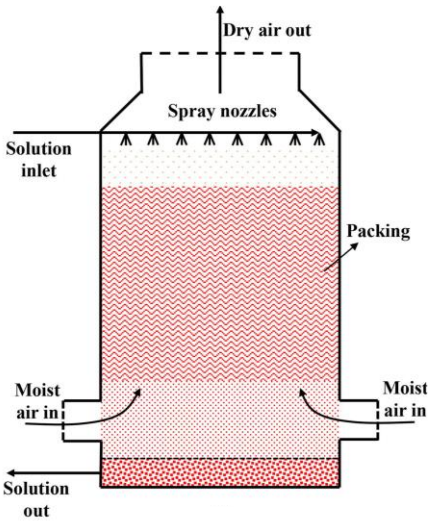

Figure 1-9: Schematic of a packing-bed tower type dehumidifier (Reprinted with Permission from Ref[16], Copyright 2021 International Journal of Energy Research)

C. Falling Film Tower Liquid Dehumidification System.

In the falling film dehumidifier design, a desiccant solution flows down a plate or tube while air passes between these surfaces, contacting the thin film of desiccant solution as can be seen in Figure 1-10. They can be in different configurations- cross flow type, parallel flow or counter flow type defined by the relative flow direction between the desiccant and air. The advantages of such a system are the low pressure drop compared to packed-bed type systems and smaller risk of carry over liquid desiccant compared to spray tower type dehumidification system. Ali et al.[22] conducted numerical comparisons between counter and parallel airflow in relation to the desiccant film and found parallel flow to be more effective for dehumidification and counterflow better for regenerating the desiccant at low

flow rates. Qi et al.[23] developed a model to estimate the wetted area of the falling film and found that decreasing the contact angle and film thickness can expand this area, enhancing the process. Another study by Dong et al[24] also concluded that wettability improvement was boosted dehumidification efficiency by increasing the soaking area and reducing film thickness.

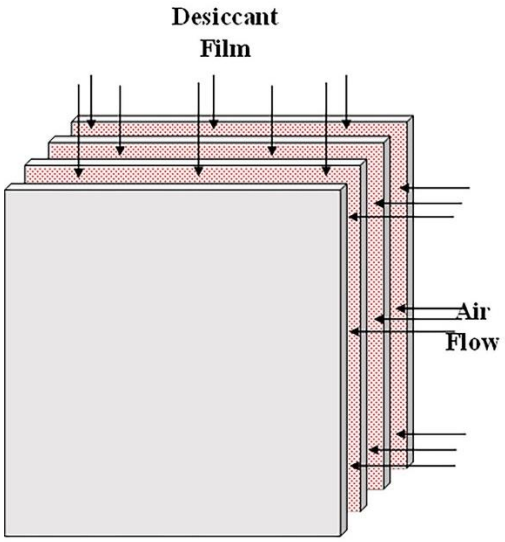

Figure 1-10: Schematic diagram of flat plate falling film dehumidifier (Reprinted with Permission from Ref[12], Copyright 2023 Energy and Buildings)

1.2.3. Membrane Dehumidification

Apart from solid and liquid desiccant dehumidification systems, a new form of technology using membrane has garnered interest. In membrane dehumidification system, the water vapor permeates through the membrane while air (oxygen and nitrogen molecules) is blocked. The advantages of this system over desiccant dehumidification it that it does

not generate any heat during the permeation of water vapor through the membrane, so this process is also called isothermal drying[25]. It also does not require the air to be cooled to its dew point like in vapor compression system[26]. The dehumidification process is illustrated in in Figure 1-11 where water vapor from humid air on one side of membrane is removed by applying vacuum on the other side of the membrane and the air molecules are too big to pass through the membrane and it leaves as dry air.

The two factors influencing the dehumidification performance are permeate pressure and air velocity. The driving force for water vapor transfer is this vacuum pressure applied on the permeate side to create the pressure differential. And this is often dependent on two membrane properties called permeability and selectivity. Permeability indicates the volume of water vapor that can pass through the membrane per unit area per unit driving force. A more permeable membrane can move more water through it per unit driving force. On the other hand, selectivity, the ratio of water vapor to other gases that the membrane allows through. A membrane with higher selectivity will enable more water vapor to pass into the permeate side[27,28].

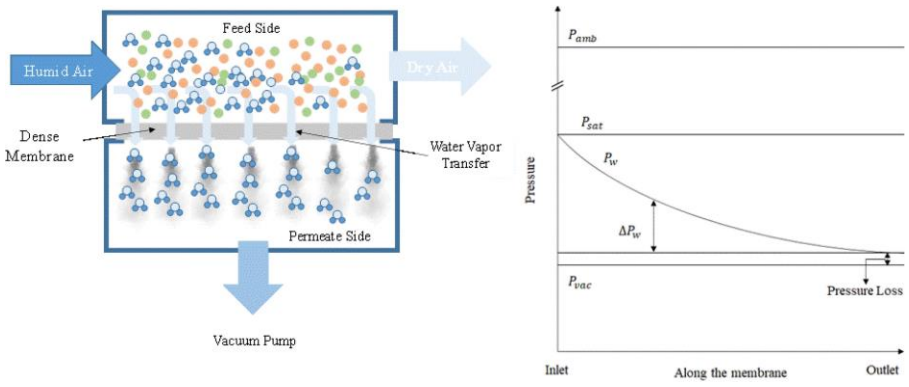

Figure 1-11: General membrane dehumidification process and pressure variation along the membrane (Reprinted with Permission from Ref[12], Copyright 2023 Energy and Buildings)

The following table compares the above-described dehumidification technologies on various parameters:

Table 1-1: Table comparing different types of dehumidification techniques.

Parameter	**Refrigeration Dehumidification**	**Solid-Desiccant Dehumidification**	**Liquid-Desiccant Dehumidification**	**Membrane Dehumidification**
Operating Principle	Condensation on cold surface	Adsorption on solid material	Absorption into hygroscopic liquid	Selective permeation through a membrane
Energy Efficiency	Moderate	Moderate to high (can utilize low-grade waste heat for regeneration)	Moderate to high (can utilize low-grade waste heat for regeneration)	High
Humidity Control	Good (can reach moderate relative humidity levels)	Excellent (can reach very low relative humidity levels)	Excellent (can reach very low relative humidity levels)	Good to excellent (depends on membrane type and system design)
Maintenance Requirements	Moderate (coil cleaning, refrigerant management)	Moderate (desiccant replacement or regeneration)	Moderate to high (potential for corrosion)	Low (membrane durability)
Cost	Low to moderate	Moderate	Moderate to high	High
Installation Complexity	Low to moderate	Moderate	High	High
Global Warming	High	Low (Depends on regeneration energy	Low (Depends on regeneration	Low (Depends on pump operation

Potential		source)	energy source)	energy source)

We have summarized the existing dehumidification techniques in the above table. based on the summary, we see that traditional refrigeration system although simple, is not very energy efficient as well as it poses the risk to environment with use of refrigerants. On the other hand, membrane dehumidification systems can be energy efficient, but they are costly due to specialized membrane requirements and system design which is less studied to be able to incorporate into an HVAC unit. The solid and liquid desiccants have a moderate cost of installation, are more energy efficient than refrigeration systems and most importantly have been widely studied. They also have a lot of scope for improvement with new innovative desiccants. We see that there have been plethora of studies of liquid desiccants and solid desiccants using many desiccants. But presently there exist only two studies that we know of that are using special kinds of desiccants that are called thermoresponsive desiccants for air dehumidification. The first study by Kocher et al[29] compares traditional solid desiccant with thermoresponsive solid desiccant by modelling a thermodynamic dehumidification cycle. The second study by Zeng et al[30] compares the dehumidification potential of thermoresponsive interpenetrating polymer networks (IPNs) as desiccant against traditional desiccant silica gel. In both these cases thermoresponsive desiccant was much superior in terms of COP or moisture removal efficiency. These two

studies were also done for solid thermoresponsive desiccant, but none could be found for liquid thermoresponsive desiccants. Hence, in this work we have explored the potential of both liquid and solid thermoresponsive desiccants air dehumidification in air conditioning. The following subsections will introduce liquid and solid thermoresponsive desiccants.

1.2.4. LCST Ionic Liquid as Desiccants

Ionic liquids (ILs) are organic salts designed to melt below 100 ℃, characteristic properties like negligible volatility and non-flammability over a wide temperature range [31,32]. The physicochemical properties of ionic liquids can be tailored by chemical modification of the cation and/or anion, because of the sheer number of the ionic liquids that are possible leading to a vast number ($> 10^{14}$) of distinct cation-anion combinations[33]. A subclass of ionic liquids undergoes a thermoresponsive liquid-liquid phase transition of either an upper critical solution temperature (UCST) or lower critical solution temperature (LCST). These thermoresponsive IL-based mixtures have opened new potential applications like protein extraction, metal ion extraction, and forward osmosis draw solutes for water purification[34].

In liquid-liquid mixtures with an LCST transition, a single and miscible phase appears at lower temperatures. However, upon heating above a critical temperature T_c, the single-phase liquid-liquid mixture separates into two immiscible phases. From a thermodynamic

view, this behavior is understood in the framework of Equation (1-1) where ΔG_{mix} is the free energy of mixing, ΔH_{mix} is the enthalpy of mixing, and ΔS_{mix} is the entropy of mixing.

$$\Delta G_{mix} = \Delta H_{mix} - T\Delta S_{mix} \quad (1\text{-}1)$$

At low temperatures, strong intermolecular interactions, like hydrogen bonding, lead to a negative enthalpy of mixing therefore the two components are miscible at the low temperature. These intermolecular interactions come at an entropic cost. When the mixture is heated above the LCST temperature, the entropic term dominates as intermolecular interactions are broken, and the system entropy increases by phase separation due to increased degrees of freedom[35].

Kang et al.[34] showed that in IL-H_2O LCST mixtures of [P4444][DMBS]+H_2O 50 wt.%, the two phases above the LCST temperature form aggregates as can be seen in Figure 1-12(a). On the contrary the other ionic liquid mixture, [P4444][BnzSO3]+H2O 50 wt.% shown in Figure 1-12(b) does not show any aggregation when the temperature is increased. The particle size for the miscible phase (1-phase) was much smaller than the separated phases. The radial distribution functions obtained from molecular dynamics simulations support the observation of aggregation phenomena in the IL-H_2O mixtures.

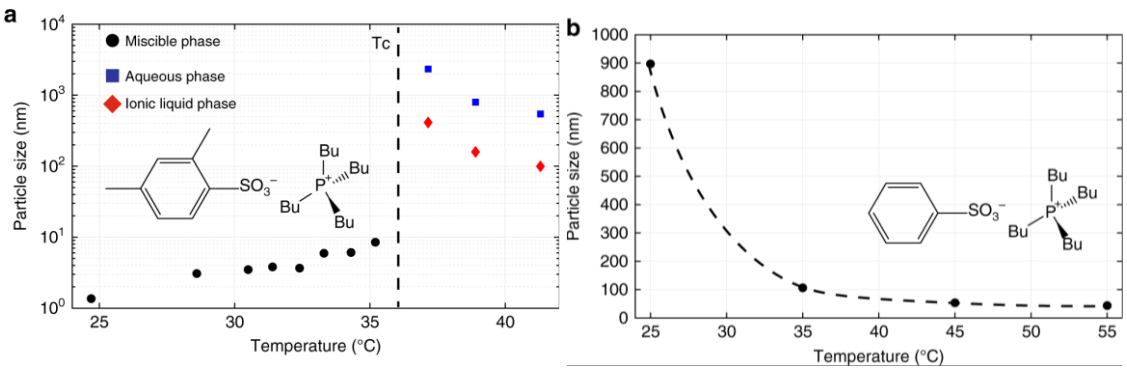

Figure 1-12: Dynamic light scattering cumulant analysis results for particle size versus temperature. (a) Particle size versus temperature of [P4444][DMBS]| H2O 50 wt.% over the fully miscible region and phase separated regions of the phase diagram. Phase separation temperature, T_c ca. 36 °C. (b) Particle size distribution of a [P4444][BnzSO3]|H2O 50 wt.% mixture versus temperature (Reprinted with Permission from Ref [34], open access under Creative Commons CC).

The existing liquid absorbents, such as Lithium Bromide and Lithium Chloride are corrosive due to halide ions present in them, particularly in an open system with oxygen present, with pronounced corrosion rates in the desorber that operates at relatively high temperatures[36]. To overcome these issues, Chugh et al.[37] have developed a semi open absorption system made up of membrane-based plate-and-frame heat exchangers that uses an ionic liquid (IL) as the liquid desiccant. Although there is a lot of literature about the liquid desiccants as the water absorbers, there aren't many ionic liquids that are used as the water absorbers especially ionic liquids that possess a thermoresponsive nature towards water. Hence, we study the potential of LCST ionic liquids as dehumidifiers.

1.2.5. Thermoresponsive Polymers

Hydrogels are soft materials consisting of physically or chemically cross-linked polymer networks and aqueous solutions. These hydrogels have been widely used as foods, disposal diaper, contact lenses because some of the fascinating behaviors such as water absorption, swelling, permeability, viscoelasticity, transparency, and biocompatibility.

One of the thermoresponsive hydrogels is poly(N-isopropylacrylamide) (PNIPAAm) which shows the LCST nature towards water. Figure 1-13 shows the schematic that shows how the PNIPAAm hydrophilic below its LCST temperature of 32 ℃ and absorbs water and becomes hydrophobic when the temperature exceeds this value where it releases the absorbed water. The hydrogel swells when its absorbs water and increases in volume and shrinks when it releases water. Although PNIPAAm possesses a thermoresponsive nature, it is not a great water absorber compared to some other polymers. Matsumoto et al.[38] synthesized an interpenetrating polymer network (IPN) gel comprising of thermoresponsive poly(N-isopropylacrylamide) and hydrophilic sodium alginate networks in their dried states. The dried IPN gel absorbs considerable moisture from air at temperatures below its LCST and oozes the absorbed moisture as liquid water above its LCST. These phenomena provide energy exchange systems in which moisture from air can

be condensed to liquid water using the controllable hydrophilic/ hydrophobic properties of thermoresponsive gels with a small temperature change.

Figure 1-13: Conceptual illustration of this study Water-adsorption and oozing behavior of dried PNIPAAm/Alg IPN gel. (Reprinted with Permission from Ref[38], open access under Creative Commons CC)

After the water was absorbed by the PNIPAAm/Alg IPN gel, its water oozing behavior was examined at different temperatures. Figure 1-14 shows that absorbed water is released rapidly after the LCST temperature of 32 ℃.

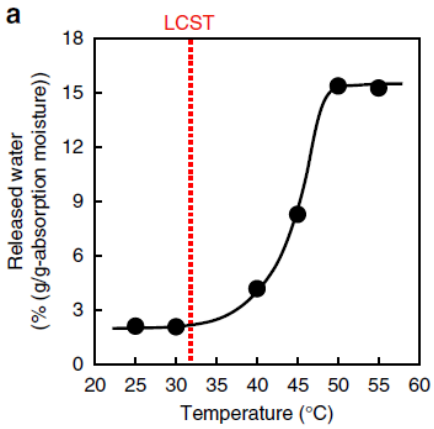

Figure 1-14: Thermoresponsive water oozing behaviors of PNIPAAm/Alg IPN gel at different temperatures (Reprinted with Permission from Ref [38], open access under Creative Commons CC).

Zhao et al.[39] have used super moisture-absorbent gel, polypyrrole chloride penetrating in poly *N*-isopropylacrylamide and used this LCST copolymer to water from the atmosphere for atmospheric water harvesting (AWH) in a broad range of relative humidity. The combined effect enabled by integration of hygroscopic and hydrophilicity-switchable polymers in a network architecture presents controllable interaction between the gel and water molecules, simultaneously realizing efficient vapor capturing, in situ water liquefaction, high-density water storage and fast water releasing under different weather conditions. Being an effective method to regulate the migration of water molecules, such design represents a novel strategy to improve the AWH.

1.3. Dissertation Scope and Outline

This dissertation focuses on studying thermoresponsive materials and exploring their potential as dehumidifiers in air conditioning. Both liquid and solid desiccants have been studied, with an emphasis on the regeneration of the desiccant by releasing water in liquid form, as opposed to the traditional vapor method used for desiccant regeneration.

Chapter 2 discusses the use of thermoresponsive ionic liquids as dehumidifiers. Since thermoresponsive ionic liquids have never been used as dehumidifiers, a thermodynamic

analysis of ionic liquids as dehumidifiers using Flory-Huggin's theory of mixing is presented. A thermoresponsive ionic liquid is compared with a non-thermoresponsive liquid desiccant using the dehumidification coefficient of performance that the two types of desiccants can produce. This chapter reveals that a thermoresponsive liquid desiccant produces a COP that is 4-times higher than a non-thermoresponsive liquid desiccant under similar conditions. Optimal operating conditions for peak performance are also suggested by testing the crucial input parameters governing the properties of the ionic liquids.

In chapter 3, the absorption process on thin film polymers is modeled using the Vrentas-Vrentas model, which considers the elastic Gibbs free energy of the polymer in addition to the mixing Gibbs free energy, offering a more accurate description compared to Flory-Huggin's theory. This chapter presents the absorption capacity of different hypothetical thermoresponsive polymers (TRPs) based on the poly(NIPAAm). The chapter lays the foundation for the next chapter by suggesting optimal parameters, such as the type of TRP and polymeric film thickness, for use in the subsequent finite element analysis of a thermoresponsive polymer.

Chapter 4 carries out a finite element design and analysis of a thermoresponsive dehumidifier in COMSOL. In this section, COMSOL is utilized to simulate the absorption of moisture from air and regenerate the polymer in the form of liquid water. The chapter introduces a novel regeneration method for a dehumidifier that hasn't been explored before.

The performance of the dehumidifier is assessed using moisture removal efficiency and compared to prior work with traditional regeneration that removes water by evaporating it using hot dry air.

In the final chapter, a preliminary synthesis of the copolymers is conducted to elevate the LCST temperature and absorption capacity of the resulting copolymer. The first monomer used is the well-known LCST monomer N-isopropylacrylamide (NIPAAm), and the second monomer is hygroscopic. The dissertation concludes with a summary and suggestions for future research.

2. THERMORESPONSIVE IONIC LIQUID DESICCANTS AS AIR DEHUMIDIFIER

2.1. Introduction

Dehumidification systems remove water vapor from air for the purposes of air conditioning, atmospheric water harvesting, and cold chain manufacturing/storage/distribution of perishable products (*e.g.*, food). Dehumidification systems largely fall under three different categories: vapor compression cycles,[40,41] solid desiccant systems,[9,42–44], and liquid desiccant systems.[15,21,45–50]. Vapor compression is a work-driven cycle that dehumidifies air by cooling it to the dew point. This condenses out the water vapor and is a work-intensive process. Rather than being work-driven cycles, desiccant systems are instead heat-driven cycles. Desiccants spontaneously absorb water vapor until they reach their saturation point. At this point, the absorbed water must be removed via a regeneration process so that the desiccant can be re-used for continued dehumidification. The regeneration process generally involves heating the desiccant up to a high temperature (*e.g.*, > 100 °C), which releases the water as vapor and consumes a large amount of energy.

In recent years, new desiccants with thermoresponsive behaviors have emerged that yield regeneration characteristics that are fundamentally advantageous.[29,30,39] These

thermoresponsive desiccants absorb water in a similar manner to traditional desiccants, but the regeneration process occurs differently. Traditional desiccants regenerate by using heat to drive a phase transition of the water into the gaseous state. Thermoresponsive desiccants regenerate by using heat to drive a phase transition within the desiccant itself. This desiccant phase transition leads to energy savings by changing the affinity between the desiccant and water. In some cases, this phase transition can drive a de-mixing process and cause water to be released in the liquid state.[29,38,39] Even if the absorbed water is released as a vapor, thermoresponsive desiccants can still lead to energy benefits due to a change in the absorption isotherms that accompany the phase transition in the desiccant.[30] Thermoresponsive desiccants have been reported in both solid- and liquid-form.[29,30,34,38,39,51–55] Solid thermoresponsive desiccants are generally based on polymer chemistries and some recent modeling reports using these within dehumidification systems show promising results.[29,30] The prospects for using solid thermoresponsive desiccants has also been noted in some recent perspective and review articles.[56–58] In contrast, reports on dehumidification system modeling using liquid thermoresponsive desiccants are comparatively scarce, with just one conference paper being very recently reported[59].

Most liquid-phase thermoresponsive desiccants are based upon ionic liquid (IL) chemistries (although deep eutectic solvents have also been recently reported[60] to exhibit this behavior). Here I focus our discussion on the more common IL case for the purposes

of clarity. ILs are salts with low melting temperatures and many ILs are in the liquid state at or below room temperature. These liquids are composed entirely of ions and do not contain any neutral molecules (in their pure state). Given their ionic characteristics, ILs exhibit hydroscopic properties like that of solid salts and aqueous salt solutions. Consequently, a pure IL that is exposed to ambient air will absorb humidity and become a water-IL solution.

Liquid thermoresponsive desiccants are ILs that exhibit a miscibility gap in the water-IL liquid phase diagram. Consequently, these desiccants undergo a temperature-induced phase transition from a homogeneous single-phase liquid to a heterogenous two-phase liquid [34,51,52]. The phase-transition temperature is referred to as either a lower critical solution temperature (LCST) or upper critical solution temperature (UCST). LCST solutions are single-phase at low temperature and two-phase at high temperature. UCST solutions exhibit the opposite behavior and are two-phase at low temperature and single-phase at high temperature. Another attractive characteristic of ionic liquids is the vast number of possibilities with respect to chemical composition, which facilitate the possibilities for finding/designing ILs in number of given applications.[32]

In this paper, the potential for LCST-type aqueous ionic liquid solutions for dehumidification is studied, and a thermodynamic cycle that accomplishes this objective is described. The phase diagram for the water-IL mixture plays a key role in system

performance. To highlight this, the Flory-Huggins theory of mixtures is applied to define the "U-shaped" immiscibility curve that separates the single-phase and two-phase regions of the phase diagram. The system performance is then reported as a function of the location and shape of the immiscibility curve as well as other operational considerations (*i.e.*, excess regeneration temperature difference beyond the LCST temperature). Finally, the performance of this thermoresponsive desiccant cycle is compared to a more traditional and non-thermoresponsive desiccant (nTRD) cycle.

2.1.1. Background on Thermoresponsive Liquid Mixtures

The phase behavior of thermoresponsive liquid mixtures is driven by the Gibbs free energy of mixing per mole, Δg_{mix}. Let us consider two component phases, *A* and *B*, which for the purposes of this discussion represent water and ionic liquid, respectively. Negative, zero, and positive values of Δg_{mix} correspond to spontaneous mixing, equilibrium, and non-spontaneous mixing, respectively. The Gibbs free energy is expressed in terms of the mixing enthalpy per mole (Δh_{mix}), mixing entropy per mole (Δs_{mix}), and absolute temperature (*T*),

$$\Delta \mathrm{g_{mix}} = \Delta h_{\mathrm{mix}} - \mathrm{T}\Delta s_{\mathrm{mix}} \qquad (2\text{-}1)$$

The Flory-Huggins theory of mixtures is frequently used to model the Gibbs free energy of polymer solutions and dictates miscibility at a particular concentration and

temperature.[61,62] For the case of large macromolecule solutes (polymers) and small molecule solvents, the mixing entropy is a function of both volume fractions and mole fractions. In comparison to the polymer case, the IL case can be considered to approximate the limit where the solute and solvent are of equivalent size and shape. In this case, the mixing entropy takes the form of an ideal solution as shown in Equation (2-2).

$$\Delta s_{\mathrm{mix}} = -\mathrm{R}(\mathrm{x_A} \ln \mathrm{x_A} + \mathrm{x_B} \ln \mathrm{x_B}) \tag{2-2}$$

where x_A and x_B denote the respective mole fractions of *A* and *B*, and *R* is the universal gas constant. The mixing enthalpy in Flory-Huggins theory is captured using the Flory-Huggins interaction parameter, χ_{AB},

$$\Delta \mathrm{h_{mix}} = \mathrm{RT}\left(\chi_{\mathrm{AB}}\, \mathrm{x_A x_B}\right) \tag{2-3}$$

Substituting in Equations (2-2) and (2-3) into Equation (2-1) yields, the Gibbs free energy of mixing:

$$\Delta \mathrm{g_{mix}} = \mathrm{RT}\left(\chi_{\mathrm{AB}}\ \mathrm{x_A x_B} + \mathrm{x_A} \ln \mathrm{x_A} + \mathrm{x_B} \ln \mathrm{x_B}\right) \tag{2-4}$$

Since $x_A + x_B = 1$, the above expression can be simplified substituting, $x_B = x$ and $x_A = 1 - x_B = 1 - x$. This yields the following expression for Δg_{mix}:

$$\Delta \mathrm{g_{mix}} = \mathrm{RT}\left(\chi_{\mathrm{AB}}\, (1-x)x + (1-x) \ln(1-x) + x \ln(x)\right) \tag{2-5}$$

As seen in Equation (2-5), the Gibbs free energy of mixing depends on the mixture composition, temperature, and the interaction parameter. For a given temperature, the graph of Δg_{mix} versus x can yield a single minima or multiple minima (Figure 2-1).

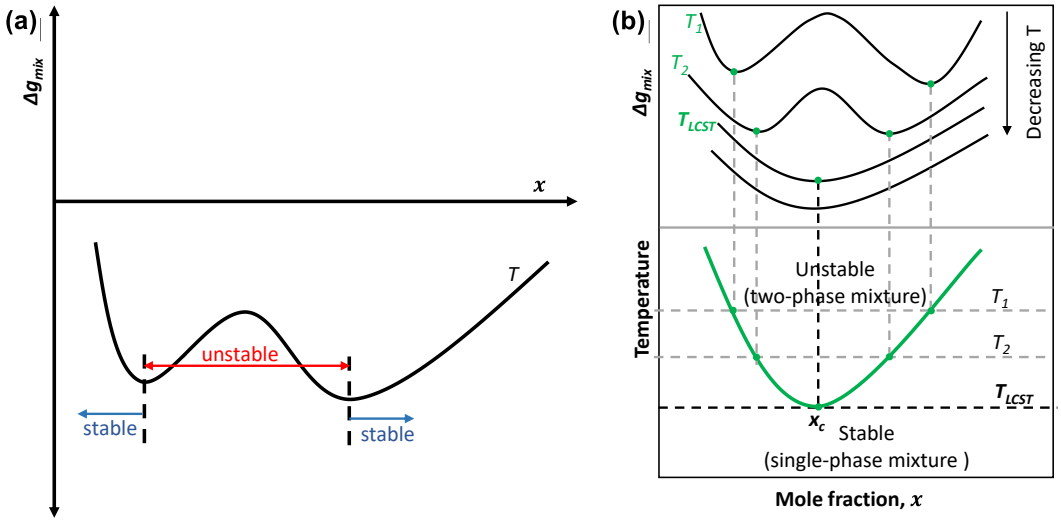

Figure 2-1: (a) Gibbs free energy of mixing of a typical IL-water mixture vs mole fraction x at a given temperature, T, (b) figure shows how locus of local minima's for Δg_{mix} vs x forms the phase diagram (T-x) for the IL-water mixture

Phase separation into two immiscible liquids occurs when there are multiple minima in the Δg_{mix} versus x curve. In this situation there is a region of instability between the two minima, and a mixture in this compositional region will not form a homogeneous single-phase liquid. Instead, this mixture will decompose into two immiscible liquids that have compositions corresponding to that of the two minima (Figure 2-1a). When the Δg_{mix} versus x curve is plotted for multiple temperatures, the locus of the minima form the boundary between the single-phase and two-phase regions of the phase diagram (green curve in Figure 2-1b). The curve that forms the boundary between the single-phase and two-phase regions is called the immiscibility curve.

At a particular critical temperature, T_c, and critical concentration, x_c, the two minima in Δg_{mix} converge. This represents the temperature at which the water-desiccant mixture is a single-phase solution for all mole fractions. LCST mixtures are such that the number of minima in Δg_{mix} transitions from multiple minima to a single minimum as the temperature is decreased whereas UCST mixtures do the reverse. Since this paper focuses exclusively on LCST mixtures, all critical temperatures are equivalent to LCST temperatures, $T_c = T_{LCST}$.

The phase behavior of the two liquids critically depends on the Flory-Huggins interaction parameter as this is the only materials-dependent property within Equation (2-5). The Flory-Huggins interaction parameter is unitless and temperature-dependent. It contains an entropic contribution, χ_S, and an enthalpic contribution, χ_H. [61–63]

$$\chi_{AB} = \chi_S + \frac{\chi_H}{T} \tag{2-6}$$

For the purposes of this paper, it is convenient to re-write this equation in terms of the LCST temperature. In the limit where the ionic liquid molecules and the water molecules can be approximated as the same size, Equation (2-6) can be re-written as the following equation (see Appendix A for more detail):

$$\chi_{AB} = 2 + \chi_H \left(\frac{1}{T} - \frac{1}{T_{LCST}}\right) \tag{2-7}$$

Equation (2-7) defines the interaction parameter in terms of χ_H and T_{LCST}. This is a

convenient relationship because T_{LCST} is a crucial and intuitive parameter that will play a key role in cycle performance.

The immiscibility curve in the water-IL phase diagram can also be written in terms of χ_H and T_{LCST} as follows (see appendix for more detail),

$$T = \frac{1}{\frac{1}{T_{LCST}} + \frac{\left(\frac{1}{1-2x}\right) ln\left(\frac{1-x}{x}\right) - 2}{\chi_H}} \tag{2-8}$$

The immiscibility curve in the phase diagram (*T*-*x* relation) is a "U-shaped" curve that separates the single-phase liquid region from the two-phase liquid region (bottom of Figure 2-1b). When a mixture is in the immiscible region (*i.e.*, region inside the "U") at a particular temperature, it will spontaneously phase separate into a water-rich liquid and an IL-rich liquid with compositions corresponding to points that directly lie on the immiscibility curve at that same temperature.

Figure 2-2 illustrates the independent effects of χ_H and T_{LCST} on the immiscibility curve in the phase diagram. The effect of χ_H is to control the curvature of the immiscibility curve (Figure 2-2a). As the magnitude of χ_H increases (χ_H become increasingly negative) the curvature of the immiscibility curve decreases. T_{LCST} is the minimum temperature in the immiscibility curve. Changing T_{LCST} does not alter the curvature of the immiscibility curve but does shift the curve (and its corresponding minimum) upward or downward (Figure 2-2b). In this work, the minimum in the immiscibility curve always occurs at a molar

concentration of x = 0.5 because the limit is considered where the IL molecules and the water molecules can be approximated as the same size. While this approximation is not strictly correct, it is a reasonable one relative to the case of polymer-solvent solutions in which Flory-Huggins theory is typically applied.

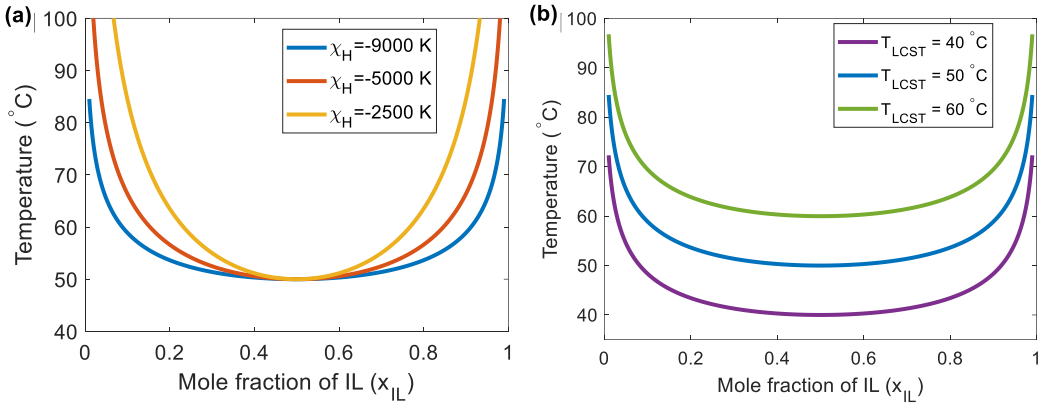

Figure 2-2 : Phase diagram (T-x) at (a) T_{LCST} = 50 °C and different enthalpic interaction parameters, χ_H and at (b) χ_H = -9000 K and different LCST temperatures

It is important to point out that despite its great advantages, the Flory-Huggins theory is not without its drawbacks. One significant limitation lies in the assumptions such as the constant volume upon mixing and the simplification that water and ionic liquid molecules are of comparable size. These assumptions may not hold true for more complex, real-world systems. Furthermore, the interaction parameter, χ, can be influenced by factors such as temperature, pressure, and composition, leading to inaccuracies in predictions but we have modeled it as only a function of temperature. Flory-Huggins theory works best for mixing non-polar polymer-solvents like alkanes where the interaction is governed by van der

Waals forces. It may be also used for the simple olefins like polyethylene where the majority of interaction is attributed to van der Waals forces and is only weakly polar. But it falls short when dealing the polar materials especially ones with hydrogen bonding where a simple interaction parameter (χ) cannot fully capture the complexity of the interaction.[64,65] The assumption that both mixture molecules (ionic liquid and water in our case) are of same size and they each occupy a single lattice point in the lattice oversimplifies the interaction between the two kinds of molecules.[61,62] The model's predictive power diminishes as the mixing components become more and more polar.

However, despite these disadvantages, the Flory-Huggins theory remains the most practical tool available for providing insights into interactions between different components during mixing and thus used here. It is widely used as a baseline for developing more complex models that can capture the nuances of specific systems. In this study, it is used as the baseline generic ionic liquid-water interactions without making concrete claims about any particular ionic liquid.

2.2. System Description and Modeling

Figure 2-3a shows the dehumidification system in a single-stage regeneration configuration and Figure 2-3b shows the corresponding thermodynamic cycle. The two main stages are the absorption stage (process $1 \rightarrow 2$) and the regeneration stage (process 3

→ 4 → 5/8). The absorption stage uses the IL-water desiccant solution to absorb water vapor and dehumidify the air. This process occurs in a similar manner to traditional non-thermoresponsive liquid desiccant dehumidification systems. The regeneration stage is a two-step progression that involves a heating process (3 → 4) and a separation process (4 → 5/8).

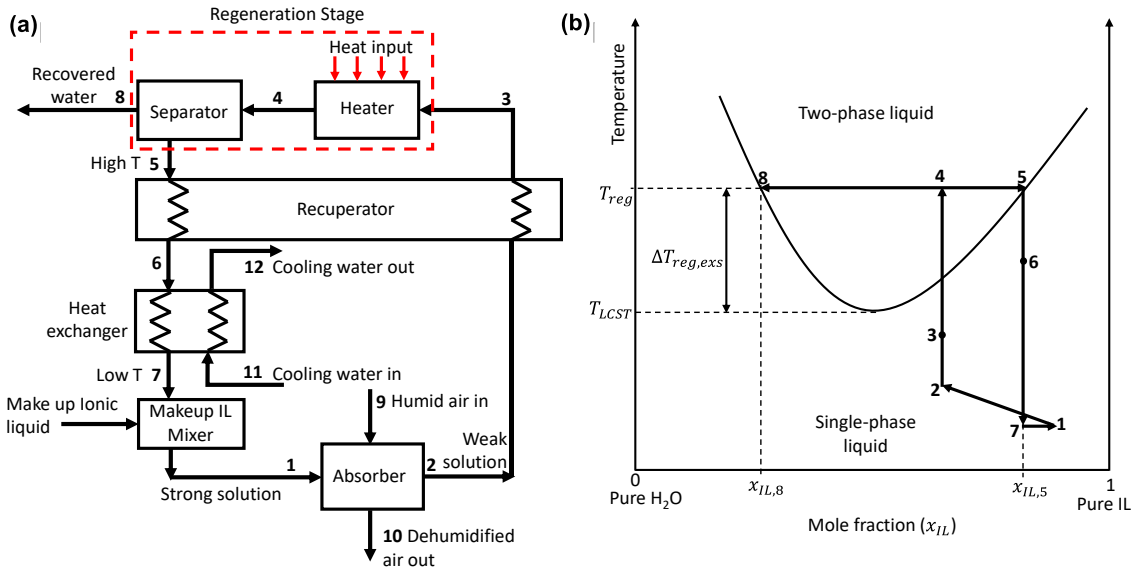

Figure 2-3: (a) Schematic of a single stage dehumidification system, (b) *T-x* phase diagram for ionic liquid dehumidification cycle

The overall cycle begins with the absorber, which has two streams entering it, a cold/strong solution of IL desiccant and humid air (points 1 and 9, respectively). Dehumidified air, which is the desired objective of this system, leaves the absorber at point 10. The consequence of dehumidifying the air has two effects on the cold/strong solution. First it dilutes the solution into a weak solution due to the absorption of the water vapor.

Second, the absorption of the water vapor is a condensation process, and this also warms the solution. Consequently, a warm and weak solution of IL desiccant leaves the absorber (point 2).

The weak IL solution is then pre-heated in a recuperator prior to arriving at the heater within the regeneration stage. This recuperator improves the energy efficiency of the system by reducing the necessary heat input into the system. It does this by exchanging thermal energy between the hot IL desiccant stream leaving the regeneration stage ($5 \rightarrow 6$) and the warm/weak IL desiccant stream traveling to the heater within the regeneration stage ($2 \rightarrow 3$).

As mentioned earlier, the regeneration process is a two-step progression that involves a heating process ($3 \rightarrow 4$) and a separation process ($4 \rightarrow 5/8$). While the regeneration process is frequently only shown as a heating process in a traditional non-thermoresponsive liquid desiccant cycle, it is noted that this heating and separating progression happens in both the traditional and thermoresponsive cases. In the traditional liquid desiccant system, the heating process increases the temperature of the water-desiccant solution to a temperature at which water vaporizes. The separation process then happens quickly and spontaneously due to the density difference between the gaseous water and the liquid solution (and so it generally not explicitly illustrated as a separator component). In addition, since the vapor pressure of liquid desiccants is often negligible at the regeneration

temperature, the water vapor leaving the solution is relatively pure and all of the desiccant remains in the liquid solution.

The regeneration process in the thermoresponsive liquid desiccant has key differences from the traditional non-thermoresponsive liquid desiccant system. Instead of the heater driving a liquid-to-vapor phase transition in the water, the heater in the thermoresponsive liquid desiccant drives a liquid-to-liquid phase transition. In this case, a single-phase water-IL solution transforms into two immiscible liquid phases corresponding to a water-rich phase and an IL-rich phase (points 8 and 5, respectively, in Figure 2-3b). Consequently, the water leaving the desiccant solution is not pure water and some IL is removed alongside the water from the desiccant solution. Another difference is that the separation process occurs very quickly and spontaneously in the traditional non-thermoresponsive liquid desiccant case due to the large density difference between the gaseous and liquid phases. In comparison, the density difference between the two liquid phases in this cycle is comparatively small and separation will occur much slower (although still spontaneously). In practice, this separation process could be sped up by inputting work (for example, using a centrifugal extractor). However, since this process is still spontaneous and because this study focuses on thermodynamics (as opposed to transport kinetics), and no work input into the separator is considered. Leaving the separator are two streams, a water-rich liquid (point 8) that contains the absorbed water from the system and an IL-rich liquid (point 5)

that will be re-used to dehumidify.

Prior to being re-used to absorb more humidity, the IL-rich liquid must be subject to additional processes to complete the thermodynamic cycle. First, the hot IL-rich liquid must be cooled back down to the absorber temperature. This is done through a two-step progression through a recuperator ($5 \rightarrow 6$) and then through an additional heat exchanger ($6 \rightarrow 7$). As mentioned earlier, the recuperator uses thermal energy from the hot IL-rich liquid to pre-heat the warm/weak IL solution that is traveling to the heater. However, the recuperator by itself is not sufficient to fully bring back the temperature back down to the absorber temperature and so an additional heat exchanger is used to provide further cooling via cooling water. Lastly, makeup IL is added back into the IL-rich liquid within a mixer ($7 \rightarrow 1$). This makeup IL is needed because the water-rich liquid stream that exited the system at the separator was not pure water and some IL was removed from the system alongside that water. For the purposes of modeling this system, T_7 is set to be the absorption temperature ($T_1 \approx 32℃$). This implicitly assumes that the cooling water flow rate and/or the cooling water inlet temperature can achieve the necessary amount of heat removal. Presumably, the cooling water loop rejects its heat to the outdoor temperature and so that temperature represents a lower limit to the cooling water temperature (T_{11}). In our simulation, the inlet air temperature to the absorber is fixed ($T_9 = 30℃$) and so our choice of setting $T_7 \approx 32℃$ is consistent with this. The makeup ionic liquid is supplied at

temperature T_1.

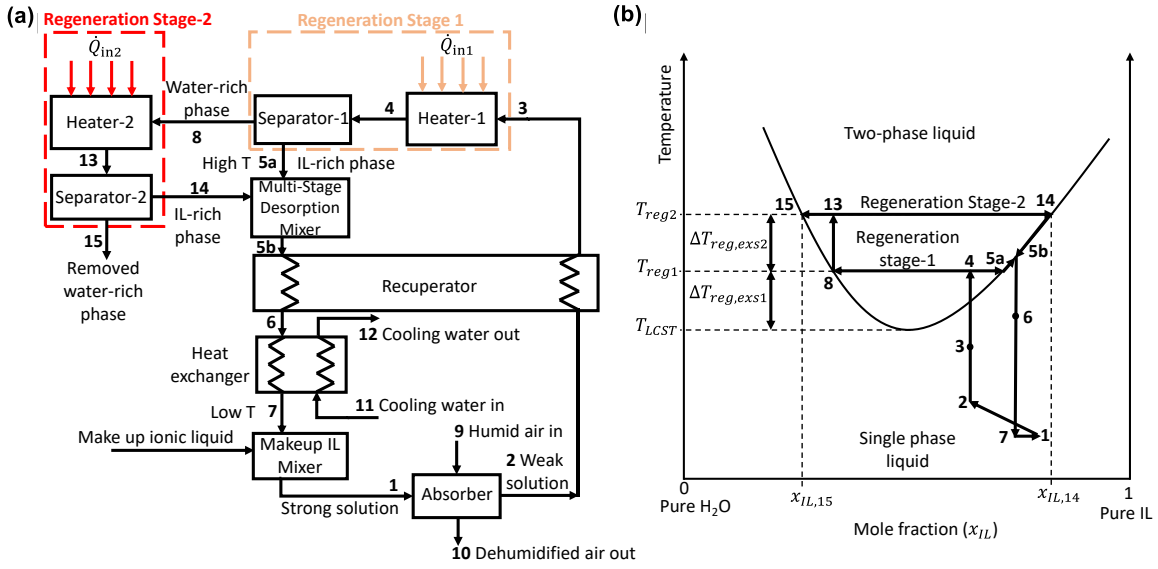

Figure 2-4: (a) Schematic of the dehumidification system two stage regeneration, (b) *T-x* phase diagram for ionic liquid dehumidification cycle

In addition to a single-stage dehumidification cycle, we also consider multi-stage dehumidification cycles that use thermoresponsive liquid desiccant. Figure 2-4 illustrates a two-stage example of the thermoresponsive liquid desiccant system. In this system, the single-phase water-rich liquid leaving the separator in the 1st stage (point 8) is sent to a 2nd regeneration stage. Here, the liquid is further heated to transform the single-phase water-rich liquid into immiscible water-rich and IL-rich phases (points 15 and 14, respectively, in Figure 2-4b). The main advantage of the multi-stage system is that it heats only a fraction of the IL desiccant solution to the hottest temperature, and thereby has the potential to reduce heat input and improve system efficiency.

Multi-stage cycles result in IL-rich streams exiting multiple separators. These are combined into a single IL-rich stream in the multi-stage regeneration mixer (process 5a/14 → 5b, see Figure 2-4b). Since these IL-rich streams have different temperatures and compositions, the resulting combined stream has a mass-weighted temperature and composition that lies between points 5a and 14. The solution mixture then exits the Mixer at point 5b. It's worth noting that the distance between points 5a and 5b in Figure 2-4b is exaggerated. In reality, point 5b will lie much closer to 5a, as evidenced in the phase diagrams presented in Section 4. In a manner similar to the single-stage system, this combined IL-rich stream is cooled in a recuperator (5b → 6), further cooled with an external cooling water source (6 → 7) and has makeup IL introduced (7 → 1) before it enters the absorber. While Figure 2.4 showcases the two-stage desiccant system, designs with three, four, or more stages can be constructed similarly. Subsequent sections provide an outline of key modeling aspects for the absorption and regeneration stages. For a thorough description of the entire system model, readers are directed to Appendix A.

2.2.1. Modelling Absorption Process

The absorption process is modeled using a moisture absorption effectiveness (ε_{ma}) and a temperature transfer effectiveness (ε_{ta}),

$$\varepsilon_{ma} = \frac{\omega_{a,9} - \omega_{a,10}}{\omega_{a,9} - \omega_{I,9}} \tag{2-9}$$

$$\varepsilon_{ta} = \frac{T_9 - T_{10}}{T_9 - T_1} \tag{2-10}$$

where ω is the humidity ratio and the numerical subscripts refer to the location within the system. Inside of the absorber, there is an interface between the IL solution and air and subscript *I* to refer to that interface. In both of these equations, the numerator describes the actual humidity (temperature) change whereas the denominator represents the maximum possible humidity (temperature) change. The humidity ratio of the air located at the IL-air interface at the absorber entrance (represented by $\omega_{I,9}$) is adjacent to IL that is in its strongest solution state (*i.e.*, least water content). Hence the equilibrium humidity of the air at this interface is the lowest humidity within the entire absorber. In addition, the air entering the absorber at point 9 is in its most humid state. Hence the denominator ($\omega_{a,9} - \omega_{I,9}$) represents the largest humidity difference in the absorber. If the air humidity at point 10, $\omega_{a,10}$, approaches that of $\omega_{I,9}$, it will have reached the thermodynamic limit for moisture absorption.

Humidity ratio is itself a function of the temperature of the air and partial pressure of water in the air (p_w). Consequently, the moisture absorption effectiveness (for a particular temperature) can be written as,

$$\varepsilon_{ma} = \frac{p_{w,9} - p_{w,10}}{p_{w,9} - p_{I,9}} \tag{2-11}$$

In Equation (2-11) the vapor pressure of water in the inlet air ($p_{w,9}$) is defined by the ambient air that needs to be dehumidified. The vapor pressure of water above the solution at the absorber inlet ($p_{I,9}$) depends on the concentration of the ionic liquid in the solution at the absorber inlet. In order to determine $p_{I,9}$, Raoult's law for ideal mixtures is used. With $p_{w,9}$ and $p_{I,9}$ defined, the vapor pressure of water at the absorber exit ($p_{w,10}$) can be determined for a given or assumed ε_{ma}. The moisture absorption rate, $\dot{m}_{abs}$, is determined by rearranging Equation (2-9) and multiplying through by the air mass flow rate, $\dot{m}_9$.

$$\dot{m}_{abs} = \dot{m}_9(\omega_{a,9} - \omega_{a,10}) = \dot{m}_9\varepsilon_{ma}(\omega_{a,9} - \omega_{I,9}) \quad (2\text{-}12)$$

Heat transfer represents a second thermodynamic driving force in the absorber and this process is described using the temperature transfer effectiveness (Equation (2-10)). Here the maximum possible heat transfer occurs if the exiting temperature of the air (T_{10}) reaches the inlet temperature of the ionic liquid solution (T_9). In Equation (2-13), T_9 is the temperature of the incoming humid air and T_1 is set to 32°C. With T_9 and T_1 defined, T_{10} can be determined for a given or assumed ε_{ta}.

$$T_{10} = T_9 - \varepsilon_{ta}(T_9 - T_1) \quad (2\text{-}13)$$

In addition to the humidity ratio and temperature of the air, it's essential to understand the enthalpies within the ionic liquid solution to analyze the overall system energy performance. Specifically, determining the exit temperature and exit enthalpy of the ionic liquid solution (T_2 and h_2, respectively) is crucial. This is achieved by performing an energy

balance on the absorber:

$$\dot{m}_9 h_9 + \dot{m}_1 h_1 + \Delta\dot{H}_{mix,1-2} = \dot{m}_{10} h_{10} + \dot{m}_2 h_2 \quad (2\text{-}14)$$

where $\Delta\dot{H}_{mix,1-2}$ represents the enthalpy change due to mixing of the incoming IL-solution and absorbed water from air, and can be written as

$$\Delta\dot{H}_{mix,1-2} = \dot{m}_2 h_{mix,2} - \dot{m}_1 h_{mix,1} \quad (2\text{-}15)$$

where $h_{mix,1}$ and $h_{mix,2}$ are obtained from the Flory-Huggins theory and can be written as follows

$$h_{\mathrm{mix},1} = \left[2 + \chi_H \left(\frac{1}{T_1} - \frac{1}{T_{LCST}}\right)\right] x_{IL,1}\, x_{H2O,1}\, RT_1 \quad (2\text{-}16)$$

$$h_{\mathrm{mix},2} = \left[2 + \chi_H \left(\frac{1}{T_2} - \frac{1}{T_{LCST}}\right)\right] x_{IL,2}\, x_{H2O,2}\, RT_2 \quad (2\text{-}17)$$

In Equation (2-16), both concentrations ($x_{IL,1}$ and $x_{H2O,1}$) as well as the temperature T_1 are known. R is the universal gas constant and χ_H and T_{LCST} are determined by the particular choice of IL. Then Equation (2-17) is used to solve for T_2 because concentrations $x_{IL,2}$ and $x_{H2O,2}$ can be determined for a given ε_{ma}. The specific enthalpy of the air at absorber inlet (h_9) and exit (h_{10}) is calculated using psychrometry (*i.e.*, MATLAB function *Psychrometricsnew*[66]). A representative specific heat of ILs is used during our calculations. The specific heat of most ionic liquids is in the 1.2 - 2 kJ/kg-K range,[67–69] and an average value of 1.6 kJ/kg-K used. For the purpose of converting mole fractions of ionic liquid to mass fractions of ionic liquid, a representative molecular weight of 240 g/mol for

the ionic liquid is used.

2.2.2. Regeneration Stage Modeling

The regeneration stage is a two-step progression that involves a heating process (3 → 4) and a separation process (4 → 5/8). The heater raises the temperature of the strong IL solution to a regeneration temperature, T_{reg}, that exceeds T_{LCST} by an excess regeneration temperature difference, $\Delta T_{reg,exs}$,

$$T_{reg} = T_{LCST} + \Delta T_{reg,exs} = T_4 \tag{2-18}$$

In practice, this excess regeneration temperature difference is necessary to achieve phase separation into two immiscible liquids because T_{LCST} represents the minimum temperature on the immiscibility curve, and corresponds to a critical molar concentration, x_C. Due to the shape of the immiscibility curve (Figure 1b), temperatures above the LCST do not necessarily drive a phase transition if the molar concentration deviates from x_C (as indicated earlier, x_C = 0.5 for the phase diagram model used in this work). As shown later in Section 4, we will see that most of the cycles operate with x_{IL} in the > 0.8 range, which is well above the critical concentration. For these reasons, an excess regeneration temperature difference, $\Delta T_{reg,exs}$, is necessary.

The respective compositions of the water-rich and IL-rich liquid phases are influenced by $\Delta T_{reg,exs}$) due to the curvature of the immiscibility curve. As the magnitude of $\Delta T_{reg,exs}$

increases, the IL-rich phase becomes richer in IL content, and the water-rich phase becomes more concentrated in water (refer to Figure 2-3b). In scenarios with multiple regeneration stages, the total excess regeneration temperature difference is divided into n-equal increments, where n represents the number of stages (see Figure 2-4b). It's important to highlight that in the definition of excess regeneration temperature, $\Delta T_{reg,exs}$ is not gauged in relation to the immiscibility curve. Instead, $\Delta T_{reg,exs}$ is compared to T_{LCST}, a constant across all x_{IL} values in the phase diagram. Thus, for $x_{IL} \neq 0.5$, it's possible to record a positive $\Delta T_{reg,exs}$ while still achieving no separation.

The regeneration heat required to drive the desorption, $\dot{Q}_{reg}$, is follows:

$$\dot{Q}_{reg} = \dot{m}_3 c_{p,s}\left(T_{LCST} + \Delta T_{reg,exs} - T_3\right) + \Delta \dot{H}_{demix} \quad (2\text{-}19)$$

The first term on the righthand side represents the sensible heat needed to raise the temperature of the strong IL solution. The second term represents the demixing enthalpy required to drive the phase transition from a single-phase liquid to two immiscible liquids. The demixing enthalpy is obtained from the Flory-Huggins theory of mixing.

$$\Delta \dot{H}_{demix} = \dot{m}_4 h_{4,mix} - (\dot{m}_5 h_{5,mix} + \dot{m}_8 h_{8,mix}) \quad (2\text{-}20)$$

As described in Section 2, the process of separating the water-rich liquid and the IL-rich liquid into separate streams will spontaneously occur due to their difference in density. In practice, this liquid-liquid separation could be too slow, and work input could be needed (for example, using a centrifugal extractor). However, since this process is spontaneous

and because this study focuses on thermodynamics (as opposed to transport kinetics no work input into the separator is considered.

2.2.3. Performance Metrics

The overall system performance is described using two metrics, dehumidification coefficient of performance, COP_{deh}, and ionic liquid makeup ratio, r_{makeup}. The dehumidification coefficient of performance is defined as the water removed from air by the IL-solution per regeneration heat input as shown in Equation (2-21). The numerator in Equation (2-21) denotes the energy needed to condense water from the air and the denominator is the heat input required to separate the absorbed water from the IL-solution.

$$COP_{deh} = \frac{\dot{m}_{abs} h_{fg}}{\dot{Q}_{reg}} \tag{2-21}$$

The dehumidification process can also introduce a heating or cooling effect on the air, and when this effect is included a thermal coefficient of performance, $COP_{thermal}$, is used. The formula for $COP_{thermal}$ is similar to COP_{deh}, but has an additional sensible heat term in the numerator (see Section S3 in Supplementary Material). For most scenarios investigated in this paper ($T_{air,in}$= 30 ℃ and T_1 = 32 ℃) this sensible heat term is small and negative, resulting in a $COP_{thermal}$ that is slightly less than COP_{deh}, but that otherwise tracks closely to the COP_{deh} trends. For completeness, a set of results for $COP_{thermal}$ is include in Appendix A.

The makeup ratio, r_{makeup}, is another important metric in our system.

$$r_{makeup} = \frac{\dot{m}_{abs}}{\dot{m}_{makeup}} \tag{2-22}$$

As described in Section 2, the water removed in the regeneration stage is not pure water. Instead, it is a water-rich liquid that has some IL within it (point 8 in Figure 2-3). Consequently, IL must be re-added to the cycle to replace the IL that is lost in the separation process. The makeup ratio is the mass rate of absorbed water divided by the mass rate of makeup ionic liquid. Higher values of r_{makeup} indicate better performance because this means that less makeup ionic liquid is needed by the system.

2.2.4. Model Input Parameters

For the purposes of studying system performance, inlet air conditions of 30 °C and 70% relative humidity (RH), which is representative of summer conditions in Miami, Florida is used. Another important input parameter is the mass flow rate ratio (*MRR*) between the air ($\dot{m}_9$) and the solution ($\dot{m}_1$) entering the absorber, $MRR = \dot{m}_9/\dot{m}_1$. Most previous studies have reported the *MRR* values between 1.3 and 3.3 [21,45,70,71]. For the purposes of this work, an intermediate value of *MRR* = 2 is chosen. Unless otherwise indicated, the values indicated in Table 1 are used as the default inputs into our model.

In all the models, the mass flow rate of the ionic liquid solution entering the absorber ($\dot{m}_1$) is initialized as 0.5 kg/s with an $x_{IL,1}$ of 0.9. The value of $\dot{m}_1$ remains fixed at 0.5 kg/s

throughout the simulation. This is achieved by considering $\dot{m}_7$ and adding an appropriate amount of makeup ionic liquid to reach this value: $\dot{m}_7 + \dot{m}_{makeup}$ = 0.5 kg/s. The simulation continues until cycle convergence is attained.

It's important to note that the maximum temperature in the cycle is capped at 95 ℃. This limit is chosen because the objective of the cycle is to leverage the phase transition of the desiccant to facilitate the regeneration process, rather than relying on the boiling phase transition of water. Generally, a value of 30 ℃ is used for the excess regeneration temperature, $\Delta T_{reg,exs}$. However, to remain below the boiling point of water and adhere to the 95 ℃ threshold, when T_{LCST} surpasses 65 ℃, the value of $\Delta T_{reg,exs}$ is adjusted to 95 ℃ - T_{LCST}.

Table 2-1: List of input parameters and their default values

Type	**Parameter**	**Default value**
Parameters of air (Point 9)	Inlet mass flow rate of air, $\dot{m}_{air}$	$1 \frac{\text{kg}}{\text{s}}$
	Inlet temperature of air, $T_{air,in}$	30 ℃
	Relative humidity, $RH_{air,in}$	70 %
Parameters of IL solution (Point 1)	Inlet mass flow rate of IL solution, $\dot{m}_1$	$0.5 \frac{\text{kg}}{\text{s}}$
	Inlet temperature of solution, T_1	32 ℃
	Lowest critical solution temperature of IL, T_{LCST}	50 ℃
	Specific heat of ionic liquid, $c_{p,IL}$	$1.6 \frac{\text{kJ}}{\text{kg}-\text{K}}$
	Molecular weight of ionic liquid, M_{IL}	$240 \frac{\text{g}}{\text{mol}}$
	Enthalpic interaction parameter, χ_{H}	-9000 K
Other parameters	Moisture absorption effectiveness ratio,	0.80

	ε_{ma}	
	Temperature transfer effectiveness ratio, ε_{ta}	0.80
	Recuperator effectiveness, ε_{rec}	0.70
	Excess regeneration temperature difference, $\Delta T_{reg,exs}$	30℃ if T_{LCST} < 65 ℃
		95℃ - T_{LCST} if T_{LCST} > 65 ℃

2.3. Results And Discussion

The discussion now centers on how the key ionic liquid system operational properties influence the overall system performance, specifically the dehumidification coefficient of performance, COP_{deh}, and the makeup ratio, r_{makeup}. The key ionic liquid properties are the lower critical solution temperature, T_{LCST}, and the enthalpic portion of the interaction parameter, χ_{H}. These two properties affect the location and shape of the immiscibility curve within the water-desiccant phase diagram. T_{LCST} affects the location of the immiscibility curve's minimum whereas χ_{H} affects the curvature of the immiscibility curve. The key system operational parameter that is investigated is the excess regeneration temperature, $\Delta T_{reg,exs}$.

2.3.1. Generalized Discussion on COP_{deh} and r_{makeup}

COP_{deh} and r_{makeup} depend upon the moisture absorption rate, regeneration heat, and mass flow rate of makeup ionic liquid ($\dot{m}_{abs}$, $\dot{Q}_{reg}$, and $\dot{m}_{makeup}$, respectively) as shown in Equations (2-21) and (2-22). Consequently, it is instructive to first discuss the main

parameters that drive these factors before talking about the specific cases of varying T_{LCST}, χ_{H}, and $\Delta T_{reg,exs}$.

2.3.1.1. Moisture Absorption Rate

The moisture absorption rate, $\dot{m}_{abs}$, represents the rate at which water is absorbed out of the humid air and this represents the key goal of the dehumidification system. Both COP_{deh} and r_{makeup} increase linearly as $\dot{m}_{abs}$ increases and so maximizing this parameter is key to improving system performance. When all other factors remain constant, it was found that the moisture absorption rate varies linearly with the ionic liquid molar concentration entering the absorber, $x_{IL,1}$ (Figure 2-5).

The relationship between $x_{IL,1}$ and $\dot{m}_{abs}$ shown in Figure 2-5 means that there is a predictable correlation between $x_{IL,1}$ and the system performance metrics. As $x_{IL,1}$ increases, so does $\dot{m}_{abs}$ and this has a positive effect on COP_{deh} and r_{makeup}. Provided this increase in $\dot{m}_{abs}$ is not overpowered by corresponding increases in $\dot{Q}_{reg}$ or $\dot{m}_{makeup}$ (which negatively affect COP_{deh} and r_{makeup}), an increasing $x_{IL,1}$ means an increasing COP_{deh} and an increasing r_{makeup}.

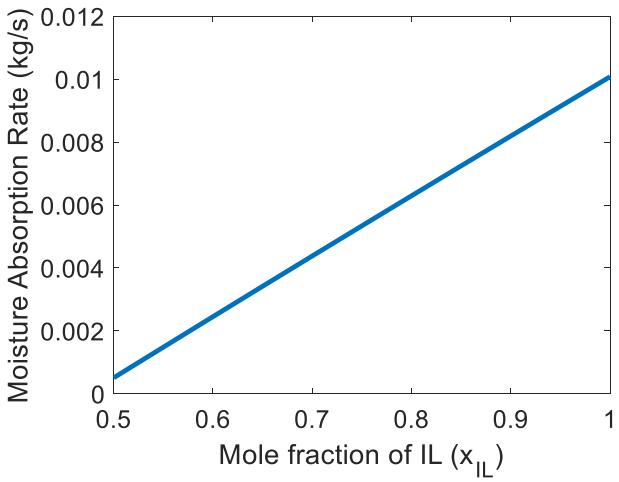

Figure 2-5: The effect of ionic liquid (IL) mole fraction of the solution entering the absorber ($x_{IL,1}$) on the moisture absorption rate for an absorber inlet solution temperature of 32 ℃

2.3.1.2. Regeneration Heat Rate

COP_{deh} is inversely related to $\dot{Q}_{reg}$ and so minimizing this heat rate leads to improved COP_{deh}. The regeneration heat is comprised of two energy components, a sensible heat that is needed to raise the temperature and a demixing enthalpy that is needed to separate the solution into water-rich and IL-rich phases (see Equation (2-19)).

The sensible heat and demixing enthalpy can be visualized by the vertical length of line 2-4 and the horizontal length of line 5-8 in Figure 2-6, respectively. Since the goal of this system is to separate out water, the demixing enthalpy is a price that must be paid to achieve this goal. That being said, the amount of input sensible heat needed to achieve a differential amount of demixing isn't necessarily fixed.

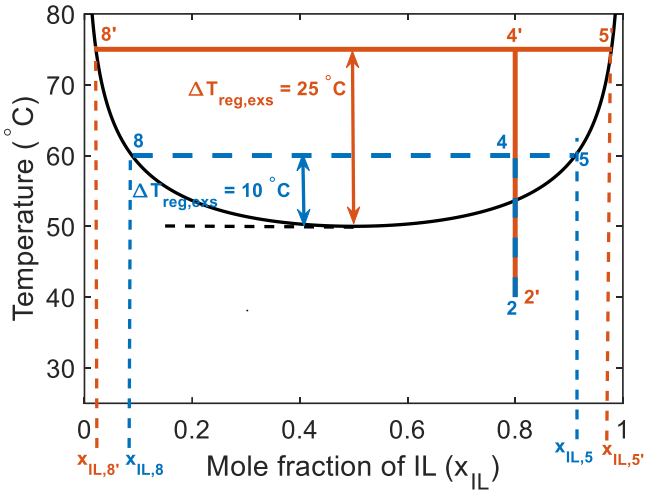

Figure 2-6: Effect of excess regeneration temperature on the concentrations of IL in water-rich phase and IL-rich phase

The input sensible heat needed to achieve a differential amount of demixing can be visualized through the local slope of the immiscibility curve. The vertical rise in the slope represents a differential sensible heat input whereas the horizontal run of the slope represents a differential amount of demixing (separation of water and IL). Flatter curves mean that less sensible heat is needed for a given amount of demixing. Hence the ratio of sensible heat to demixing enthalpy is best near the center of the phase diagram (x_{IL} = 0.5) and gets increasingly worse upon approach to the edges of the phase diagram (x_{IL} = 0.0 or 1.0). Increasing sensible heat near the edges of the phase diagram will continue to increase separation, but with diminishing returns due to the increasing steepness of the immiscibility curve. Hence increasing sensible heat input near the center of the phase diagram will generally lead to increases in COP_{deh}, but increasing sensible heat input near the edges of

the phase diagram will generally lead to decreases in COP_{deh}. The ideal immisicibility curve would be a perfectly horizontal line at the LCST temperature that spans across the full x_{IL} range and then turns 90 degrees to a vertical upward line at x_{IL} = 0.0 and 1.0. In this case, a differential sensible heat input above T_{LCST} would yield perfect phase separation between the water and IL and no excess regeneration temperature difference, $\Delta T_{reg,exs}$, would be necessary.

Another way to decrease $\dot{Q}_{reg}$ and hence improve COP_{deh} is to do regeneration in multiple stages (Figure 2-4). Increasing the number of regeneration stages means that less solution mass is heated to the highest regeneration temperature. This contrasts with a single stage process, where the entire solution mass is heated to the highest regeneration temperature. Consequently, an increase in the number of stages typically leads to a reduction in $\dot{Q}_{reg}$. It is seen that improvements in $\dot{Q}_{reg}$ with increasing regeneration stages cannot be directly visualized on the phase diagram (Figure 2-4b). This is because the phase diagram shows molar concentrations and because it does not directly show the mass flow rates going from one regeneration stage to the next (which are critically important to determining $\dot{Q}_{reg}$).

It is also important to note that the improvements in $\dot{Q}_{reg}$ with increasing regeneration stages does come with a tradeoff. This tradeoff is reduced separation because only a fraction of the IL solution is heated to the highest regeneration temperature (and hence only

a fraction of the IL solution is separated to the largest extent). This decreased separation leads to a more dilute ionic solution (*e.g.* x_{IL} at point 5b versus point 14 in Figure 2-4b), which can in turn lead to decreased moisture absorption and a negative effect on COP_{deh}.

2.3.1.3. Makeup Ionic Liquid Rate

The makeup ratio (r_{makeup}) defines the proportion between the moisture absorption rate and the makeup IL rate, given by $\dot{m}_{abs}/\dot{m}_{makeup}$. It can be enhanced either by elevating $\dot{m}_{abs}$ or diminishing $\dot{m}_{makeup}$. The dependence of $\dot{m}_{abs}$ on $x_{IL,1}$ was explored earlier in Section 2.3.1.2; thus, the emphasis here is on $\dot{m}_{makeup}$. The makeup IL rate can be partially discerned by observing point 8 in the thermodynamic cycle. Point 8 signifies the molar concentration ($x_{IL,8}$) of the water-rich phase departing the separator during regeneration. This phase mirrors the IL extracted from the system, which must be replenished to reset the thermodynamic cycle. Generally, with all else constant, $x_{IL,8}$ declines as $\Delta T_{reg,exs}$ grows or the absolute value of χ_{H} increases, leading to a decrease in $\dot{m}_{makeup}$.

However, adjusting any system aspect can cause multiple impacts, necessitating joint consideration of both $\dot{m}_{abs}$ and $\dot{m}_{makeup}$ to ascertain the actual r_{makeup} alteration. It's pivotal to understand that point 8 solely indicates the molar concentration of the exiting ionic liquid solution. To translate this into the actual departing ionic liquid, two unrepresented elements on the phase diagram are crucial: the mass flow rate of the ionic

liquid solution at point 8 and the ionic liquid's molecular weight.

During modeling, it was observed that augmenting the number of regeneration stages did not influence r_{makeup} (as discussed in Sections 2.3.2 – 2.3.5). Typically, adding stages led to a drop in $\dot{m}_{makeup}$. This wasn't due to changes in the molar concentration of the ionic liquid in the separated water-rich phase. It occurred because an increase in regeneration stages meant a reduced fraction of the mass flow rate reached the final separator. However, a decrease in $\dot{m}_{makeup}$ was offset by a corresponding drop in $\dot{m}_{abs}$, keeping r_{makeup} consistent regardless of the number of regeneration stages. This static ratio between $\dot{m}_{makeup}$ and $\dot{m}_{abs}$ stems from the symmetric nature of the immiscibility curve in this study. Typically, water-IL immiscibility curves exhibit some asymmetry, meaning r_{makeup} independence from the stage number might not always be the case.

Furthermore, alternate designs of this thermoresponsive dehumidification cycle might recapture the ionic liquid within the separated water-rich phase (point 8), eliminating makeup IL necessity. For example, the highly water-rich solution at point 8 could potentially undergo concentration via water's evaporative cooling, then re-enter the cycle [59]. This intricate cycle version would also offer both dehumidification and cooling advantages. For this paper's scope, the focus remains on dehumidification, primarily examining how the immiscibility curve's shape impacts system efficiency.

2.3.2. Effect of LCST on Performance Parameters

An increase in LCST temperature shifts the immiscibility curve towards higher temperatures (Figure 7c). For a fixed absorber inlet temperature, T_1, and excess regeneration temperature $\Delta T_{reg,exs}$, the primary outcome of elevating the LCST temperature is a modification in the maximum temperature achieved in the system (notice the changing T_4 in Figure 7c).

Figure 2-7a shows that COP_{deh} decreases as T_{LCST} increases. This effect occurs because as T_{LCST} increases, $\dot{Q}_{reg}$ increases and $\dot{m}_{abs}$ decreases, both of which lead to decreased COP_{deh}. The increase in $\dot{Q}_{reg}$ is visible in Figure 2-7c via increases in the vertical length of line 2-4, which represents the sensible heat input into the system. The vertical distance between point 2 and the immiscibility curve is especially important, because this represents a sensible heat input for which no accompanying demixing occurs, and this also increases as T_{LCST} increases. Figure 2-7c also shows that that an increasing T_{LCST} causes $x_{IL,1}$ to decrease. This decreasing $x_{IL,1}$ causes a decrease in $\dot{m}_{abs}$ and so consequently also hurts COP_{deh} (see Section 2.3.1). A discontinuity at T_{LCST} = 65 ℃ is visible in Figure 2-7a. This results from the maximum regeneration temperature constraint that is implemented to avoid boiling of the water ($T_{reg} \leq$ 95 ℃, see Section 2.3.4). For T_{LCST} < 65 ℃, $\Delta T_{reg,exs}$ is fixed to be 30 ℃. However, for T_{LCST} > 65 ℃, $\Delta T_{reg,exs} = 95℃ - T_{LCST}$.

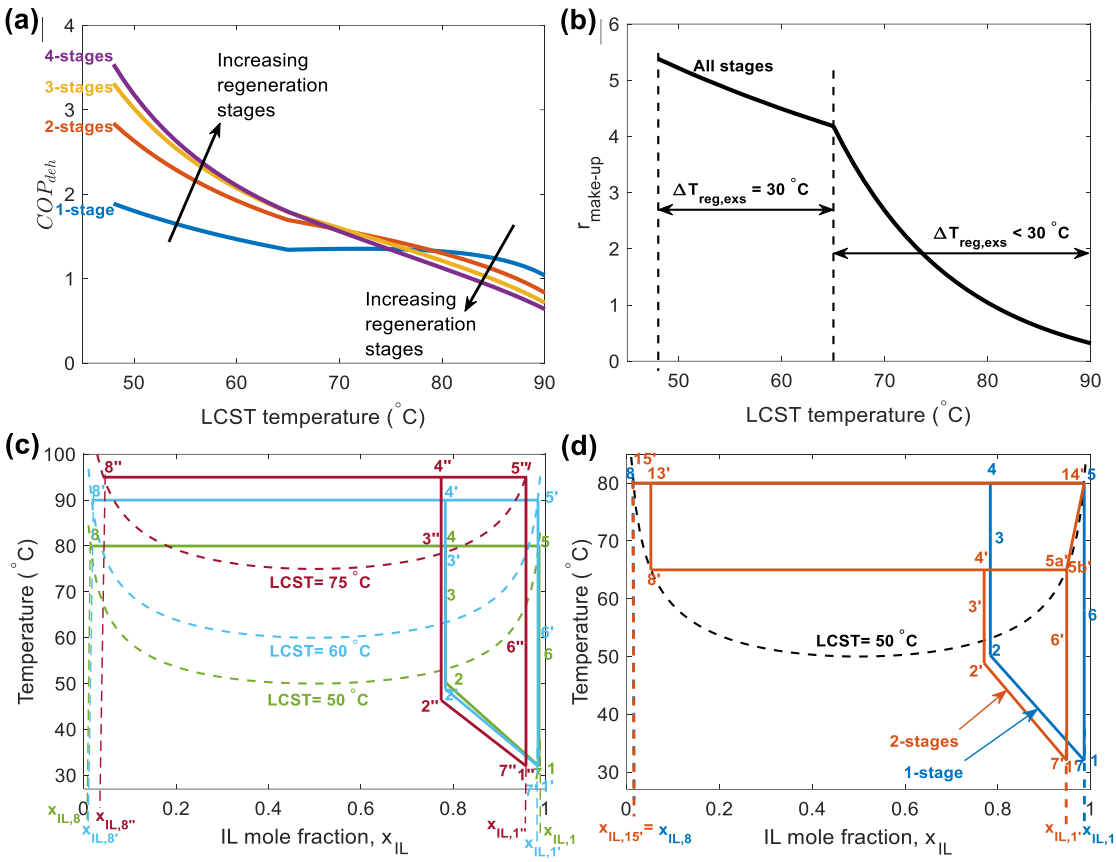

Figure 2-7: Effect of LCST temperature and number of regeneration stages on (a) Dehumidification Coefficient of Performance, and (b) IL makeup ratio, (c) phase diagrams for dehumidification cycle at LCST 50 °C, 60 °C and 75 °C, (d) phase diagram for the T_{LCST} = 50 °C and χ_H = -9000 K for 1-stage and 2-stages regeneration

By extrapolation of the COP trend with decreasing T_{LCST}, one might assume that picking ionic liquid mixtures with lower and lower T_{LCST} would lead to better and better COP. However, this would not be the case in practice due to the necessary heat rejection in the cycle (process 6 → 7). The cooling water loop should cool the ionic liquid solution to below the LCST temperature, and presumably the cooling water loop rejects its heat to the outdoor environment. Consequently, the outdoor temperature represents a lower limit for

the LCST. Given this limitation, outdoor temperature variations (geographic and time of year), and limitations on heat exchanger effectiveness, a T_{LCST} of 50 °C likely represents a practical and approximate lower limit.

Figure 2-7a shows that increasing the number of stages (n_{stages}) increases COP_{deh} at low T_{LCST} and decreases COP_{deh} at high T_{LCST}. This reversal in trend can be understood by examining $\dot{Q}_{reg}$ and $\dot{m}_{abs}$, both of which affect COP_{deh}. Increasing the number of regeneration stages helps COP_{deh} by reducing $\dot{Q}_{reg}$. However, increasing the number of stages also hurts COP_{deh} by decreasing $x_{IL,1}$, which in turn decreases $\dot{m}_{abs}$ (Figure 2-7d). At low T_{LCST} values, the reduction in $\dot{Q}_{reg}$ has the dominant effect on COP_{deh}. At high T_{LCST} values, the reduction in $\dot{m}_{abs}$ has the dominant effect on COP_{deh}.

Figure 2-7b demonstrates that the makeup ratio, r_{makeup}, decreases as the LCST temperature increases. This can be visualized by the IL concentration at point 8 in Figure 2-7c. Larger values of $x_{IL,8}$ hurt r_{makeup} because more IL is lost during the separation process and hence more makeup IL is needed. Mirroring and compounding the effects of increases in $x_{IL,8}$, are decreases in $x_{IL,1}$ which decrease $\dot{m}_{abs}$ and also hurt r_{makeup}. These effects become more drastic for $T_{LCST} > 65$°C because $\Delta T_{reg,exs}$ is decreased in this range and this draws points 5 and 8 toward the center of the immiscibility curve in a faster manner. It is observed that the number of stages does not affect r_{makeup} as discussed in Section 2.3.1.2.

2.3.3. Effect of the Enthalpic Interaction Parameter on Performance Parameters

The enthalpic interaction parameter, χ_{H}, affects the curvature of the immiscibility curve. Figure 2-8c shows that as the magnitude of χ_{H} increases (χ_{H} become increasingly negative) the curvature of the immiscibility curve decreases. The curvature has a drastic and non-linear effect on the resulting composition of the water-rich and IL-rich phases ($x_{\mathrm{IL},5}$ and $x_{\mathrm{IL},1}$, respectively). The inset of Figure 2-8c illustrates the non-linear relationship between $x_{\mathrm{IL},5}$ and χ_{H}. The curve's slope is pronounced and steep in the range of -5000 K < χ_{H} < 0 K, and is comparatively mild and shallow in the range of from -10000 K < χ_{H} < -5000 K.

Figure 2-8a shows that COP_{deh} generally increases as the magnitude of χ_{H} increases (*i.e.*, as χ_{H} becomes increasingly negative and moves toward the left of the x-axis). This effect occurs because $\dot{m}_{abs}$ increases and $\dot{Q}_{reg}$ decreases as the magnitude of χ_{H} increases, both of which improve COP_{deh}. A larger magnitude of χ_{H} causes an increase in $x_{\mathrm{IL},5}$ which tightly correlates to an increase in $x_{\mathrm{IL},1}$ (Figure 8c). This increases in $x_{\mathrm{IL},1}$ causes an increase in $\dot{m}_{abs}$ and consequently an increase in COP_{deh}. This effect is more drastic in the -5000 K < χ_{H} < 0 K range and relatively mild in the -10000 K < χ_{H} < -5000 K range because of the non-linear relationship between $x_{\mathrm{IL},5}$ and χ_{H} (inset of Figure 2-8c).

An additional effect of this increased $\dot{m}_{abs}$, is a reduced sensible heat input (line 2-4) which helps both $\dot{Q}_{reg}$ and COP_{deh}. Increasing $\dot{m}_{abs}$ directly improves COP_{deh} via the

numerator in Equation (2-21). However, increases in $\dot{m}_{abs}$ provide an additional improvement in COP_{deh} through an indirect effect on $\dot{Q}_{reg}$. The absorption of water vapor from the air has synergistic effects in this system. First, it decreases air humidity, which is the primary function of the system. However, the water absorption also has a heating effect on the IL solution due to the water vapor's enthalpy of condensation. As more water is absorbed, this heating effect increases, and point 2 in Figure 2-8c become increasingly hotter as the magnitude of χ_{H} increases. Increasing the temperature of point means that less sensible heat input is needed during regeneration, and this also improves COP_{deh}.

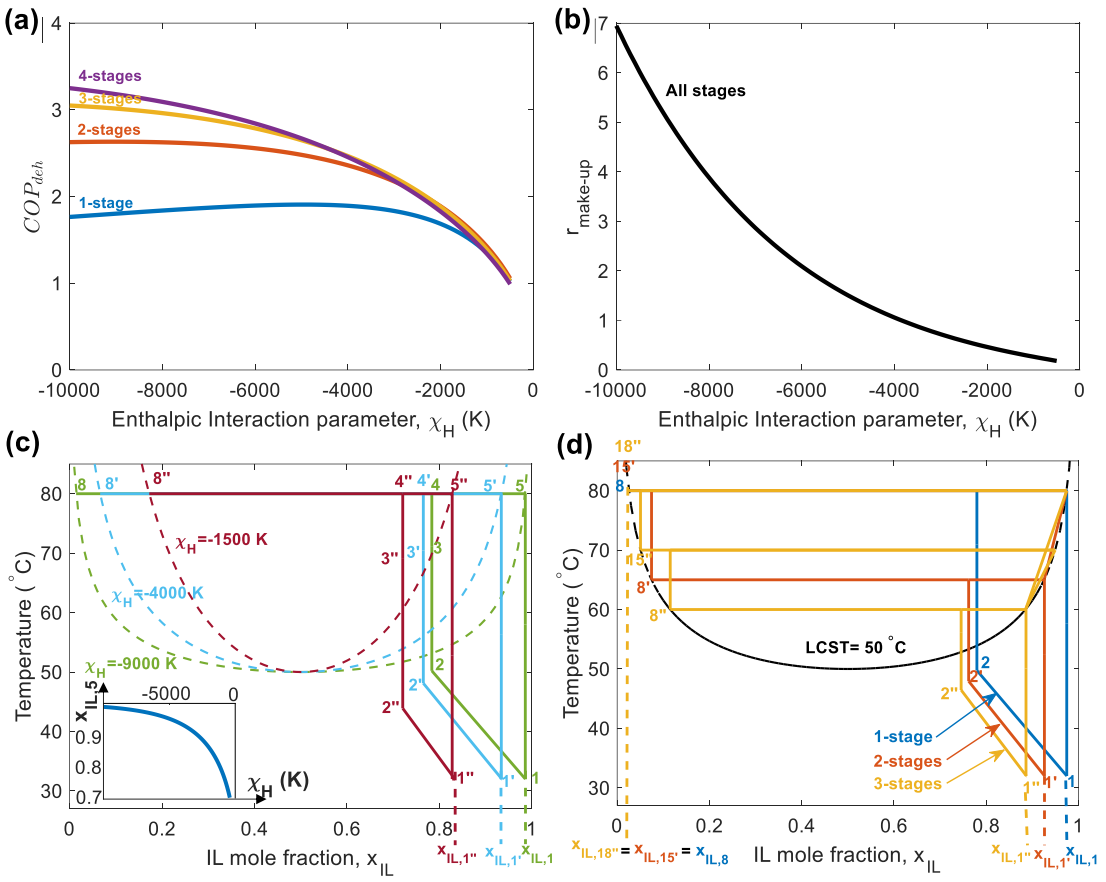

Figure 2-8: Effect of enthalpic interaction parameter, χ_H on (a) Dehumidification Coefficient of Performance, (b) makeup ratio for different regeneration stages, (c) phase diagram for χ_H =-9000K, χ_H = -4000 K and χ_H =-1500 K for a 1-stage regeneration cycle and (d) Phase diagram for the T_{LCST}=50 °C and χ_H = 9000 K for 1-stage, 2-stages and 3-stages regeneration

There is a scenario in which increasing the magnitude of χ_H can reduce COP_{deh} and this can be seen in the range of -10000 K < χ_H ≲ -4000 K for the 1-stage system in Figure 8a. In this range a very shallow decline in COP_{deh} is seen. This occurs because for fixed value of excess regeneration temperature ($\Delta T_{reg,exs}$ = 30 °C), it begins to operate in very steep parts of the immiscibility curve. As highlighted in Section 2.3.1.2, operating within

these pronounced segments of the immiscibility curve indicates functioning within a diminishing returns regime. In this regime, increasingly larger sensible heat inputs are needed to achieve increasingly smaller amounts of separation. Consequently, COP_{deh} is decreased even though better separation is achieved (in an absolute separation sense). When operating in this regime, reducing $\Delta T_{reg,exs}$ would improve COP_{deh} while still allowing for the benefits of higher magnitude χ_{H}. Alternatively, increasing the number of stages would diminish this effect in a positive manner because a smaller fraction of the IL solution would be operating in this very steep portion of immiscibility curve.

Figure 2-8a shows that increasing the number of regeneration stages increases COP_{deh} for $|\chi_{\mathrm{H}}|$ > 4000 K. The larger benefits of increased regeneration stages in this regime are due to operation in the steep portion of the immiscibility curve. The reductions in $\dot{Q}_{reg}$ are pronounced in this region since less mass flow rate is operating in these steep portions of the immiscibility curve. The negative effect of increasing regeneration stages is a dilutionary effect on $x_{IL,1}$ (Figure 2-8d), which decreases $\dot{m}_{abs}$ and has a negative effect on COP_{deh}. The dilutionary effect becomes pronounced for high curvature immiscibility curves ($|\chi_{\mathrm{H}}|$ < 4000 K) and counteracts the benefits of reduced $\dot{Q}_{reg}$ in a meaningful manner.

Figure 2-8b demonstrates that the makeup ratio, r_{makeup}, decreases as the magnitude of χ_{H} decreases. This can be directly visualized by the IL concentration at point 8 in Figure

2-8c. Larger values of $x_{IL,8}$ hurt r_{makeup} because more IL is lost during the separation process and hence more makeup IL is needed. Mirroring and compounding the effects of increases in $x_{IL,8}$, are decreases in $x_{IL,1}$ which decrease $\dot{m}_{abs}$ and also hurt r_{makeup}.

2.3.4. The Combined Effects of T_{LCST} and χ_H on System Performance

Figure 2-9 displays contour plots of COP_{deh} for continuously variable T_{LCST} and χ_{H} for 1-, 2-, 3, and 4-stage regeneration cycles. Generally speaking, lower LCST temperatures (that are still above the cycle's heat rejection temperature) are favorable for greater COP_{deh}. The optimum enthalpic interaction parameter for COP_{deh} changes as the number of stages changes. For 1-stage, the best χ_{H} is approximately -5000 K and this transitions to higher magnitudes (increasingly negative values) as the number of stages increases. The contour lines in Figure 2-9 tend to be more horizontal than vertical (especially at low T_{LCST} and higher magnitude χ_{H} values). This means that T_{LCST} has a more dominant effect on COP_{deh} than χ_{H} in these regions. A subtle change in contours occurs at T_{LCST} = 65 °C for 1-stage and this is a result of limiting the maximum regeneration temperature to 95 °C. This subtle change in the contours is not noticeable in the 2-, 3-, and 4-stage regeneration systems because a larger fraction of the regeneration process happens at lower temperatures.

Figure 2-10 demonstrates that $r_{make-up}$ improves as T_{LCST} decreases and as χ_{H} becomes increasingly negative. The contour lines in Figure 2-9b is mostly vertical. This

means that χ_{H} has a more dominant effect on r_{makeup} than T_{LCST}. Considering the effects of T_{LCST} and χ_{H} on COP_{deh} and r_{makeup}, it is desirable to operate in the lower left regions of these maps, in other words, low T_{LCST} and high $|\chi_{\mathrm{H}}|$. As noted earlier, r_{makeup} does not depend on the number of stages and so Figure 10 is only a 1-part figure that is equivalent for any number of stages.

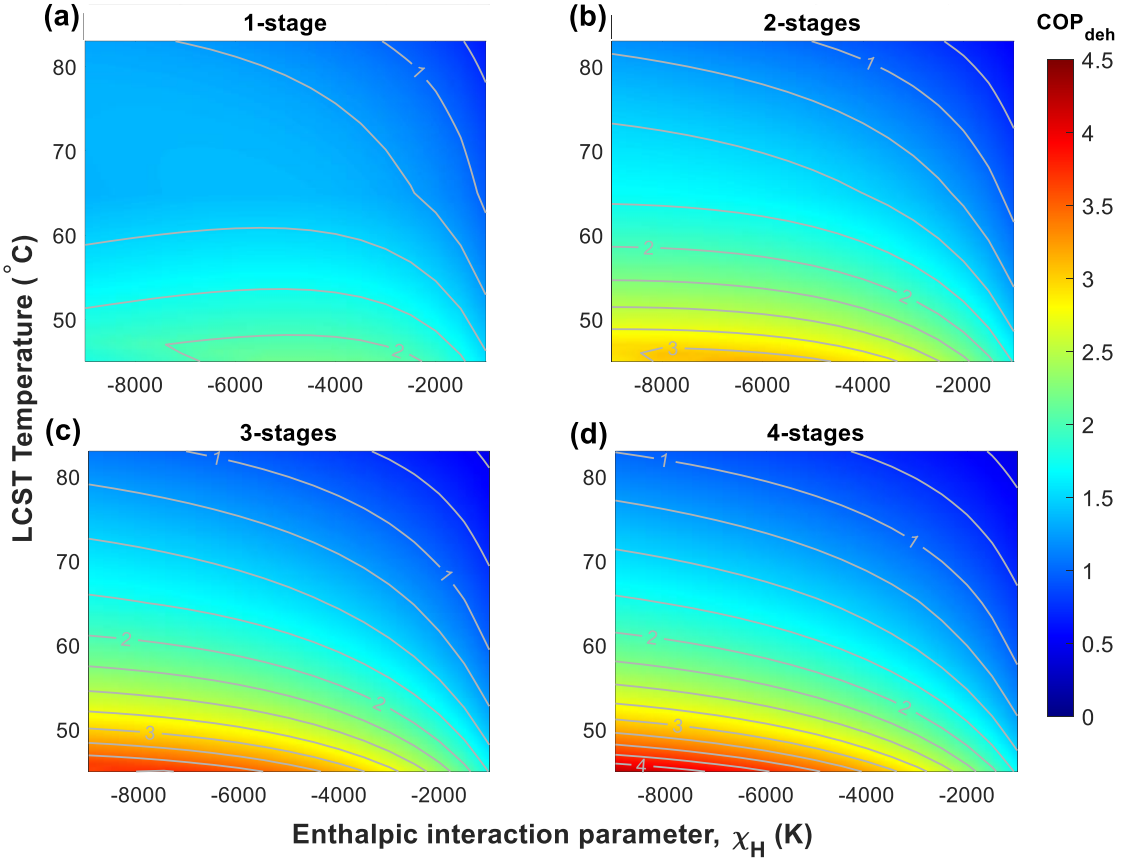

Figure 2-9: Contour plot of Dehumidification Coefficient of Performance for varying LCST temperature, T_{LCST} and enthalpic interaction parameter, χ_H for (a) 1-stage, (b) 2-stage, (c) 3-stage, and (d) 4-stage regeneration cycle

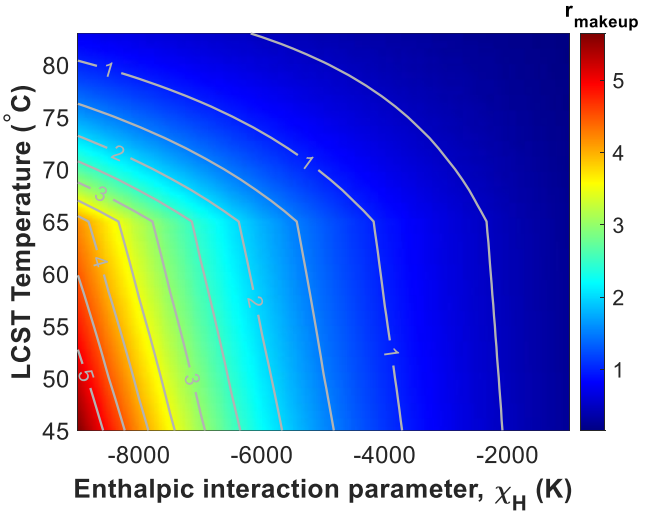

Figure 2-10: Contour plot of makeup ratio for LCST temperature and enthalpic interaction parameter, χ_H (for all stages)

2.3.5. Effect of Excess Regeneration Temperature

Due to the curvature of the immiscibility curve, some amount of excess regeneration temperature must be used to achieve separation. This section explores how varying this parameter effects COP_{deh} and $r_{make-up}$. One of the interesting findings is that there is an optimum value of $\Delta T_{reg,exs}$ when it comes to maximizing COP_{deh} (Figure 2-11a).

Figure 2-11c illustrates thermodynamic cycles for varying amounts of $\Delta T_{reg,exs}$. Several effects of increasing $\Delta T_{reg,exs}$ are visible: (i) the vertical length of line 3-4 increases, (ii) the magnitude of $x_{IL,1}$ increases, and (iii) the local slope of the immiscibility curve at point 5 increases. The effect of increasing line 3-4 represents an increase in $\dot{Q}_{reg}$, which hurts COP_{deh}. However, the effect of increasing $x_{IL,1}$ is to increase $\dot{m}_{abs}$ and help

COP_{deh}. Hence effect (i) and (ii) have competing effects on COP_{deh}.

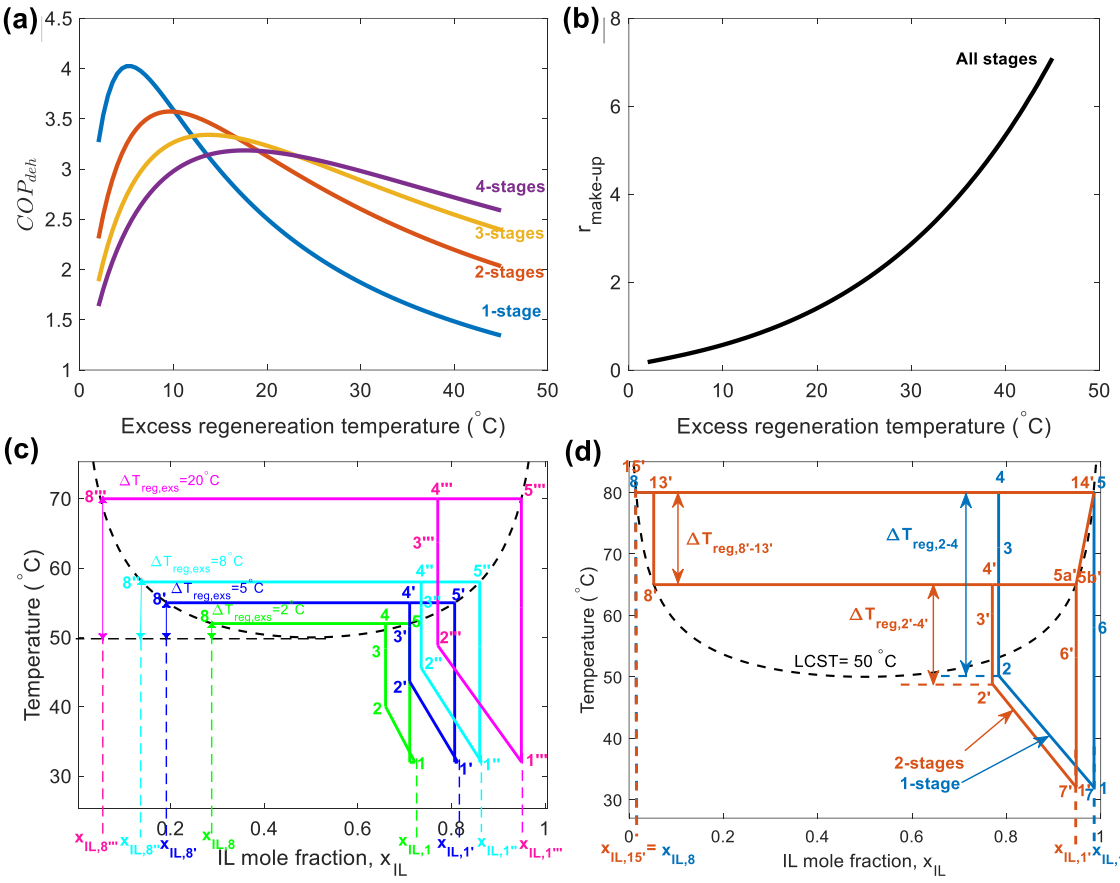

Figure 2-11: Effect of excess regeneration temperature, $\Delta T_{reg,exs}$ on (a) Dehumidification Coefficient of Performance, (b) makeup ratio for different regeneration stages, (c) phase diagram for $\Delta T_{reg,exs}$ = 2°C, $\Delta T_{reg,exs}$=5°C, $\Delta T_{reg,exs}$ = 8°C and $\Delta T_{reg,exs}$ = 20 °C for 1-stage regeneration cycles, (d) Phase diagram for 1-stage and 2-stage regeneration cycles at T_{LCST} =50 °C, χ_H =-9000 and $\Delta T_{reg,exs}$ =30 °C

Whether these competing results of effects (i) and (ii) have a net negative or net positive effect on COP_{deh} relates to effect (iii), which is the local slope of the immiscibility curve at point 5. As described in Section 2.3.1.2, the local slope of the immiscibility curve

represents the amount of demixing achieved for a differential sensible heat input. Hence flatter slopes in the immiscibility curve favor improved COP_{deh}. This slope is highly favorable towards the middle of the of the phase diagram (x_{IL} = 0.5) and unfavorable towards the edges of the phase diagram (x_{IL} = 0.0 or 1.0). This means that towards the middle of the phase diagram, increasing $\Delta T_{reg,exs}$ leads to increased COP_{deh}, and towards the edges of the phase diagram, increasing $\Delta T_{reg,exs}$ leads to decreased COP_{deh}. This then results the occurrence of an optimum $\Delta T_{reg,exs}$ with respect to COP_{deh} as seen in Figure 2-11a.

The effect that the local curvature in the immiscibility curve has on where the optimum $\Delta T_{reg,exs}$ occurs indicates that the choice of this system operational parameter strongly depends upon the enthalpic interaction parameter, χ_{H}. As mentioned in Section 2.3.1., the ideal immiscibility curve would be a perfectly horizontal line at the LCST temperature that spans across the full x_{IL} range and then turns 90 degrees to a vertical upward line at x_{IL} = 0.0 and 1.0. In this case, $\Delta T_{reg,exs}$ could be approximately zero because perfect phase separation would be achieved with a differential temperature increase above T_{LCST}. Although an immiscibility curve like that for liquid-liquid phase separations would not be possible in reality, this idea would serve as a useful concept to guide selection of thermoresponsive liquid desiccants for an actual cycle (and also explains why increasingly negative values of χ_{H} are favorable for performance).

Figure 2-11a also shows that increasing regeneration stages helps COP_{deh} for large $\Delta T_{reg,exs}$ and hurts for small $\Delta T_{reg,exs}$. The mechanism that leads to this behavior is similar to that described in Section 4.2 and 4.3. More specifically increasing regeneration stages leads to both positive and negative effects on COP_{deh}. Increasing regeneration stages helps by reducing $\dot{Q}_{reg}$, but also hurts by decreasing $\dot{m}_{abs}$ (which is visible by a decreasing $x_{IL,1}$ in Figure 2-11d). For large $\Delta T_{reg,exs}$, the reduction in $\dot{Q}_{reg}$ is the dominant effect on COP_{deh} whereas for small $\Delta T_{reg,exs}$, the reduction in $\dot{m}_{abs}$ is the dominant effect on COP_{deh}.

Figure 2-11b demonstrates that the makeup ratio, r_{makeup}, increases as $\Delta T_{reg,exs}$ increases. This can be directly visualized by the IL concentration at point 8 in Figure 2-11c. Larger values of $x_{IL,8}$ hurt r_{makeup} because more IL is lost during the separation process and hence more makeup IL is needed. Mirroring and compounding the effects of increases in $x_{IL,8}$, are decreases in $x_{IL,1}$ which decrease $\dot{m}_{abs}$ and also hurt r_{makeup}.

2.3.6. Comparison to a Non-Thermoresponsive Desiccant (nTRD) System

After a systematic examination of the core attributes of a thermoresponsive liquid desiccant cycle, a straightforward analysis is conducted to contrast this cycle with a non-thermoresponsive liquid desiccant cycle, which is essentially a conventional liquid desiccant cycle.

Figure 2-12 illustrates the schematic of our model for a non-thermo-responsive desiccant (nTRD) system. This system is similar to our single-stage cycle (Figure 2-3a) but does have some differences because regeneration does not occur via a liquid-liquid phase transition. Rather, regeneration occurs via a liquid-vapor phase transition of the water component in the desiccant solution. One difference is that our schematic for the nTRD system does not include a dedicated separator in the regeneration stage because the separation process happens extremely quickly due to the large density difference between the gaseous water and the liquid solution This system also does not require makeup IL solution because the vapor pressure of IL is very low and hence the vapor mass leaving the system can be approximated as pure water.

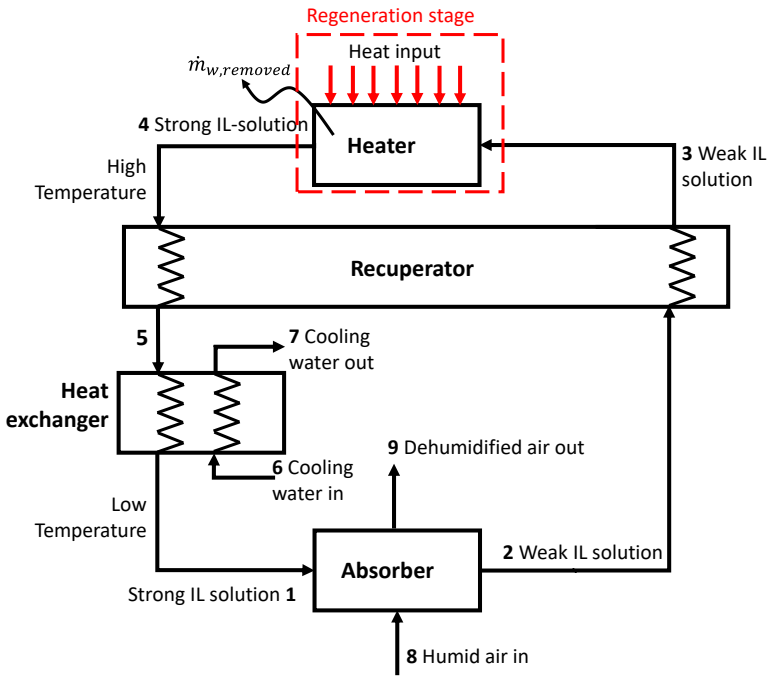

Figure 2-12: Schematic of a non-thermoresponsive desiccant (nTRD) dehumidification system

The regeneration heat of this nTRD model, $\dot{Q}_{reg,nTRD}$, is calculated as follows,

$$\dot{Q}_{reg,nTRD} = \dot{m}_3 c_{p,s}(T_4 - T_3) + \dot{m}_{w,removed} h_{fg} \quad (2\text{-}23)$$

The first term on the right represents the sensible heat input needed to raise the IL solution to the regeneration temperature (for which the boiling temperature of water, T_4 = 100°C is used). The second term on the right represents the latent heat needed to boil off the absorbed water from the solution mixture (h_{fg} is the enthalpy of vaporization for water).

In order to compare our thermoresponsive liquid cycle to this nTRD model, it is assumed that the nTRD cycle absorbs the same amount of water from the humid air as our LCST ionic liquid (for a given temperature and concentration). For this comparison, an ionic liquid with T_{LCST} = 50°C and χ_H = -9000 K is chosen.

Figure 2-13 compares COP_{deh} for the LCST system and nTRD system as a function of moisture absorption effectiveness ratio in the absorber (ε_{ma}). As ε_{ma} increases, it is seen that both LCST and nTRD systems have increasing COP_{deh}. However, the LCST case both outperforms the nTRD system and has a COP_{deh} that increases faster than the nTRD system. Figure 2-13 demonstrates the benefits of the LCST cycle relative to the nTRD case. While the nTRD COP_{deh} never exceeds 1, the LCST system achieves COP_{deh} in excess of 3 (and can approach even higher values for the different IL and system configurations investigated in the previous sections). A major driving force for this COP_{deh} improvement

is the fact that the nTRD system requires a large regeneration heat input due to water's very large enthalpy of vaporization. In contrast, the liquid-liquid phase transition in the LCST system requires a much smaller regeneration heat because the demixing enthalpy is much smaller than water's enthalpy of vaporization.

One drawback of the LCST IL system with respect to the nTRD cycle is that the LCST IL system does require makeup IL whereas the nTRD cycle does not. However, as noted in Section 4.1.3, alternative conceptions of this LCST cycle could be envisioned that recover the ionic liquid this is discarded with the water-rich phase leaving the separator (point 8 in Figure 2-3a). For instance, this water-rich solution could potentially be concentrated through evaporative cooling of the water and then re-introduced into the cycle. The more complicated conception of the cycle would have the added benefit of providing dehumidification and cooling and deserves future study.[59]

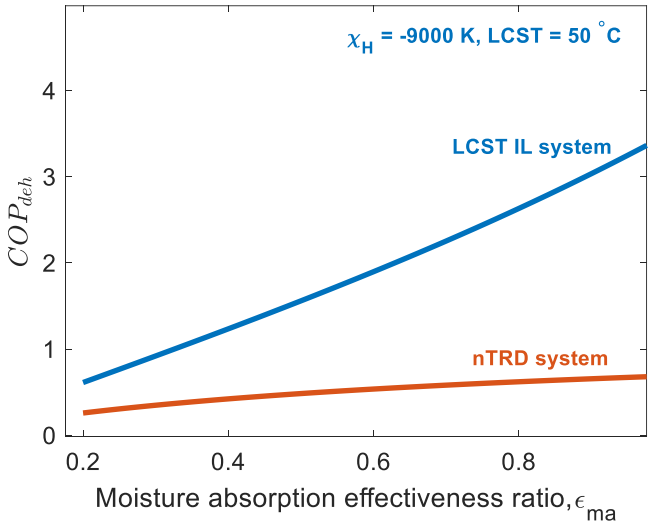

Figure 2-13: Comparison of COP_{deh} of a non-thermo-responsive desiccant (nTRD)

system and ionic liquid (IL) system for different values of moisture absorption effectiveness ratio, ε_{ma}

2.4. Summary

In this chapter a liquid desiccant dehumidification system is presented that improves COP_{deh} by regenerating via liquid-liquid phase transitions as opposed to liquid-vapor phase transitions. This COP_{deh} improvement arises because liquid-vapor phase transitions require large vaporization enthalpies whereas liquid-liquid phase transitions only require comparatively small demixing enthalpies. Analysis of the immiscibility curve impact on COP_{deh} using the Flory-Huggins theory of mixing indicates that LCST temperatures near the cycle's heat rejection temperature and increasingly negative enthalpic interaction parameters generally favor increased COP_{deh}. In other words, immiscibility curves that are flatter and occur at lower temperatures are generally favorable. This work represents an initial step towards exploring the potential of liquid thermoresponsive LCST cycles and more work is needed. Analyzing this system on the basis of the 2nd law of thermodynamics would provide further insight into how this cycle can be improved. With this in mind, Section A.3 in Appendix A presents some initial efforts in this direction. Experimental proof-of-concepts for this cycle would be helpful. In addition, identifying and/or creating specific liquid desiccants that simultaneously achieve low LCST temperatures and increasingly negative enthalpic interaction parameters is a non-trivial task. Lastly,

investigations of LCST cycles that recover the ionic liquid from the water-rich phase would be valuable (*i.e.*, thereby eliminating the need for makeup ionic liquid).

3. ANALYTICAL MODELLING ABSORPTION OF WATER VAPOR ON A POLYMERIC THIN FILM

3.1. Introduction

In the preceding chapter, the dehumidification potential of thermoresponsive liquid desiccants was examined, revealing significant advantages over conventional desiccant systems. Despite these benefits, thermoresponsive liquid desiccants remain under-researched in experimental settings, necessitating a significant leap to develop a functional dehumidification system based on them. Consequently, attention is now directed towards thermoresponsive solid desiccants. Although they have been studied more than their liquid counterparts, comprehensive research on them remains limited.

This chapter delves into modeling thermoresponsive polymer desiccants using the Vrentas-Vrentas [72] theory of mixing. The Flory-Huggins theory [61,62], while offering insights into polymer-solvent interactions, is based on a liquid-like state and does not fully capture the nuances of water absorption in glassy polymers. Beyond thermodynamic modeling of the absorption process, this chapter also offers a glimpse into the kinetics of absorption by thin film thermoresponsive polymer films, with water diffusion kinetics modeled using Fick's equation.

Insights are provided on absorption by polymeric films under various conditions and

with distinct polymer properties. New polymers are modeled drawing inspiration from a well-known thermoresponsive polymer, PNIPAAm, and by adjusting fundamental properties such as LCST temperature and interaction parameters. Recommendations are made regarding optimal parameter values, including LCST, interaction parameter, and film thickness, which will be utilized in the subsequent chapter for the finite element design of the dehumidifier.

3.1.1. Background of Glassy Polymers

In polymer science, the glass transition temperature, T_g, plays a pivotal role in determining a polymer's mechanical behavior. As a polymer's temperature descends below its T_g, it adopts a brittle character. Conversely, when heated above its T_g, it exhibits a rubbery nature. This temperature-dependent behavior greatly influences material selection for diverse applications.

The underlying behavior can be attributed to the structural intricacies of glassy materials. These materials often consist of elongated molecular chains, atom-linked networks, or possess complex molecular structures. In their liquid state, such materials are highly viscous but free to flow. When cooled the mobility of the chains is reduced and we enter a rubbery state with limited mobility. When the cooling continuously, there is subtle change in slope of the specific volume curve, and we enter into the glassy region. The

temperature where this occurs is called glass transition temperature. In the glassy state, polymer is more rigid, brittle and polymer chains have very limited mobility.

The interaction between polymer and water in the glassy region is different than in the rubbery and liquid region. In the glassy state, there is elastic energy stored in the polymer which does not happen in rubbery or liquid state. To account for this stored elastic energy, the Vrentas-Vrentas model has been developed to cover the water absorption by a polymer in the glassy region. The next section will explain the modelling of absorption using this theory.

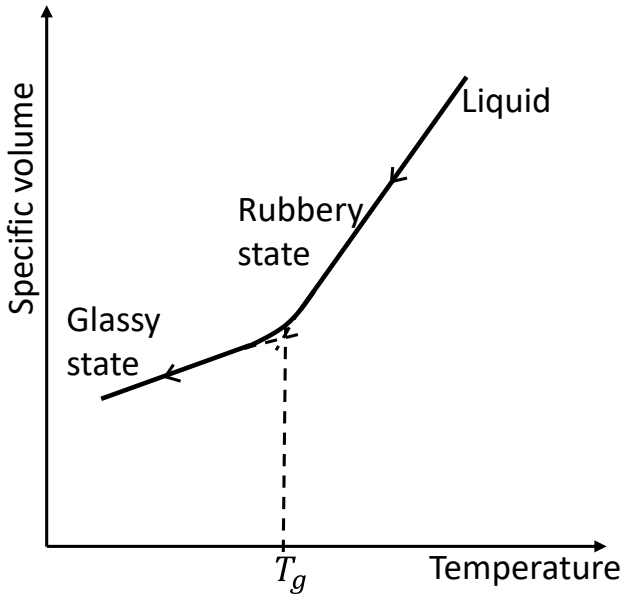

Figure 3-1: Schematic representation of the glass transition temperature showing specific volume change with temperature.

3.2. Modelling and Methodology

In this section, absorption isotherms derived from the Vrentas-Vrentas model, combined with kinetic equations, will be employed to model the absorption process in a thin polymeric film.

3.2.1. Modeling Absorption on a Thin Film Polymer on a Substrate

The absorption behavior of glassy polymers can be modelled using the Vrentas-Vrentas model[72]. This model is a modified version of Flory-Huggins theory[61,62] that takes into account the elastic energy stored in the polymer during absorption. According to Vrentas-Vrentas model for the polymer-water mixture, the sorption isotherms can be given by the Equation (3-1)[72].

$$\phi_1 \, exp\left(\phi_2 + \chi {\phi_2}^2 + F\right) = \frac{p_1}{p_1^0} \tag{3-1}$$

In the above the Equation the ϕ_1 and ϕ_2 are the volume fractions for water and the polymer in the polymer-water mixture at temperature T and relative humidity equivalent to $\frac{p_1}{p_1^0}$. Also χ, is the F-H interaction parameter between water and polymer molecules. As reference, we have used χ for the widely known LCST polymer poly(NIPAAm), and which was determined by Bae et al[73] as shown in Figure 3-2. Later $\chi(T)$ is altered to change polymer absorption properties.

It should be noted that the experimentally determined by Bae et al [73] where the polymer was immersed in water and not when the polymer is absorption water vapor from air at different relative humidities. Therefore, due to lack of the availability of literature for the interaction parameter at different relative humidity, we have assumed it to be a function of only temperature. It's important to note that the calculated isotherms for poly(NIPAAM) likely will not match experimentally determined isotherms in literature for interactions with humid air. Despite the drawbacks of using this interaction parameter with liquid water, we proceed to use it so that system-level considerations for thermoresponsive polymers in dehumidification systems can be explored. While the exact polymer properties are not known, proceeding in this manner helps address the question of "If it works, will it matter?" Moreover, since suitable thermoresponsive polymers for dehumidification have not yet been identified, this exploration should help provide appropriate target properties for polymer exploration within this application space.

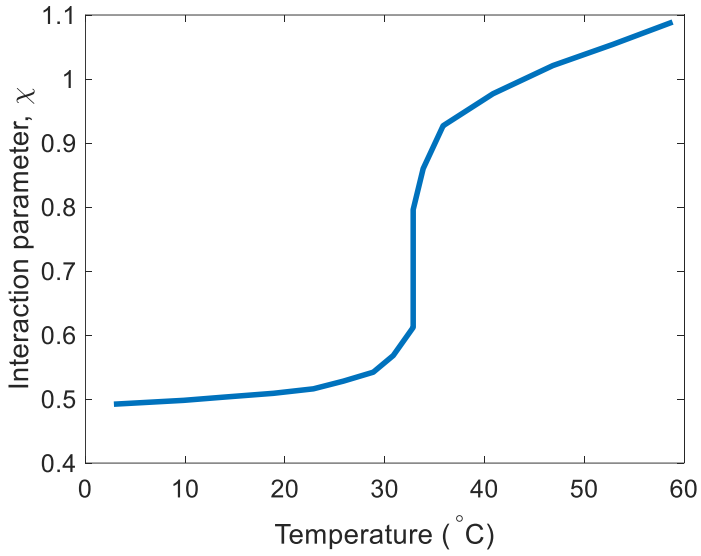

Figure 3-2: Interaction parameter of poly(NIPAAm)-water mixture. (Reproduced with permission from Bae et al.[73], Copyright 2003 Journal of Polymer Science Part B: Polymer Physics)

The *F* parameter in Equation (3-2) accounts for the deformation of the polymer during absorption given by the following Equation (3-2).

$$F = M_1\omega_2^2(c_{pg} - c_p)\left(\frac{dT_{gm}}{d\omega_1}\right)\left(\frac{T}{T_{gm}} - 1\right)/RT \qquad (3\text{-}2)$$

Where M_1 is the molecular mass of water, ω_2 is mass fraction of polymer in the polymer-water mixture, T_{gm} is the glassy transition temperature of the polymer-water mixture, R is universal, T is the temperature, and $(c_{pg} - c_p)$ is the difference in specific heat of the glassy and the rubbery polymer. Finally, $\frac{dT_{gm}}{d\omega_1}$ is the change in the glassy temperature of the mixture with respect to the mass fraction of the water in the mixture. Glassy temperature of the polymer-water mixture, T_{gm} is determined using Fox Equation

[74]:

$$\frac{1}{T_{gm}} = \frac{\omega_1}{T_{g1}} + \frac{\omega_2}{T_{g2}} \tag{3-3}$$

Figure 3-3 shows the glass transition of the polymer-water mixture against volume fraction of pure polymer in the mixture. To calculate T_{gm} using Equation (3-3), an average glass transition temperature of T_{g2} =132 ℃ [75,76] is used for poly(NIPAAm) and for water, T_{g1} = -137.15 ℃ [77] is used. It is observed that as the volume fraction of polymer reduces (it absorbs more water), T_{gm} also decreases. T_{gm} is crucial in determining the F-parameter value in Equation (3-2). The F-parameter value determines whether the mixture is in the glassy or rubbery state.

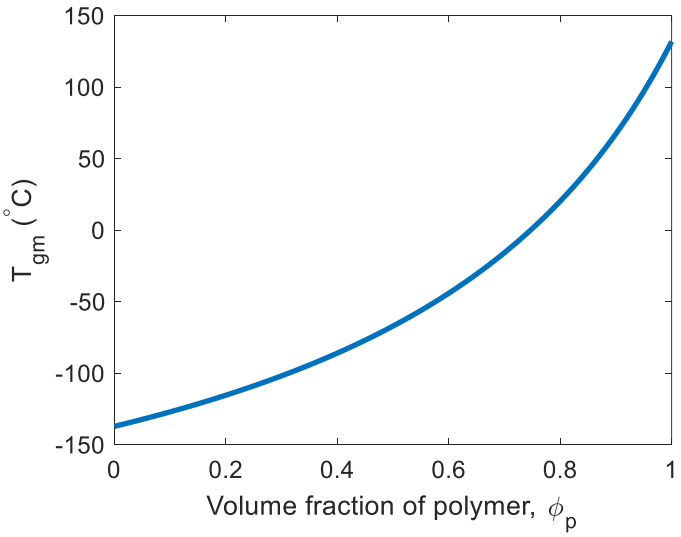

Figure 3-3: Glass transition temperature of poly(NIPAAm)-water mixture at different volume fractions

It is interesting to see how F varies with temperature and the volume fraction. Figure 3-4 shows how F looks at different temperatures for poly(NIPAAM)-water mixture. As the polymer absorbs more water, the mixture moves closer to being a rubbery polymer. When glass transition temperature of the mixture T_{gm}, becomes smaller than temperature of the polymer, it becomes a rubbery polymer and F = 0 for rubbery polymers. Beyond this point, by definition for $T \geq T_{gm}$, $F = 0$ and Vrentas-Vrentas model reduces to Flory-Huggins theory of mixtures.

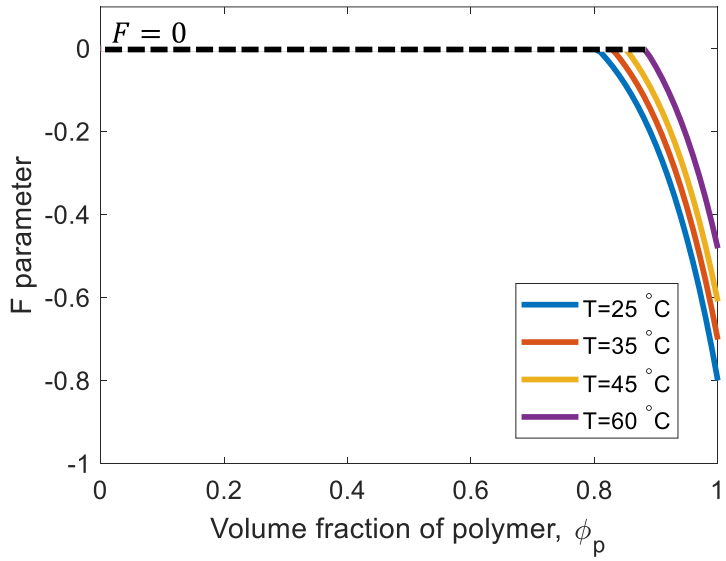

Figure 3-4: F parameter at different polymer volume fraction at different temperatures for poly(NIPAAm)-water mixture

The desorption process may not always follow the same path as the absorption path and therefore there is always a hysteresis between the absorption and desorption process. But we have assumed the same isotherm for both absorption and desorption because

isotherm can even change from cycle to cycle and the difference is often not appreciable.

3.2.2. Kinetics of Absorption/Desorption by Polymeric Films

Consider a polymeric film on a metallic substrate as shown in Figure 3-5. The polymeric side is exposed to the air at the temperature and relative humidity.

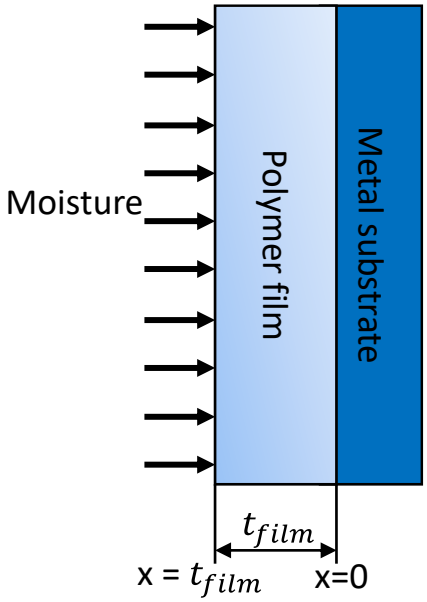

Figure 3-5: Schematic of moisture absorption by a polymeric film

The water diffusion within the polymeric film is calculated using Ficks law. Ficks equation for concentration within the polymeric film with time is shown in Equation (3-4). In this equation, c (mol/m^3) is the concentration of the water in the polymer-water mixture, D (m^2/s) is the water diffusion coefficient within the polymeric film.

$$\frac{\partial c}{\partial t} = D\,\frac{\partial^2 c}{\partial x^2} \tag{3-4}$$

Since thermal diffusivity, $k/\rho c_p$ is many orders of magnitude greater than mass diffusivity, D, the absorption process is assumed to occur at a constant temperature. There is coupling of the heat equation and diffusion equation in this chapter. However, in the next chapter, the polymeric film is cooled using a cooling fluid for the duration of the absorption process.

The boundary conditions for concentration for the polymeric film are as follows. The Equation (3-5) shows set the initial concentration to c_i. On the side where film is exposed to ambient, the concentration is dependent on water vapor concentration in air (c_a). It is depending on relative humidity (RH) and air temperature (T_{amb}) and polymer temperature and is obtained from the Vrentas-Vrentas model described above. On the substrate side, no water can escape through the metal substrate and hence there is no change in concentration.

$$c = c_i, \qquad 0 < x < t_{film}, \qquad t \leq 0 \tag{3-5}$$

$$c = c_a \qquad x = t_{film}, \qquad t > 0 \tag{3-6}$$

$$\frac{\partial c}{\partial x} = 0, \qquad x = 0, \qquad t > 0 \tag{3-7}$$

The solution of the Equation (3-4) with boundary (3-5)-(3-7) is given by Crank [78] in the following equation.

$$\frac{c(t) - c_i}{c_\infty - c_i} = 1 - \frac{4}{\pi}\sum_{n=0}^{\infty}\frac{1}{(2n+1)}exp\left(-\frac{D_x(2n+1)^2\pi^2 t}{4{t_{film}}^2}\right)sin\left(\frac{(2n+1)\pi x}{2t_{film}}\right) \tag{3-8}$$

It is not possible to measure the concentration of the water in the polymeric film at every position. Therefore, the total amount of moisture present in the film is used. The total weight of the moisture in the film is obtained by integrating concentration in Equation (3-8) over the polymeric film thickness.

$$M = \int_0^H c\, dx \tag{3-9}$$

The result of this integration is the following [78]

$$G \equiv \frac{M(t) - M_i}{M_\infty - M_i} = 1 - \frac{8}{\pi^2} \sum_{n=0}^{\infty} \frac{1}{(2n+1)^2} exp\left(-\frac{D(2n+1)^2 \pi^2 t}{4{t_{film}}^2}\right) \tag{3-10}$$

Simplifying above Equation in terms of the moisture content at given time *t*, $M(t)$ and saturation moisture content, M_∞. This equation gives us the moisture uptake in a polymer at the any given time ($M(t)$) with known initial water content (M_i) in the polymer, M_∞ is water content at saturation and D and is diffusion coefficient.

$$\frac{M(t)}{M_\infty} = \left(\frac{M_i}{M_\infty}\right) + \left(1 - \frac{M_i}{M_\infty}\right) G \tag{3-11}$$

The unknowns in Equation (3-11) are diffusion coefficient, D, initial water content in the polymer (M_i) , water content at saturation (M_∞) and water content at time t, $M(t)$. The diffusion coefficient is obtained from literature for a particular polymer-water pair. M_i and M_∞ can be obtained from the Vrentas-Vrentas model explained in the earlier section. M_i is obtained by knowing the temperature and relative humidity of the conditions in which the

polymer was stored whereas M_∞ is obtained in the similar manner by using the temperature and relative humidity of the air during absorption.

3.3. Results and Discussion

3.3.1. Changing Polymer Properties (LCST Temperature And Interaction Parameter)

Polymer properties, including LCST and interaction parameters, play a pivotal role in dictating the temperature-dependent behavior of a polymer. To understand this better, the empirically determined interaction parameter curve presented in Figure 3-2 is analyzed. This curve was segmented into three distinct regions, and linear regression was applied to each segment. Figure 3.6 juxtaposes the experimental curve with the modeled curve for poly(NIPAAm).

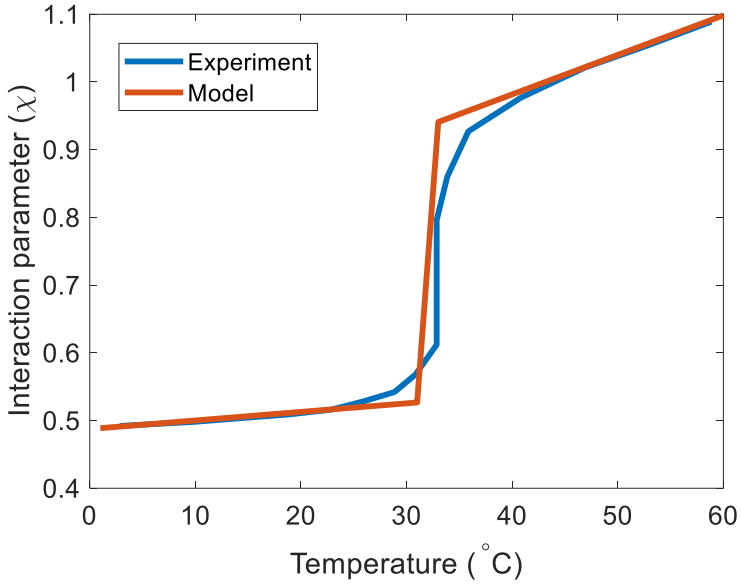

Figure 3-6: Temperature dependent interaction parameter for poly(NIPAAm) with LCST of 32 ℃ modelled using regression.

The absorption capacity of the polymer can be altered by adjusting the interaction curve in the region of the LCST. Changing the LCST involves shifting the curve either to the left or right. Figure 3-7 displays the χ(T) curve for polymers with varying LCST temperatures. The modeled curve for poly(NIPAAm) has been shifted to the right to represent higher LCST temperatures. Ideally, an LCST higher than the air temperature is preferred to ensure that absorption or heat transfer with the air doesn't push it into the hydrophobic region.

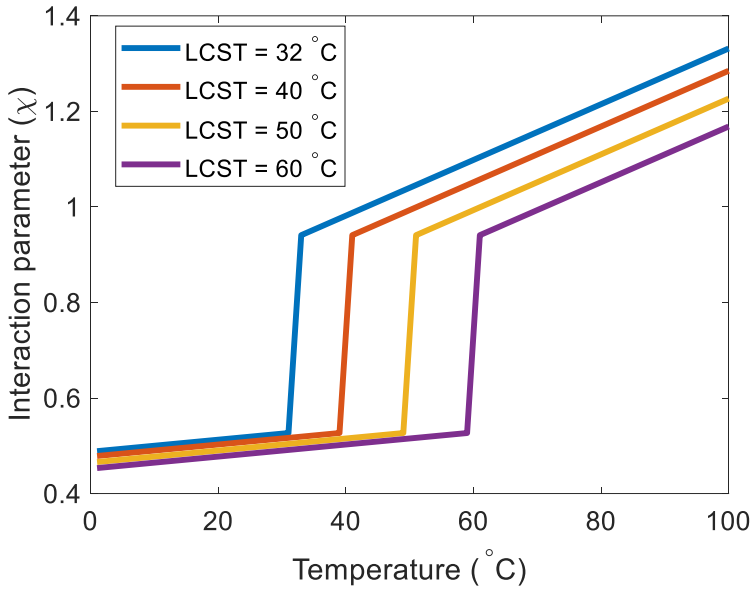

Figure 3-7: Changing LCST using the regression model.

The absorption capacity of the polymer is altered by adjusting the interaction parameter in the absorption region. This adjustment involves shifting the curve in this region by various offset values, denoted as Δχ. The aim is solely to enhance absorption capacity, so

the curve is only shifted downward. For PNIPAAm, the default is $\Delta\chi = 0$. For more absorbent polymers with identical LCST temperatures, $\Delta\chi$ assumes increasingly negative values. Figure 3-8 illustrates the variation in $\chi(T)$ for the different polymers examined in this section.

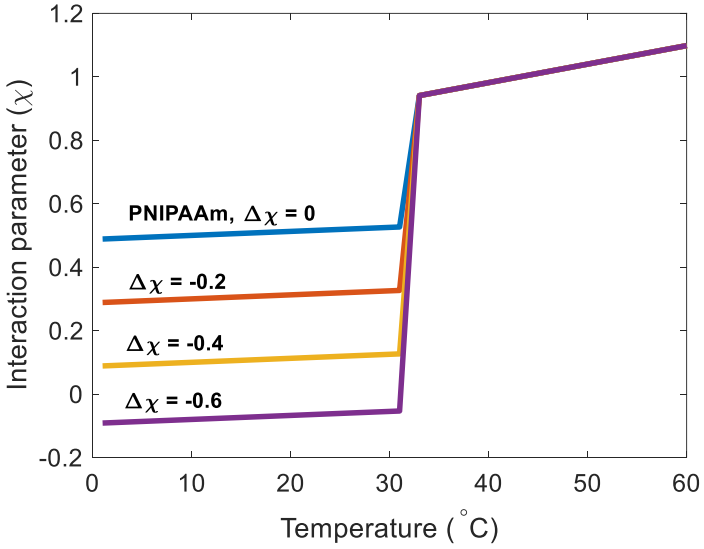

Figure 3-8: Changing interaction parameter using the regression model

3.3.2. Effect of T_{LCST} and $\Delta\chi$ on Absorption Capacity

The absorption capacity of a polymer is defined as the quantity of water it can absorb at saturation per unit mass of the dried polymer, represented by M_∞ in Equation (3-10). Figure 3-9 presents a contour plot depicting the absorption capacity of the polymer across different $\Delta\chi$ and T_{LCST} values, with a relative humidity set at 75% and an absorption temperature of T_{LCST}-15 °C. The plot reveals that both a lower T_{LCST} and a lower $\Delta\chi$ result

in a higher absorption capacity. However, $\Delta\chi$ has a more pronounced effect than T_{LCST}, as indicated by the more vertical orientation of the contour lines.

A drawback of a low $T_{LCST}$is the potential need for absorption to occur at temperatures significantly below T_{LCST}. Maintaining such low temperatures might necessitate active refrigeration, especially when relying on outdoor ambient temperatures isn't feasible. For a polymer like PNIPAAm, which has a T_{LCST} of 32 ℃, the ambient air temperature often exceeds 32 ℃. This can cause the polymer's temperature to surpass its LCST, a scenario that's especially likely in warmer regions or during system startup when indoor and outdoor temperatures align. Hence, in most situations, a polymer with a T_{LCST} higher than the ambient air temperature is preferred, allowing the polymer's temperature to stay below its LCST without active cooling. An LCST of approximately 50 ℃ is considered ideal.

While a lower $\Delta\chi$ is generally more desirable, its exact value will be influenced by the polymer's hygroscopic nature. For this study, a $\Delta\chi$ resulting in 1.5 times the absorption capacity at an LCST of 50 ℃ was selected, which corresponds to $\Delta\chi$ = -0.5. Therefore, in the subsequent chapter, the reference polymer will have an LCST = 50 ℃ and $\Delta\chi$ = -0.5. We acknowledge that this is a conservative choice for the polymer since there are already hygroscopic polymers with higher moisture absorption capacity than 1 $g_{H2O}/g_{dry\text{-}pol}$. But such polymers are Interpenetrating Polymers (IPNs) synthesized with PNIPAAm with LCST of 32 ℃. But we have also tested thermoresponsive polymers (TRPs) with higher

moisture absorption capacity than 1 in the next chapter.

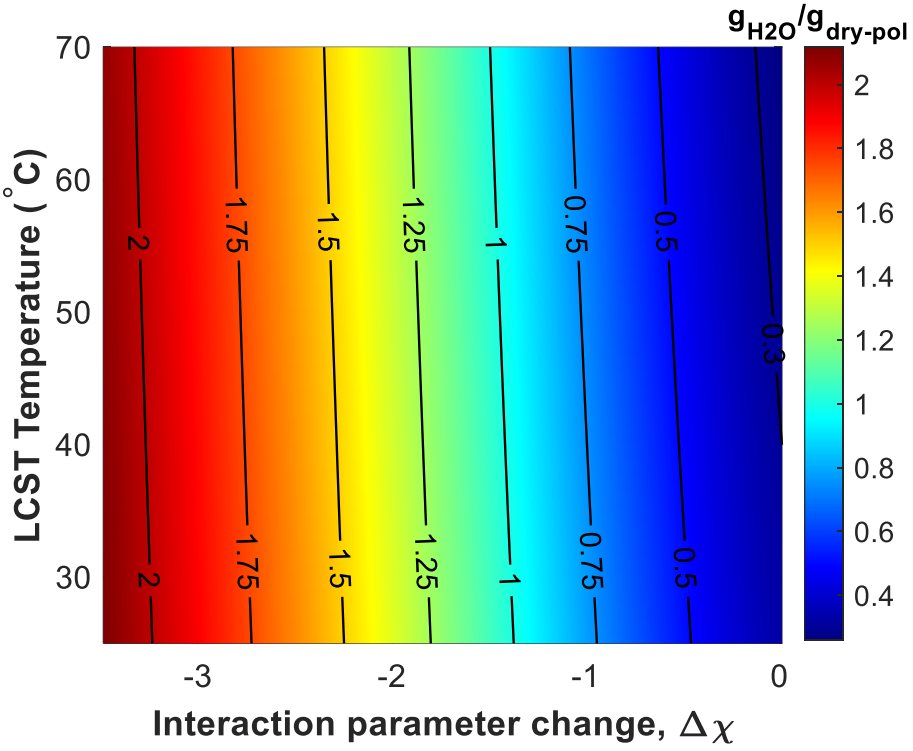

Figure 3-9: Contour plot showing moisture absorption capacity at different T_{LCST} and Δχ and relative humidity of 75%

3.3.3. Absorption Kinetics at Default Input Parameters

Table 3-1: List of default input parameters to the absorption model

Parameter	**Value**
Air relative humidity (RH)	0.75
T_{LCST} (°C)	32
Δχ	0 (PNIPAAm)
Absorption temperature, T_{abs} (°C)	T_{LCST}-15
Polymer film thickness, t_{pol} (μm)	100
Moisture diffusivity, D (m^2/s)	2 x 10^{-11}

We have used the default polymer to be PNIPAAm with T_{LCST} of 32 °C and Δχ of 0. The air relative humidity is taken to be 75% and a film thickness of 100 μm is

used. A constant average value for moisture diffusivity is 2 x 10^{-11} m^2/s obtained from literature[79,80]. Figure 3-10 shows the moisture uptake in the polymer at different temperatures which is calculated using Equation (3-11). It is observed that the moisture absorption decreases considerably as we go beyond the LCST temperature of 32 °C for PNIPAAm.

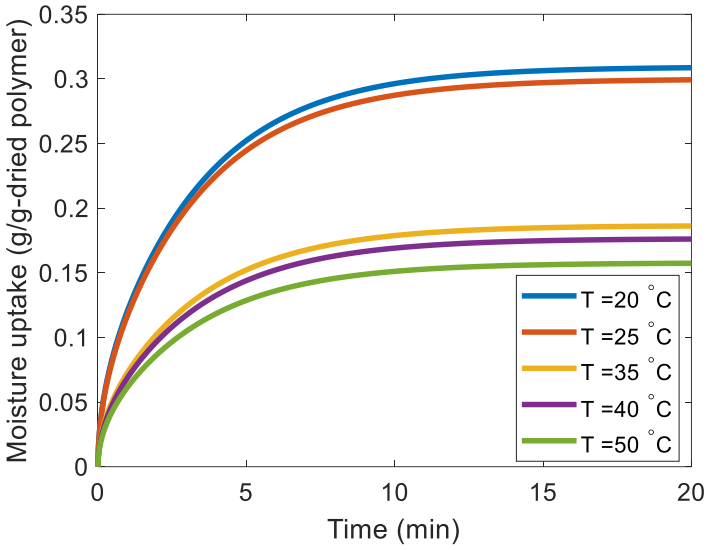

Figure 3-10: Moisture uptake in a poly(NIPAAm) polymeric film at different temperature and relative humidity of 75%

3.3.4. Effect of Polymer Film Thickness on Absorption Capacity and Kinetics

Figure 3-11 shows that thickness of the polymer film has an effect on the kinetics of absorption. The absorption time constant for diffusion typically varies as thickness squared and a similar behavior is evident in Figure 3-11. A 10 μm film saturates almost instantaneously whereas the 100 μm film saturates in about 15 minutes. Moreover, the rate

of absorption is faster in the beginning and then continues to slow down as time passes. We can see this clearly in Figure 3-11 for the 250 µm film which may take a long time to each saturation but also not be absorbing much water in that time rendering it useless for practical purpose. Therefore, the choice of film thickness is an important one while designing your dehumidifier. A 100 µm is chosen as the default film thickness and operated it for 90% of saturation time before switching to desorption process. This will be explained in detail in the next chapter.

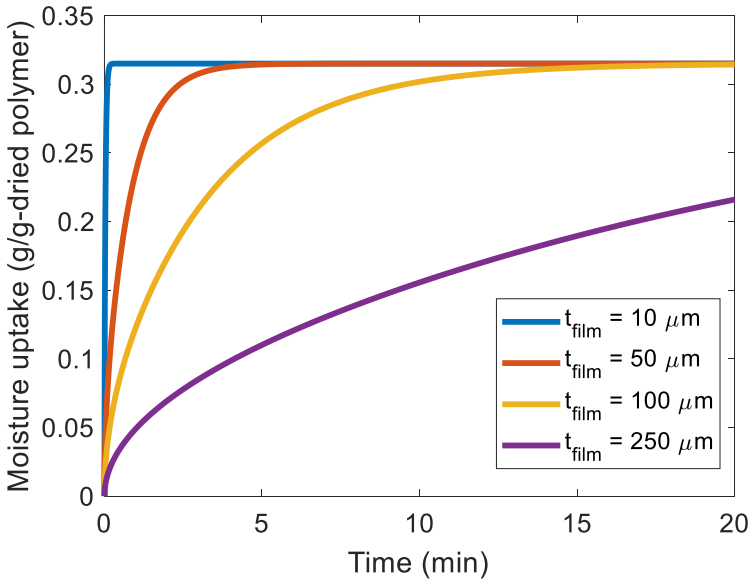

Figure 3-11: Moisture uptake at different polymer film thickness for poly(NIPAAm) at relative humidity of 75% at polymer temperature 17 ℃

3.3.5. Effect of Air Relative Humidity

As observed in Figure 3-12, the relative humidity of the air doesn't influence the

absorption kinetics. However, a higher relative humidity indicates more water in the air, leading to a significant increase in the water absorbed by the film as the relative humidity rises. Thus, it can be concluded that the polymer film in the desiccant dehumidifier will be more effective on days with high relative humidity. Nonetheless, it's essential to consider the desorption work, factoring in the energy needed to extract liquid water from the polymer film.

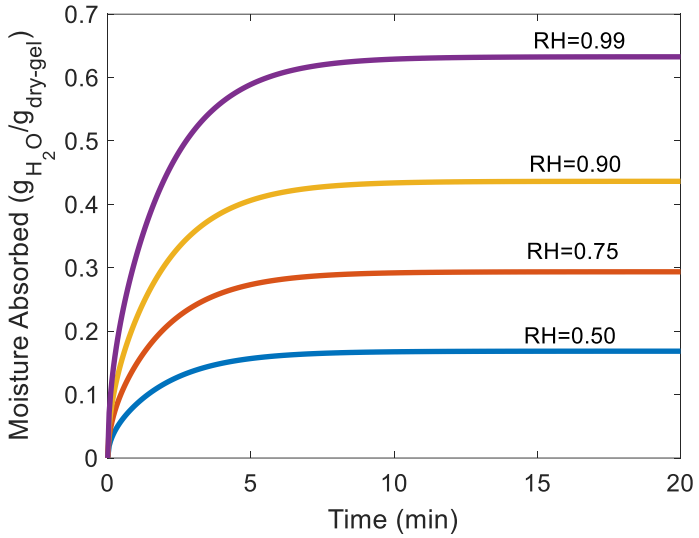

Figure 3-12: Moisture absorption by a polymeric film at different relative humidities with time for a 100 μm thick film

Figure 3-13 illustrates the absorption capacity of a polymer across varying temperatures and relative humidities. Notably, temperature plays a crucial role in the transition region, resulting in a swift change in absorption capacity both below and above the LCST temperature. However, outside of this transition region, the temperature's influence

diminishes, with minimal effects observed in both hydrophilic and hydrophobic regions. In contrast, the impact of relative humidity is more pronounced, showing a non-linear surge in absorption capacity as relative humidity rises.

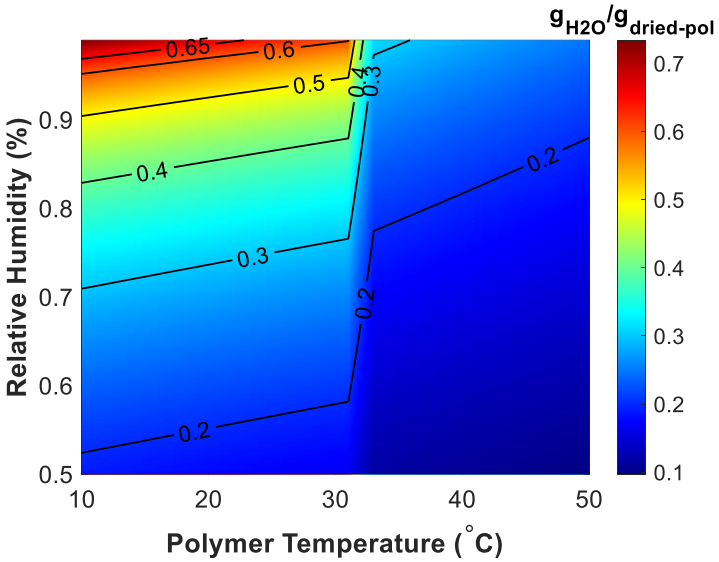

Figure 3-13: Contour plot showing moisture absorption capacity at different polymer temperature and relative humidities for PNIPAAm polymer.

3.4. Summary

This chapter delved into the water absorption process of thermoresponsive polymeric films, utilizing the Vrentas-Vrentas model. This model enhances the Flory-Huggins theory for mixtures by incorporating the elastic Gibbs free energy component into the mixing Gibbs free energy. This addition is particularly crucial for thermoresponsive polymers, especially when they are in a glassy state.

With this refined model tailored for the polymer in question, the absorption process

within the thermoresponsive polymer was examined. This was achieved by determining the absorption capacity through the Vrentas-Vrentas isotherm and correlating it with water diffusion within the polymer. While this model offers valuable insights into absorption dynamics within thermoresponsive polymers, it doesn't perfectly mirror actual absorption. Nevertheless, it serves as a foundational tool in the subsequent chapter, guiding the design of a thermoresponsive dehumidifier that employs a thin film polymer as the desiccant.

For the upcoming chapter, the default parameters selected are an LCST temperature of 50 °C, an interaction parameter of $\Delta\chi$ = -0.5, and a polymer film thickness of 100 μm. The choice of polymer is conservative with polymer having only 1.5 times absorption capacity of the PNIPAAm. The choice was somewhat intentional to avoid simulating a polymer that may be too far from reality in terms of LCST and absorption capacity. But other more absorbent TRPs with more negative $\Delta\chi$ showed absorption capacity as high as 2 $g_{H2O}/g_{dry\text{-}pol}$.

4. FINITE ELEMENT ANALYSIS OF A THERMORESPONSIVE DEHUMIDIFIER

4.1. Introduction

The Vrentas-Vrentas model adeptly captures the absorption dynamics of a thin film, shedding light on the absorption characteristics of a thermoresponsive polymer. Yet, its application in a dehumidifier designed for air conditioning remains unclear. To address this, a finite element analysis (FEA) model is introduced, providing a detailed perspective on an actual thermoresponsive dehumidifier.

A dehumidification system is suggested that employs a thermo-responsive polymer as the desiccant. This system absorbs water vapor from humid air and releases liquid water, a departure from the typical method of vaporizing it as water vapor to regenerate the desiccant. The dehumidifier design draws inspiration from a car radiator, as depicted in Figure 4-1. Humid air navigates through channels, the walls of which are composed of thin polymeric films. To optimize the water vapor absorption by the polymeric film, a coolant circulates, maintaining the polymer's temperature below its LCST. The specific dehumidifier explored in the model is illustrated in Figure 4-2. It features rectangular air channels for the dehumidified air's passage. These channels are constructed from aluminum sheets coated with a thin thermoresponsive polymeric film. A cooling fluid flows through

channels perpendicular to the air channels, cooling the polymeric film. During the regeneration or desorption process, this cooling fluid is substituted with a heating fluid.

This chapter showcases the operation of a dehumidifier that utilizes a thermoresponsive polymer as its desiccant, capable of absorbing water vapor from the air and releasing liquid water. The chapter elucidates the dehumidifier's functionality based on input parameters and underscores the significance of these parameters in determining the dehumidifier's performance.

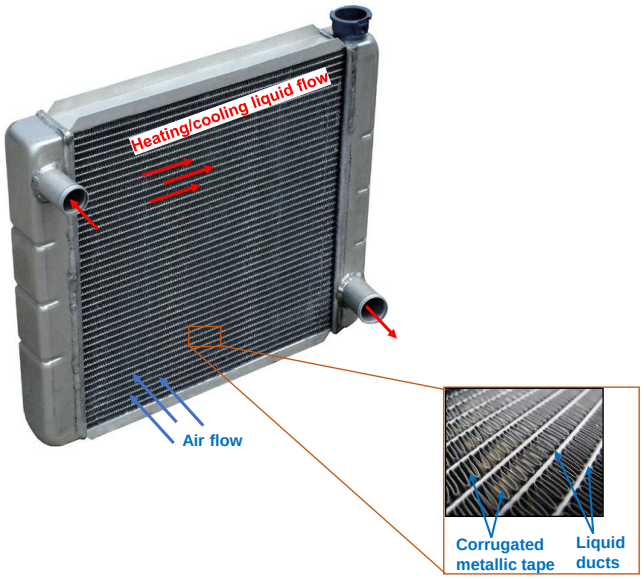

Figure 4-1: A car radiator[81]

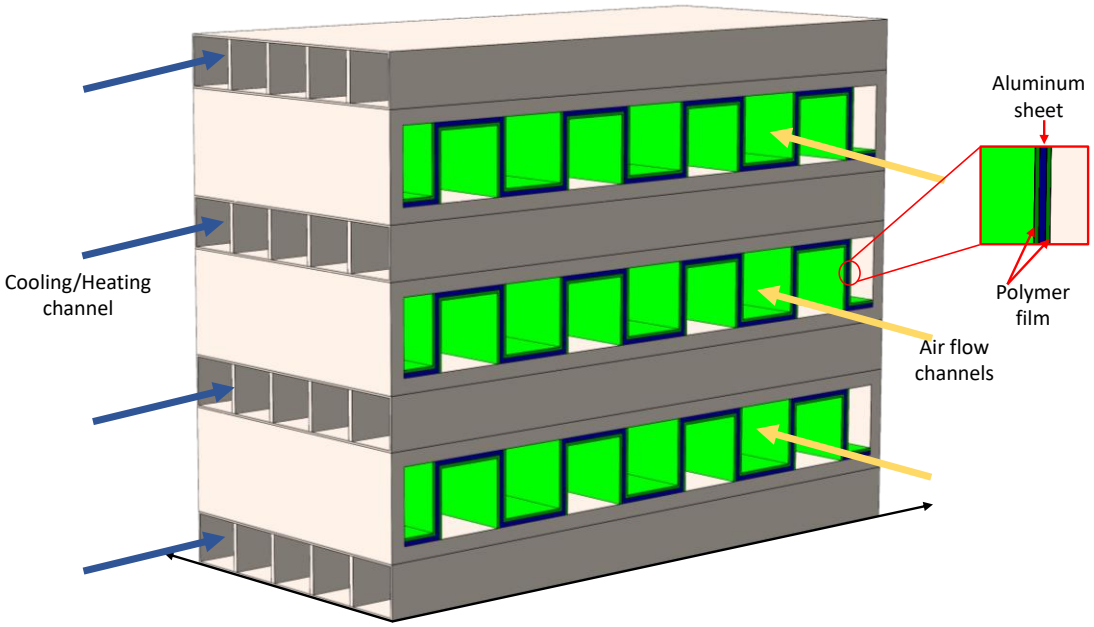

Figure 4-2: A representative CAD geometry of the thermoresponsive dehumidifier

4.2. Modelling a Unit Cell in COMSOL

We have modelled the moisture absorption/regeneration process from air to on a unit cell of the geometry shown in Figure 4-3 because simulating for the entire geometry is computationally expensive. The absorption is modeled by coupling heat transfer, mass transfer, fluid flow and solid mechanics module in COMSOL. The equations used to solve the model are explained in detail in Appendix C. In this section, we have explained the initial and the boundary conditions for each of the physics.

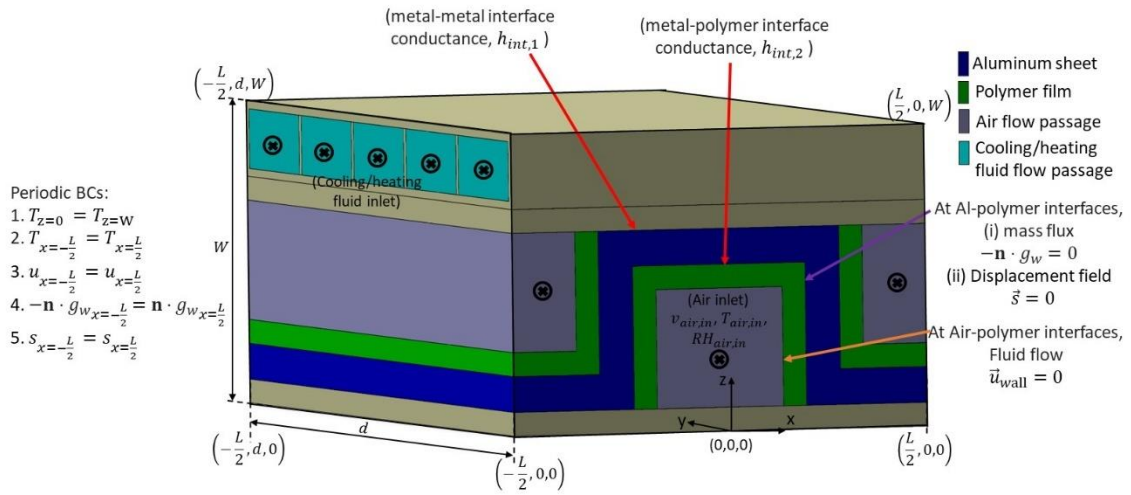

Figure 4-3: CAD geometry of the absorber unit cell used for FEA analysis in COMSOL.

4.2.1. Heat Transfer

The unit cells consist of four types of materials- (i) Solid which consists of outer casing which is assumed to be made of the stainless steel and aluminum sheet on which the polymer film is grown. (ii) Porous material consists of only polymer film and (iii) moist air that flows through the air gap, (iv) cooling/heating water flows through the cooling/heating channels. The assumptions and the boundary conditions are as follows:

1. Initial and inlet conditions are as follows:

    a. Initial temperature dehumidifier is assumed to be at regeneration temperature (T_{regen}= 60 °C), for absorption process and absorption temperature for regeneration process (T_{abs} = 35 °C).

    b. Inlet temperature of air, $T_{air,in}$ = 35 °C

c. Inlet temperature of cooling fluid, $T_{cf,in}$ = 35 ℃ and inlet temperature of heating fluid, $T_{hf,in}$ = 60 ℃

2. In the unit cell, periodic boundary conditions are applied as shown in Equation (4-1). In the equation, L/2 is the half-length of the unit cell. The periodic boundary conditions are applied as shown in the following two equations. The first equation is periodic in x-direction which stems from the assumption that there are many cells in the x-direction and the and our unit cell is unaffected by the boundary effects.

$$T_{x=-L/2} = T_{x=L/2} \tag{4-1}$$

$$T_{Z=0} = T_{Z=W} \tag{4-2}$$

The 2nd equation describes the periodic nature of the cells in z-direction which stems from the assumption that unit cell lies in the middle and the therefore are many cells on the either side of the chosen unit cell.

3. The interface between the steel casing the aluminum sheet is modelled by setting layer conductance to $h_{cont,metal}$ =1000 W/m^2-K which is typical value for two metal contact that are machined well. Similarly for aluminum sheet and the polymer interface a typical value for layer conductance between a metal and polymer was used and the set to 70 W/m^2-K.

4.2.2. Mass Transfer

The mass transfer of the moisture within the polymer is described by the following assumptions:

1. Initial boundary conditions:

    a. Air initial relative humidity of air, $RH_{air,ini}$= 0.75

    b. Air inlet relative humidity, $RH_{air,in}$= 0.75

2. Mass flux (g_w) at the aluminum-polymer interface is assumed to be zero which means that water cannot penetrate through the aluminum sheet. The mass flux is given by the following equation. In the equation $\boldsymbol{n}$ is the normal vector to the surface and g_w is the mass flux of water.

$$-\boldsymbol{n} \cdot g_w = 0 \tag{4-3}$$

3. Periodic mass flux boundary conditions are applied on the left half of the unit cell and the right half of the unit cell. This is described by the following equation.

$$-\mathbf{n} \cdot g_{w_{x=-\frac{L}{2}}} = \mathbf{n} \cdot g_{w_{x=\frac{L}{2}}} \tag{4-4}$$

4.2.3. Fluid Flow

The air flow within flow channels is given by the following the assumptions:

1. At the inlet, normal velocity is applied, $u_{x,y,z=0} = 1\ m/s$

2. At walls, no slip boundary conditions is applied, u_{wall} = 0.

3. Periodic boundary conditions is applied for velocity at the left half and right half the unit cell assuming that our unit cell is surrounded by numerous cells in the x- direction and is unaffected by edge effects. It is described by the following equation.

$$u_{x=-\frac{L}{2},y,z} = u_{x=\frac{L}{2},y,z} \tag{4-5}$$

4.2.4. Solid Mechanics

In the solid mechanics module, the deformation of the polymer is described by the following assumptions:

1. The area of the polymer film in contact with aluminum sheet is fixed and undergoes no deformation. The deformation field is described by $\vec{s}_{wall} = 0$.

2. Only the surface exposed to air is free to deform.

3. The periodic deformation boundary conditions applied are as follows.

$$\vec{s}_{x=-\frac{L}{2},y,z} = \vec{s}_{x=\frac{L}{2},y,z} \tag{4-6}$$

4.2.5. Performance Parameters

To assess the performance of the polymer, we have used moisture removal efficient (MRE) as the performance parameter. It is commonly used in literature to determine the efficiency of the thermoresponsive desiccants and is defined as follows in Equation (4-7). It is often expressed in kg/kWh.

$$MRE = \frac{m_{abs,tot}}{Q_{reg,tot}} \tag{4-7}$$

In the above equation, $m_{abs,tot}$ denotes the amount of water absorbed by the polymer during the absorption cycle. Referring to Equation (4-8), $\dot{m}_{air}$ represents the air mass flow rate, while ω_{in} and ω_{out} indicate the inlet and exit humidity ratios, respectively. τ_{abs} specifies the duration of the absorption, often referred to as the absorption period.

$$m_{abs,tot} = \int_0^{\tau_{abs}} \dot{m}_{air}(\omega_{in} - \omega_{out})\, dt \tag{4-8}$$

$Q_{reg,tot}$ represents the total regeneration heat needed to desorb the absorbed liquid during the desorption period, denoted as τ_{des}. In Equation (4-9), $\dot{m}_f$ stands for the mass flow rate of the heating liquid, while $T_{f,in}$ and $T_{f,out}$ refer to the inlet and outlet temperatures of the heating fluid, respectively.

$$Q_{reg,tot} = \int_0^{\tau_{des}} \dot{m}_f c_{p,f}\left(T_{f,in} - T_{f,out}\right) dt \tag{4-9}$$

4.2.6. Model Input Parameters

The inlet parameters are detailed in the subsequent tables. Table 4-1 displays the supply parameters. The default inlet relative humidity is set at 75% at 35 ℃, with the desired house condition being 25 ℃ and 50% RH. In this dehumidification system, isothermal absorption is presumed at the incoming air temperature. Sensible heat removal that is required to cool

the air to desired house temperature is not addressed in this model. The system design is rooted in addressing a practical challenge. An average-sized 2000 ft^2 house in the United States serves as the reference space for cooling. For clarity, the indoor comfort zone for temperature and relative humidity is set at 25 ℃ and 50% RH, in line with ASHRAE Standard 55[82]. While the outdoor air temperature can fluctuate, it's typically set at 35 ℃ and 75% RH by default. Simulations are conducted on a single unit cell, with results then scaled to multiple unit cells to meet house requirements.

ASHRAE recommends air changes per hour (ACH) is between 0.3-0.4 for residential households. We have chosen 0.35 ACH for our consideration. This means that the air in the house needs to be completely replaced by fresh air every three hours. This translates to an air flow rate of 100 cubic feet per minute (CFM). We have simplified the air flow rate to per unit cell. This air flow rate for 1 unit cell is given by Equation (4-10).

$$v_{air} = \frac{CFM}{A_{duct}} \tag{4-10}$$

Where v_{air} is the speed through the air conditioning ducts which is controlled by the blower fan, A_{duct}- is the duct area. A typical HVAC can have a rectangular duct size between 0.2-1 m which gives use the range of for air velocity to be between 0.05-1.2 m/s. The inlet air velocity is varied in the absorption simulation to obtain the desired humidity ratio for exit air.

Table 4-1: Supply air parameters for three positions in an Air conditioning system

	Temperature (℃)	Relative humidity (%)	Humidity ratio, ω (g/kg)
Dehumidifier inlet (Ambient)	35 ℃	75	27
Dehumidifier exit	35 ℃	28.5	10
House conditions	25 ℃	50	10

Table 4-2: Default input parameters used in the model.

Inlet air velocity, v_{air} (m/s)	1
Thermal conductivity of dry air (W/m-K)	0.025
Metal-metal thermal conductance (W/m^2-K)	1000
Metal-polymer thermal conductance[83] (W/m^2-K)	75
LCST temperature, T_{LCST} (℃)	50
Interaction parameter change, $\Delta\chi$	-0.5
Water diffusion coefficient in the polymer[79], D_{eff} (m^2/s)	2 x 10^{-11}
Geometric parameters	
Thickness of Aluminum tape, t_{Al} (μm)	150
Thickness of the polymer film, t_{pol} (μm)	100
Air gap width of the unit cell (μm)	750
Air gap height of the unit cell (μm)	750
Depth of dehumidifier channel, D_{ch} (cm)	10

4.3. Results and Discussions

4.3.1. Results for a Default Case

4.3.1.1. Absorption-Desorption Cycle

Given the transient nature of the problem, where the polymer undergoes an absorption-desorption cycle, the cycle time, τ, becomes pivotal. This time represents the duration the polymer absorbs moisture before transitioning to regeneration mode. The envisioned setup involves two absorber sets operating concurrently: one focused on moisture absorption and

the other on regeneration. Figure 4-4 illustrates the absorption-desorption cycle for the polymer. The absorption and desorption periods are labeled as τ_{abs} and τ_{des}, respectively. These periods might differ. Typically, they are adjusted, and performance metrics are derived for various τ_{abs} and τ_{des} values. The polymer's transition between these states plays a decisive role in the performance of the thermoresponsive polymer.

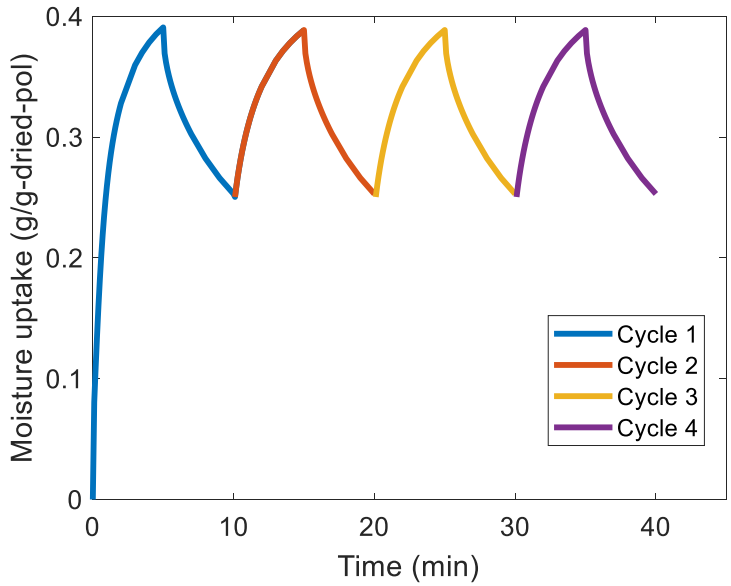

Figure 4-4: Absorption-desorption cycle of a typical LCST type polymer

In contrast, thermal equilibrium is achieved much more rapidly, as evident in Figure 4-5. When compared to moisture equilibrium, it's almost instantaneous. By default, the absorption temperature is set 15 ℃ below the LCST temperature, while the regeneration temperature is set 10 ℃ above the LCST temperature. Hence, for an LCST of 50 ℃, the temperature oscillates between 35 ℃ and 60 ℃. It's important to highlight that the cooling

fluid temperature stands at 35 ℃ and the heating fluid temperature at 60 ℃, causing the polymer temperature to be slightly higher and lower, respectively.

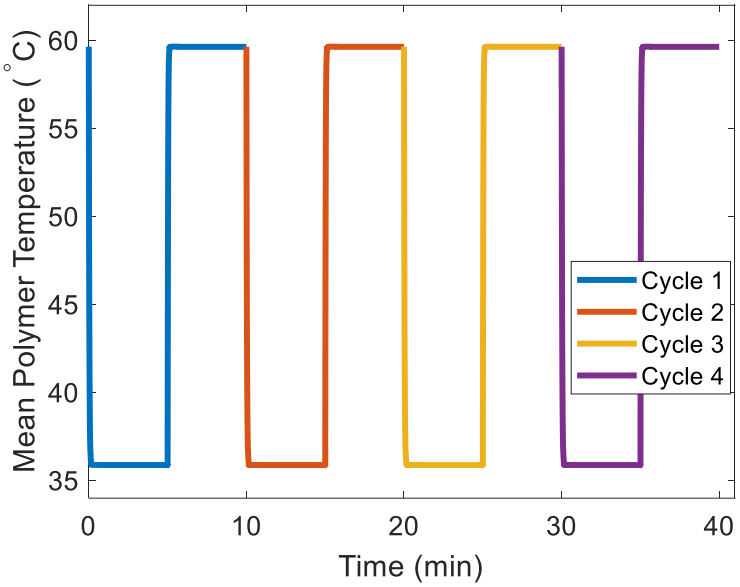

Figure 4-5: Temperature cycle during absorption-desorption cycle

Exploring various factors during the absorption-desorption cycle offers valuable insights. Figure 4-6 displays contour plots of the polymer's cross-section during this cycle, with deformation represented by the color bar. The polymer undergoes a 5-minute swelling process, followed by a 5-minute desorption, returning to its initial state before the cycle recommences. It's important to highlight that the starting point isn't a completely dry polymer; the depiction focuses on the repeated absorption-desorption cycle. This polymer swells at 35 ℃ and contracts at 60 ℃, consistent with its LCST of 50 ℃. The deformation shown aligns with the moisture uptake detailed in Figure 4-4.

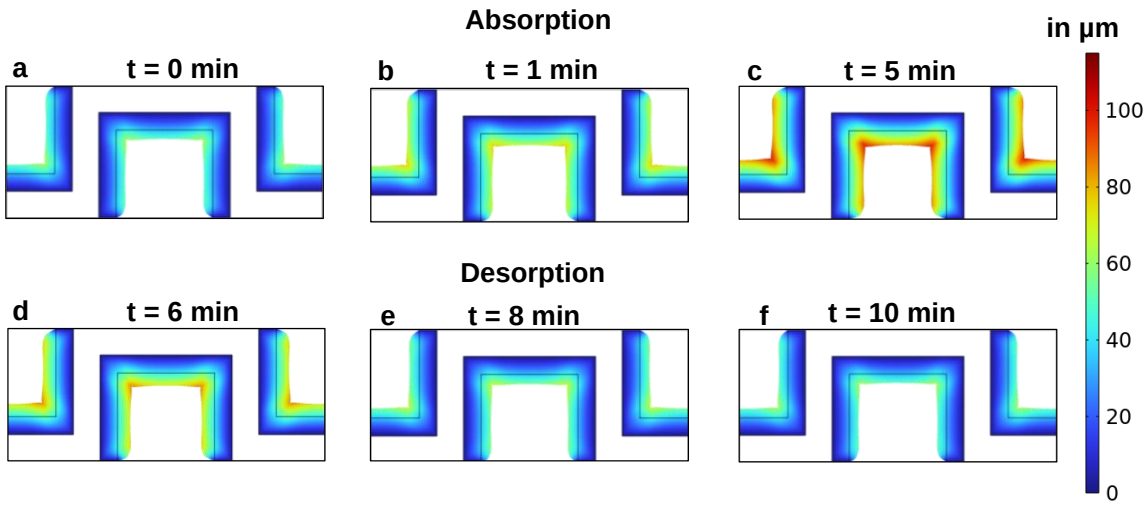

Figure 4-6: Contour plots of swelling/shrinking in an absorption-desorption cycle

4.3.1.2. Air Pressure Drop in the Dehumidifier.

Analyzing the air pressure drop within the dehumidifier channel is crucial. As depicted in Figure 4-7(a), the air pressure drop across the channel exhibits a linear trend. For the shorter lengths (depths) of the dehumidifier considered in this model, the pressure drop remains relatively minimal. Specifically, a drop of less than 180 Pa is noted for a channel depth of 10 cm at an air velocity of 1 m/s. This drop is even more modest at reduced air velocities. Given the limited channel depth, the air pressure drop doesn't pose significant challenges for this design. This observation is reinforced by Figure 4-7(b), which plots the pressure drop against different channel depths. The pressure drop stays within acceptable limits, and when compared with an atmospheric pressure of 1 atm, a drop of less than 200 Pa is negligible.

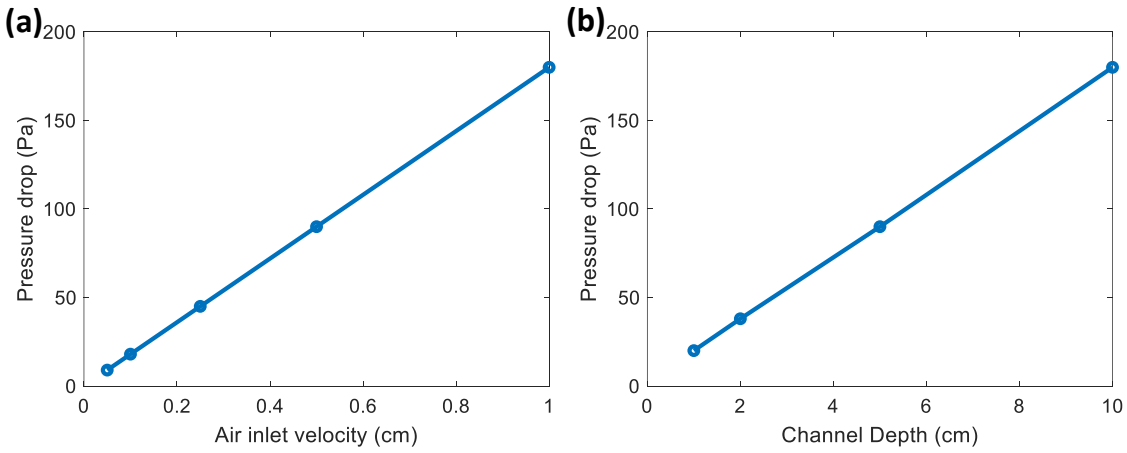

Figure 4-7: (a) Air Pressure drop in a dehumidifier with 10 cm depth for different air inlet velocity, (b) Air pressure drop for different length (depths) of the dehumidifier for air inlet velocity of 1 m/s.

4.3.1.3. Exit Air Humidity Ratio

A critical parameter to consider is the exit humidity ratio of air supplied to the residence. Ensuring the air meets the home's humidity ratio requirements is essential. For isothermal absorption at 35 °C, the target is to supply air with an average humidity ratio of 10 g/kg of dry air. The two determinants influencing this humidity ratio are the air inlet velocity and absorption depth.

Figure 4-8(a) illustrates the air exit humidity ratio over time. Initially, the humidity ratio drops rapidly as the polymer swiftly absorbs water from the air. However, as absorption progresses, the polymer nears saturation, causing the outgoing air to maintain a humidity ratio similar to the incoming air. It's evident that a slower air inlet velocity prolongs the time to reach saturation since the air interacts longer with the polymeric film,

resulting in more water being absorbed per unit mass of air at reduced velocities.

Figure 4-8(b) contrasts the average humidity ratio with the absorption period at varying air inlet velocities. The average exit humidity ratio is a more relevant metric when determining the absorption period, given the goal of maintaining a specific household humidity level before initiating polymer desorption. While lower air velocities can sustain the desired humidity for extended periods, they might fall short in meeting the house's Air Changes per Hour (ACH) needs. Hence, 1 m/s is selected as the standard air inlet velocity for subsequent calculations.

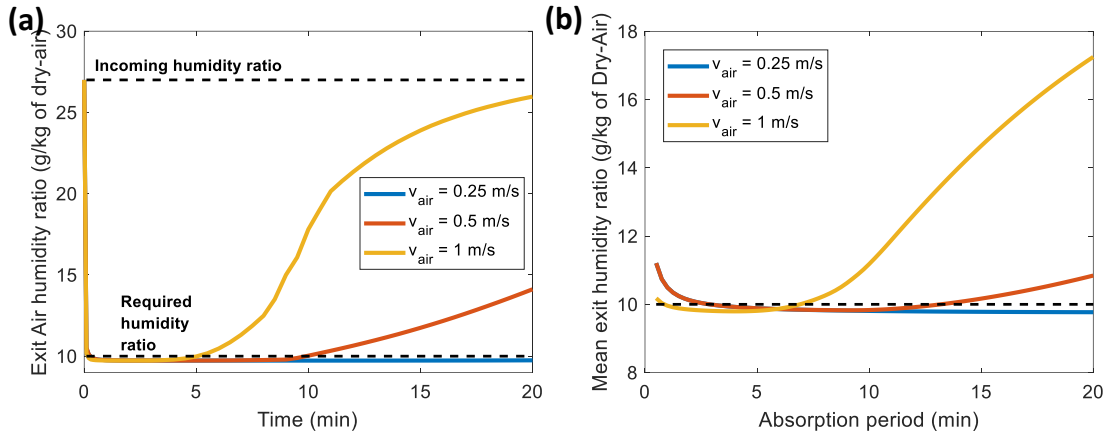

Figure 4-8: (a) Exit humidity ratio of air with time and (b) mean exit humidity ratio with absorption period at different inlet air velocities.

Figure 4-9 depicts the exit air humidity ratio across various dehumidifier channel depths. For shallower channel depths, such as 1 cm and 2 cm, the targeted humidity ratio of 10 g/kg of dry air is achieved for a brief span, less than half a minute. This short duration results from the limited interaction time between the air and the polymer. The polymer

quickly reaches saturation, hindering further water absorption from the incoming air. Consequently, such minimal depth proves to be inefficient.

For a channel depth of 5 cm, the desired humidity ratio is sustained for a mere absorption period of under 2 minutes, as illustrated by the yellow curve in Figure 4-9(b). However, with a 10 cm channel depth, the system can consistently deliver the desired humidity ratio for approximately 7 minutes before observing an uptick in the average humidity ratio.

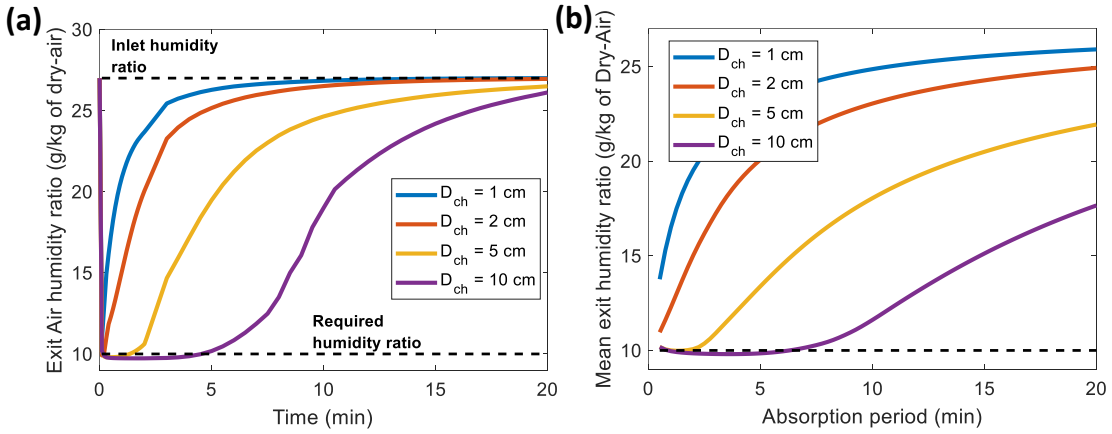

Figure 4-9: (a) Exit humidity ratio of air with time and (b) mean exit humidity ratio with absorption period at different channel depths

It's important to acknowledge that several factors, such as channel width, polymer film thickness, and absorption interaction parameter, could potentially impact the exit humidity ratio and pressure drop. However, in the context of absorption, this analysis utilizes the default values for these properties as provided in Table 4-2.

4.3.1.4. Moisture Removal Efficiency

The most important metric in assessing the dehumidification system's efficacy is the moisture removal efficiency (MRE). After the absorption phase concludes, the polymer undergoes regeneration, wherein water is removed in its liquid form by heating the polymer film's substrate internally using a heating fluid. For desorption, the polymer film's 90% saturation serves as the starting point. Figure 4-10 illustrates the MRE for varying desorption periods, τ_{des}.. It's evident that the MRE diminishes as the desorption period, τ_{des}., extends. This trend can be attributed to the diminishing rate of moisture removal as more moisture is extracted. Consequently, the additional heat introduced becomes less effective in extracting further water from the polymer.

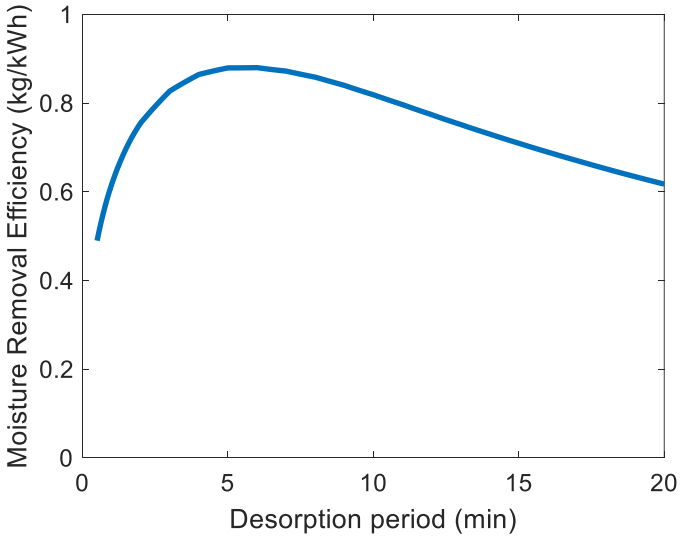

Figure 4-10: Moisture removal efficiency for different desorption period for TRP with LCST 50 ℃ and $\Delta\chi$ = -0.5 and RH_{air} =75%

4.3.2. Effect of Polymer Film Thickness on Moisture Removal Efficiency

Figure 4-11 displays the moisture removal efficiency (MRE) of the polymer, highlighting the peak MRE achieved at different desorption periods based on the film's thickness. Understandably, a 50 μm polymer film reaches saturation rapidly during water absorption. Similarly, it releases water at a faster rate during desorption. However, after a certain point, additional heat contributes less to water removal, leading to a decline in MRE. Conversely, a film that's too thin might necessitate frequent switches between absorption and desorption, which may not be feasible in practical applications. On the other hand, a 250 μm film takes a prolonged duration to reach saturation. As a result, its peak isn't evident since it requires an extended period for water desorption, which in turn increases the total heat input, subsequently reducing the MRE. Hence, a polymer film thickness of 100 μm is chosen as the default. This thickness offers a balanced desorption time and delivers a good MRE.

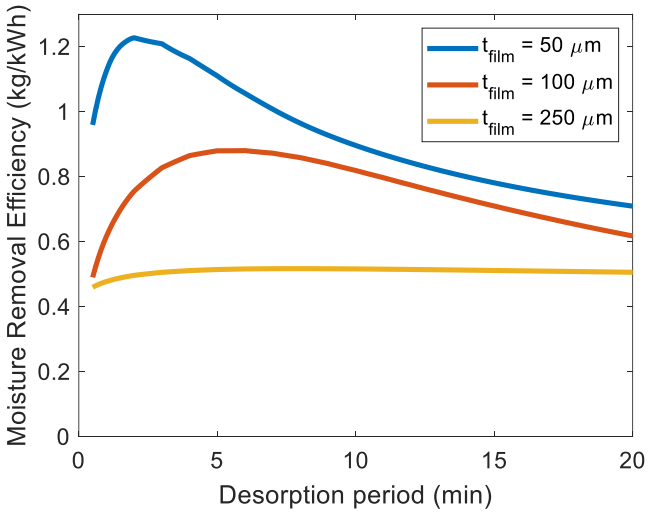

Figure 4-11: Moisture removal efficiency vs absorption-desorption period for different thicknesses of the polymeric film for LCST = 50 ℃, $\Delta\chi$= -0.5 and RH_{air} =75%

4.3.3. Effect of LCST Temperature on Moisture Removal Efficiency

Figure 4-12 indicates that a lower LCST temperature yields a superior MRE. However, this comes with the challenge of maintaining the polymer at a temperature significantly below the ambient, which is logistically challenging. As such, an LCST of 32 ℃ isn't optimal. A polymer with an LCST around 50 ℃ is more practical, as it can be stored at ambient temperature and cooled using a fluid also at ambient temperature. This observation aligns with conclusions drawn in the previous chapter: an LCST around 50 ℃ might offer slightly reduced performance compared to TRPs with a lower LCST, but it negates the need for refrigerating the cooling fluid used during the absorption phase.

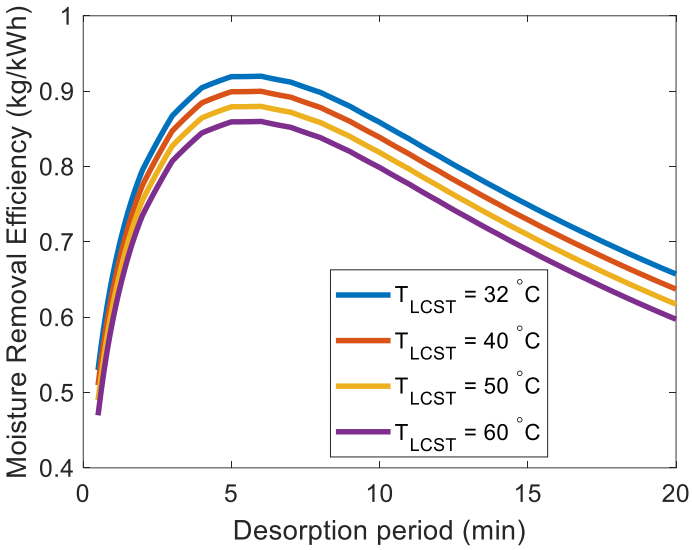

Figure 4-12: Moisture removal efficiency vs desorption period different values of LCST temperatures and $\Delta\chi$= -0.5 and RH_{air} =75%

4.3.4. Effect of Interaction Parameter on Moisture Removal Efficiency

Figure 4-13(a) demonstrates that as the interaction parameter ($\Delta\chi$) decreases, there's a corresponding increase in the moisture removal efficiency during desorption. Given that $\Delta\chi$, plays a pivotal role in determining a polymer's absorption capacity, it's anticipated that a polymer with a lower $\Delta\chi$ would exhibit enhanced efficiency. Specifically, a polymer with $\Delta\chi$= -0.5 can achieve a peak MRE nearly three times that of $\Delta\chi$ = 0 (equivalent to the NIPAAm polymer in the absorption region). These TRPs have an LCST temperature of 50 °C. This suggests that a polymer with a higher absorption capacity and constant LCST temperature is more suitable to be used as a desiccant in air conditioning.

The non-linear surge in MRE with a declining $\Delta\chi$ can be linked to the increase in

absorption capacity that accompanies a decrease in $\Delta\chi$. A smaller χ value is always preferable for enhanced water absorption. It's worth noting that while it might have been possible to opt for an even smaller $\Delta\chi$ to boost absorption capacity and, by extension, MRE, a conservative approach was adopted. The default choice halted at $\Delta\chi = -0.5$, corresponding to a polymer with an absorption capacity roughly 1.5 times that of PNIPAAm. This choice is somewhat conservative since there already exist polymers that have greater absorption capacity than 1 $g_{H2O}/g_{dry\text{-}pol}$ at 75% relative humidity but they tend be Interpenetrating network (IPN) polymer composed of LCST NIPAAm monomer and a hygroscopic monomer and have an LCST of 32 ℃. And generally, an increase in the LCST temperature from 32 ℃ to 50 ℃ would also compromise its absorption capacity hence the default choice of the thermoresponsive polymer is one with LCST=50 ℃ and $\Delta\chi = -0.5$.

Although I have chosen $\Delta\chi = -0.5$ and LCST 50 ℃ as the default TRP for this work it is still worth looking at performance of thermoresponsive polymer with LCST 50 ℃ and absorption capacity of 1, 1.5 and 2 $g_{H2O}/g_{dry\text{-}pol}$ at RH_{air} = 75% and T_{air} = 35 ℃. Interaction parameter change ($\Delta\chi$), corresponding to these TRPs are -1.5, -2.3 and -3.2 respectively. The moisture removal efficiency (MRE) of the system for these TRPs as desiccants is shown in Figure 4-13(b) along with TRPs shown in Figure 4-13(a). It can be seen that more absorbent thermoresponsive polymers show a significant increase in MRE. For

thermoresponsive polymers with absorption capacity of 1, 1.5 and 2 $g_{H2O}/g_{dry\text{-}pol}$ at RH_{air} = 75% and T_{air} = 35 °C, the peak MRE increased to 1.75, 2.75 and 3.6 respectively. These values are greater than shown for similar studies using thermoresponsive polymer that show peak MRE up to 1.1 [30] or lower at varying input parameters like LCST temperature, dew point of exit air, regeneration temperature etc. These peak MREs correspond to peak COPs of 1.1, 1.7 and 2.3 respectively. These values are comparatively higher than existing desiccant dehumidification systems utilizing liquid[14,47,84–87] or solid desiccants[88–91] (not necessarily thermoresponsive desiccants). For most such existing systems the COP is below 1.

It must be noted here that while manipulating χ, it was only changed in the absorption region and left unchanged in the desorption region. This made the new TRPs more thermoresponsive and hence caused a greater increase on MRE than we would see in a real polymer. In real-world conditions, an increase in the absorption capacity of a polymer is expected to occur across the entire temperature range, which would result in a less marked increase in MRE.

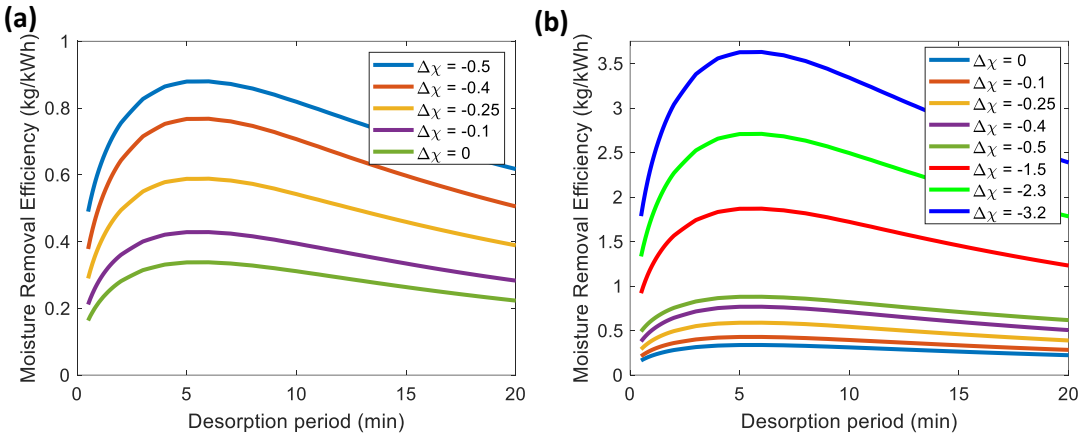

Figure 4-13: Moisture removal efficiency vs desorption period at different interaction parameters, Δχ and LCST = 50 °C, (a) smaller range for Δχ, (b) bigger range for Δχ

4.3.5. Effect of Air Relative Humidity on Moisture Removal Efficiency

Figure 4-14 illustrates that air relative humidity positively influences the moisture removal efficiency (MRE). This correlation stems from the moisture absorption capacity of a polymer. As the polymer can absorb more moisture at higher relative humidities per unit mass of the dried polymer, it increases the numerator in the MRE equation, thereby enhancing the efficiency. However, this also implies that during the desorption phase, there's more water to remove, necessitating a higher energy input. Yet, this water removal occurs in liquid form, primarily through the diffusion of liquid water out of the polymer, facilitated by the polymer's shrinking and the inherent phase change. Importantly, this regeneration energy doesn't rise proportionally with the increase in absorbed moisture, especially when compared to conventional regeneration methods where water undergoes

vaporization.

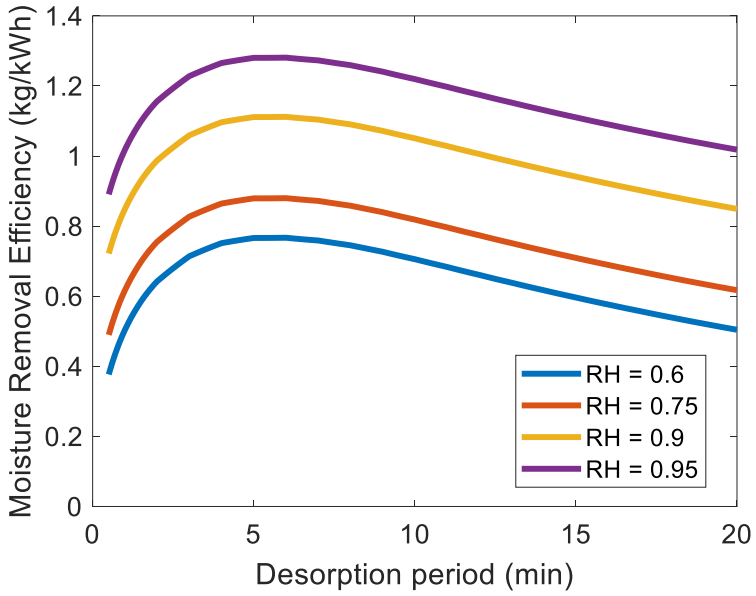

Figure 4-14: Moisture removal efficiency vs desorption period for different relative humidity of ambient air

4.4. Summary

In this chapter, the functionality of an innovative thermoresponsive dehumidifier was showcased. This dehumidifier, similar to a car radiator, toggles between absorption and regeneration cycles by adjusting the temperature of the heating/cooling fluid. The model features fins constructed from a thin aluminum sheet, deposited with a layer of thermoresponsive polymer. As humid air traverses these thermoresponsive fins, it loses its moisture content. Upon completing the absorption phase, a transition to the heating fluid elevates the temperature of the thermoresponsive fins, facilitating the removal of liquid water.

To achieve the target humidity ratio for indoor air, parameters such as air inlet velocity and dehumidifier depth were adjusted. The optimal conditions were identified as an air velocity of 1 m/s and a dehumidifier depth of 10 cm, aligning with the practical needs of a household. This dehumidifier configuration yielded a moisture removal efficiency (MRE) comparable to prior research on thermoresponsive polymers under similar air conditions. However, it's essential to highlight that a direct comparison could not be made because there haven't been earlier studies that utilize thermoresponsive polymer to absorb moisture and regenerate it by removing water in liquid form.

Further exploration into the effects of parameters such as LCST temperature, polymer-water interaction parameter, polymer film thickness, and air relative humidity on the dehumidifier's MRE was conducted. The findings suggest optimal performance under conditions of higher relative humidities, lower LCST temperatures, and interaction parameters. While a lower LCST temperature offers superior performance, the marginal decline of 4% in peak MRE from 32 ℃ to 50 ℃ is observed. A polymer with an LCST of 50 ℃ is favored, as it allows for cooling of the polymer with ambient temperature water, eliminating the need for refrigeration of cooling water during the absorption phase. When interaction parameter was varied, a lower interaction parameter produced a higher MRE with peak MRE being as high as 3.6 for TRP with LCST = 50 ℃ and $\Delta\chi$ = -3.2 with absorption capacity of 2 $g_{H2O}/g_{dry\text{-}pol}$ at RH_{air} = 75% and T_{air} = 35 ℃. These MRE values

when compared to other dehumidification studies using LCST polymers, are much higher as they show a maximum MRE of 1.1[30] or lower for various inlet conditions like outlet air dew point (akin to exit humidity), regeneration temperature, LCST temperature etc. An MRE of 3.6 when compared to the most commonly known parameter COP, turns out to be 2.26 which is reasonably good value when compare with other dehumidification systems.

However, a conservative choice was made for default TRP as such a polymer with LCST = 50 ℃ does not yet exist and therefore TRP with LCST = 50 ℃ and $\Delta\chi$ = -0.5 was chosen the default. Consequently, efforts were made to synthesize copolymers approximating these specifications. The subsequent chapter delves into the synthesis of polymers with higher LCSTs than 32 ℃ and superior absorption capacities compared to PNIPAAm.

5. CONCLUSION AND FUTURE DIRECTIONS

5.1. Dissertation Summary

This dissertation provides a novel investigation into the use of thermoresponsive materials as efficient dehumidifiers in air conditioning systems. It examines both liquid and solid desiccants, with a particular focus on the regeneration process, proposing an innovative method of releasing absorbed water in liquid form, which is more energy-efficient compared to the traditional vapor-based regeneration methods.

Chapter 2 introduces thermoresponsive ionic liquid desiccants, highlighting their potential in improving the coefficient of performance (COP) by utilizing liquid-liquid phase transitions during the dehumidification process. The analysis employs the Flory-Huggins theory to suggest that flatter immiscibility curves at lower temperatures correlate with higher COP. The chapter identifies the challenges in creating liquid desiccants that can achieve low Lower Critical Solution Temperature (LCST) temperatures with negative enthalpic interaction parameters, advocating for experimental validation of the proposed thermoresponsive LCST cycles.

Chapter 3 shifts the focus to the modeling of water vapor absorption on thermoresponsive polymeric thin films using the Vrentas-Vrentas model. This model, which includes the elastic Gibbs free energy, provides a better fit for the polymers' behavior

especially in their glassy state. The chapter establishes a baseline for the absorption capacity of various hypothetical thermoresponsive polymers based on the poly(N-isopropylacrylamide) or PNIPAAm. By exploring optimal parameters like LCST temperature, interaction parameter, and polymer film thickness, this analytical work lays the groundwork for the design and simulation of a dehumidifier using a thermoresponsive polymer film.

Chapter 4 progresses into the practical application by conducting a finite element analysis of the dehumidifier design. This innovative device operates akin to a car radiator and alternates between absorption and regeneration cycles through temperature modulation. A key feature of the dehumidifier is its construction, with fins composed of thin aluminum sheets coated with a thermoresponsive polymer, which absorbs moisture from the air. This chapter outlines the optimal operational parameters for moisture removal efficiency (MRE), taking into account air inlet velocity and dehumidifier depth, achieving a significant MRE under simulated conditions. The results also underscore the importance of relative humidity, LCST temperature, and the interaction parameters in maximizing the dehumidifier's efficiency.

Finally, the dissertation encapsulates the journey from theoretical analysis to practical design and concludes with a forward-looking perspective. It highlights the initial steps taken towards synthesizing copolymers with higher LCST temperatures and greater

absorption capacities than PNIPAAm, setting the stage for future research and development. The synthesized materials are expected to closely match the optimal parameters derived from the computational models, providing a promising avenue for achieving more energy-efficient and effective dehumidification in air conditioning systems.

The collective findings of this research point toward the feasibility of using thermoresponsive materials in dehumidification applications, offering an avenue for enhanced performance and energy efficiency. Future work, as suggested, includes experimental validation of the proposed systems, synthesis of polymers with tailored properties to match the theoretical models, and further refinement of the finite element simulations to perfect the dehumidifier design.

5.2. Future Directions

Earlier chapters highlighted that an LCST of 32 ℃ doesn't align well with optimal air conditioning performance. Given that ambient air temperatures frequently exceed this value, cooling becomes essential to keep the polymer below its LCST for effective water vapor absorption. This underscores the importance of creating polymers with elevated LCSTs.

The thermoresponsive nature of PNIPAAm, characterized by an LCST of 32 ℃, is well-recognized. Matsumoto et al.[38] crafted an interpenetrating polymer network (IPN) gel

by merging thermoresponsive poly(N-isopropylacrylamide) and hydrophilic sodium alginate. When dried, this IPN gel exhibits notable moisture absorption below its LCST and releases it as liquid water above this temperature. The gel's composition includes PNIPAAm (thermoresponsive) and Alg (hygroscopic). While the IPN synthesis bolsters the gel's absorption capacity, it doesn't raise the LCST, which remains anchored at 32 ℃. This confines its moisture absorption capabilities to temperatures below this mark.

The aim is to adjust the LCST of thermoresponsive polymers by integrating hygroscopic polymers. Matsumoto et al.[38] paired PNIPAAm with AAcNa in diverse concentrations. Figure 5-1 showcases the normalized water content for PNIPAAm, PNIPAAm-co-AAcNa copolymer and PNIPAAm/Alg IPN across a temperature spectrum. The PNIPAA/Alg IPN doesn't influence PNIPAAm's LCST. Conversely, adding AAcNa nudges NIPAAm's LCST from 32℃ to 42℃ at a concentration of 2.5 mol%. Exceeding this concentration sees AAcNa's hygroscopic attributes dominate the copolymer, undermining its thermoresponsive traits. This chapter focuses on the synthesis of innovative copolymers, assessing their absorption capacity and LCST via swelling tests in water.

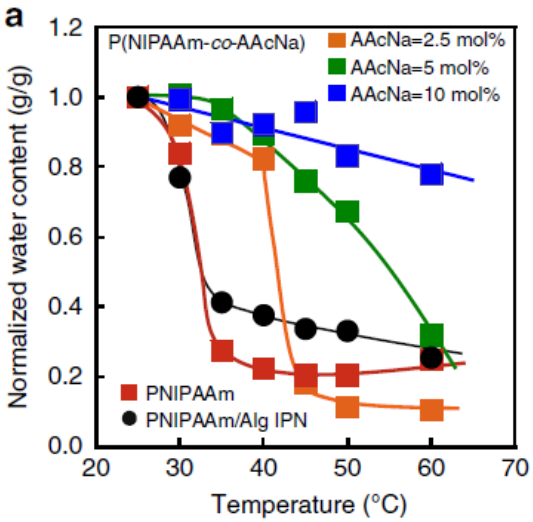

Figure 5-1: Normalized water content for different copolymers with varying temperature (Reprinted with permission from Ref[38], open access under Creative Commons CC)

5.2.1. Synthesis of New Thermoresponsive Polymers (TRPs)

The PNIPAAm/Alg gel was synthesized following the methodology of Matsumoto et al.[38], yielding results in line with the findings of the original authors. Figure 5-2 displays the normalized water content, defined as W/W_0, where W denotes the hydrogel's weight at each temperature and W_0 represents the water weight at 25℃. The figure contrasts the normalized water content of three hydrogels: PNIPAAm, Alg, and the PNIPAAm/Alg IPN hydrogel. The IPN gel's behavior mirrors that of the PNIPAAm gel, with the LCST temperature remaining unchanged. This observation underscores the need to investigate alternative hygroscopic polymers capable of adjusting the LCST temperature.

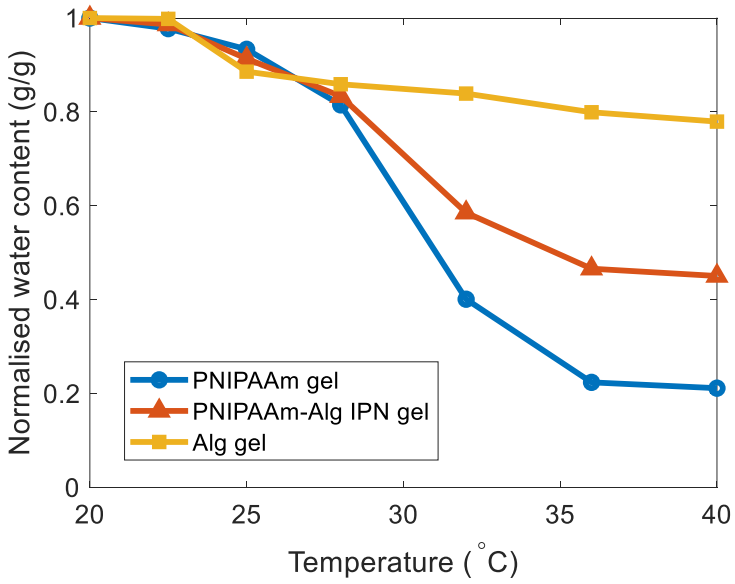

Figure 5-2: Normalized water content for hydrogels at different temperatures.

Following the successful replication of results from Matsumoto et al.[38], the focus shifted to the synthesis of new copolymers. This decision was influenced by the noticeable LCST shift with PNIPAAm-co-AAcNa, a change absent in the PNIPAAm/Alg gel. Furthermore, copolymers present the advantage of adjustable properties through the manipulation of monomer concentrations. They also cater to the demands of large-scale production, especially for roll-to-roll manufacturing of polymeric films on aluminum substrates. Hence two new copolymers were using NIPAAm monomer as the LCST component and a new hygroscopic monomer as the hygroscopic component to enhance the absorption capacity of the synthesized copolymers.

The two copolymers that were synthesized include a linear copolymer with Dimethylaminoethyl acrylate (DMAEMA) as the secondary more hygroscopic monomer

and a crosslinked copolymer with ([2-(Methacryloyloxy)ethyl]dimethyl-(3-sulfopropyl)ammonium hydroxide) (SBMA) as hygroscopic monomer.

Figure 5-3(a) illustrates the water absorption of the NIPAAm-co-DMAEMA linear copolymer. The data indicates that as the DMAEMA concentration increases from 10 wt% to 25 wt%, there's a corresponding enhancement in absorption capacity. However, a further increase in concentration from 25 wt% to 50 wt% leads to a decline in both absorption capacity and the LCST characteristic. This decline can be attributed to the synthesis of a linear copolymer without the crosslinker MBAA, rendering the resultant copolymer water-soluble. This solubility caused the copolymer to dissolve during the absorption test, making this test inappropriate for gauging the copolymer's LCST. While the potential of this polymer hasn't been entirely ruled out, there are reservations regarding its longevity over repeated absorption cycles due to the risk of it being washed away.

Figure 5-3(b), shows the water absorption of NIPAAm-co-SBMA copolymer exhibited improvements in both absorption capacity and LCST temperature. In particular, when the 25 wt% SBMA copolymers were compared to pure PNIPAAm, the former absorbed 1.5 times more water at 18 ℃, and its LCST increased to 42 ℃, up from the initial 32 ℃.

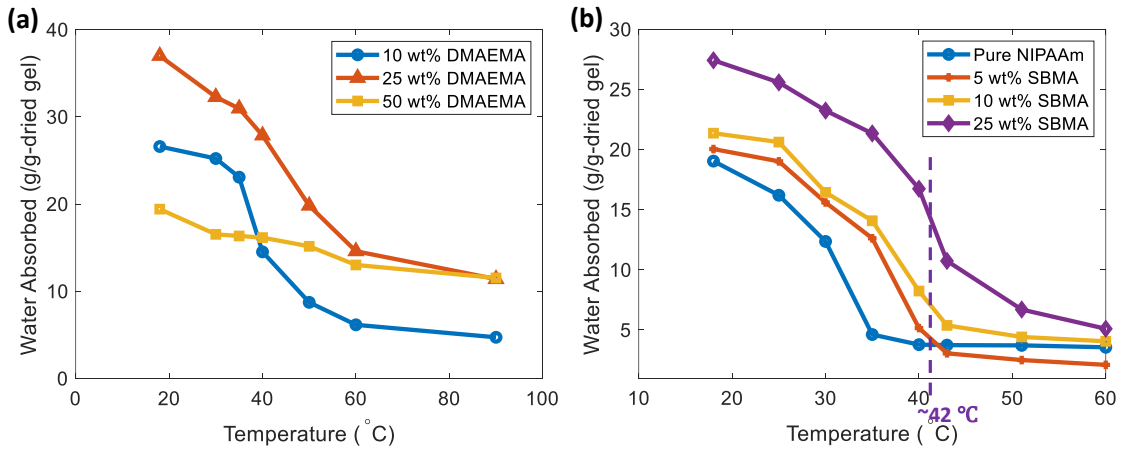

Figure 5-3: Water absorption at different temperatures for (a) NIPAAm-co-DMAEMA copolymer, and (b) NIPAAm-co-SBMA copolymer

5.2.2. Absorption Test of Thermoresponsive Polymer (TRPs) in Realistic Conditions

The prior section showcased the successful synthesis of copolymers with an LCST exceeding 32°C, the LCST for poly-(NIPAAm). Two copolymers were developed that elevated the LCST temperature to over 40°C. The first, NIPAAm-co-DMAEMA, was a linear copolymer. However, during the swelling test, it dissolved in water, making it challenging to evaluate its thermoresponsive properties on an aluminum substrate. It's essential to assess its performance in the air before confirming its applicability. The second copolymer, crosslinked using NIPAAm and SMBA as monomers, achieved an LCST shift to 42°C with 25 wt% of SBMA monomer. Notably, the absorption tests for these polymers were conducted in liquid water, not air.

Therefore, future research can be done in the area to authenticate the LCST

characteristics of the synthesized copolymers under actual conditions using a humidity chamber, as depicted in Figure 5-4. This chamber regulates humidity through various salt solutions. Instruments like an in-situ thermocouple, RH recorder, and weighing scale will track temperature, relative humidity, and copolymer mass in real-time. While efforts to stabilize humidity using different salt solutions faced challenges, particularly in sustaining humidity levels above 80% for prolonged durations, this configuration holds potential for subsequent investigations into the thermoresponsive behavior of polymers.

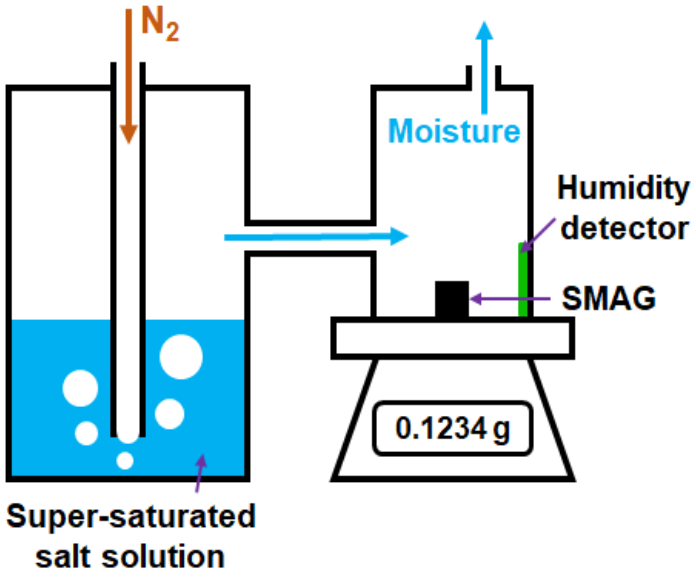

Figure 5-4: Diagram of the humidity box used for absorption/desorption investigation (Reprinted with permission from Ref[39], Copyright 2019 Advanced Materials)

REFERENCES

1. U.S. Energy Information Administration. 2015 Residential Energy Consumption Survey. https://www.eia.gov/consumption/residential/data/2015/hc/php/hc11.1.php (2018).

2. Linde Group. Refrigerants Environmental Data: Ozone Depletion and Global Warming Potential. *Refrigerants Environmental Data* 2 (2015).

3. DOE. Quadrennial Technology Review: An Assessment of Energy Technologies and Research Opportunities. (Increasing Efficiency of Building Systems and Technologies). 38 (2015).

4. Velders, G. J. M., Fahey, D. W., Daniel, J. S., McFarland, M. & Andersen, S. O. The large contribution of projected HFC emissions to future climate forcing. *Proc Natl Acad Sci U S A* **106**, 10949–10954 (2009).

5. Shelpuk, B. C. & Hooker, D. W. Development programmes in solar desiccant cooling for residential buildings. *International Journal of Refrigeration* **2**, 173–179 (1979).

6. Enteria, N. *et al.* Development and construction of the novel solar thermal desiccant cooling system incorporating hot water production. *Appl Energy* **87**, 478–486 (2010).

7. Ge, T. S., Dai, Y. J., Wang, R. Z. & Li, Y. Experimental investigation on a one-rotor two-stage rotary desiccant cooling system. *Energy* **33**, 1807–1815 (2008).

8. Panaras, G., Mathioulakis, E., Belessiotis, V. & Kyriakis, N. Theoretical and experimental investigation of the performance of a desiccant air-conditioning system. *Renew Energy* **35**, 1368–1375 (2010).

9. Al-Alili, A., Hwang, Y. & Radermacher, R. Performance of a desiccant wheel cycle utilizing new zeolite material: Experimental investigation. *Energy* **81**, 137–145 (2015).

10. Ge, T. S., Dai, Y. J., Wang, R. Z. & Peng, Z. Z. Experimental comparison and

analysis on silica gel and polymer coated fin-tube heat exchangers. *Energy* **35**, 2893–2900 (2010).

11. Weixing, Y., Yi, Z., Xiaoru, L. & Xiugan, Y. Study of a new modified cross-cooled compact solid desiccant dehumidifier. *Appl Therm Eng* **28**, 2257–2266 (2008).

12. Abdullah, S. *et al.* Technological development of evaporative cooling systems and its integration with air dehumidification processes: A review. *Energy and Buildings* vol. 283 Preprint at https://doi.org/10.1016/j.enbuild.2023.112805 (2023).

13. Peng, C. S. P. & Howell, J. R. Analysis and simulation of an efficient liquid desiccant system for warehouse dehumidification. in *ASHRAE Transactions* vol. 88 (1982).

14. Ahmed, S. Y., Gandhidasan, P. & Al-Farayedhi, A. A. Thermodynamic analysis of liquid desiccants. *Solar Energy* **62**, 11–18 (1998).

15. Gandhidasan, P. A simplified model for air dehumidification with liquid desiccant. *Solar Energy* **76**, 409–416 (2004).

16. Kalpana & Subudhi, S. Developments in liquid desiccant dehumidification system integrated with evaporative cooling technology. *International Journal of Energy Research* vol. 46 61–88 Preprint at https://doi.org/10.1002/er.6713 (2022).

17. Kumar, R., Dhar, P. L. & Jain, S. Development of new wire mesh packings for improving the performance of zero carryover spray tower. *Energy* **36**, 1362–1374 (2011).

18. Gandhidasan, P. Prediction of pressure drop in a packed bed dehumidifier operating with liquid desiccant. *Appl Therm Eng* **22**, 1117–1127 (2002).

19. Patnaik, S., Lenz, T. G. & Lof, G. O. G. Performance Studies for an Experimental Solar Open-cycle Liquid Desiccant Air Dehumidification System. *Solar Energy* **44**, 123–135 (1990).

20. Factor, H. M. & Grossman, G. A Packed Bed Dehumidifier/Regenerator for Solar Air Conditioning with Liquid Desiccants. *Solar Energy* **24**, 541–550 (1980).

21. Martin, V. & Goswami, D. Y. Heat and Mass Transfer in Packed Bed Liquid Desiccant Regenerators — An Experimental Investigation. in *Transactions of the ASME* vol. 121 162–170 (1999).

22. Ali, A., Vafai, K. & Khaled, A. R. A. Comparative study between parallel and counter flow configurations between air and falling desiccant in the presence of nanoparticle suspensions. *Int J Energy Res* **27**, 725–745 (2003).

23. Qi, R., Lu, L. & Qin, F. Model development for the wetted area of falling film liquid desiccant air-conditioning system. *Int J Heat Mass Transf* **74**, 206–209 (2014).

24. Dong, C., Lu, L. & Wen, T. Investigating dehumidification performance of solar-assisted liquid desiccant dehumidifiers considering different surface properties. *Energy* **164**, 978–994 (2018).

25. El-Dessouky, H. T., Ettouney, H. M. & Bouhamra, W. A novel air conditioning system: Membrane air drying and evaporative cooling. *Chemical Engineering Research and Design* **78**, 999–1009 (2000).

26. Goetzler, W., Zogg, R., Young, J. & Johnson, C. *Energy Savings Potential and RD&D Opportunities for Non-Vapor-Compression HVAC Technologies*. http://www.osti.gov/home/ (2014).

27. Xing, R. *et al.* Advanced thin zeolite/metal flat sheet membrane for energy efficient air dehumidification and conditioning. *Chem Eng Sci* **104**, 596–609 (2013).

28. Bui, T. D., Chen, F., Nida, A., Chua, K. J. & Ng, K. C. Experimental and modeling analysis of membrane-based air dehumidification. *Sep Purif Technol* **144**, 114–122 (2015).

29. Kocher, J. D., Yee, S. K. & Wang, R. Y. A first and second law analysis of a thermoresponsive polymer desiccant dehumidification and cooling cycle. *Energy Convers Manag* **253**, (2022).

30. Zeng, Y., Woods, J. & Cui, S. The energy saving potential of thermo-responsive desiccants for air dehumidification. *Energy Convers Manag* **244**, (2021).

31. Welton, T. Room-Temperature Ionic Liquids. Solvents for Synthesis and Catalysis. *Chem Rev* (1999) doi:10.1021/cr980032t.

32. Seddon, K. R. Ionic liquids for clean technology. *Journal of Chemical Technology and Biotechnology* **68**, 351–356 (1997).

33. Chiappe, C. & Pieraccini, D. Ionic liquids: Solvent properties and organic reactivity. *J Phys Org Chem* **18**, 275–297 (2005).

34. Kang, H. *et al.* Molecular insight into the lower critical solution temperature transition of aqueous alkyl phosphonium benzene sulfonates. *Commun Chem* **2**, (2019).

35. Zhao, Y., Wang, H., Pei, Y., Liu, Z. & Wang, J. Understanding the mechanism of LCST phase separation of mixed ionic liquids in water by MD simulations. *Physical Chemistry Chemical Physics* **18**, 23238–23245 (2016).

36. Wasserscheid, P. & Seiler, M. Leveraging gigawatt potentials by smart heat-pump technologies using ionic liquids. *ChemSusChem* **4**, 459–463 (2011).

37. Chugh, D., Gluesenkamp, K., Abdelaziz, O. & Moghaddam, S. Ionic liquid-based hybrid absorption cycle for water heating, dehumidification, and cooling. *Appl Energy* (2017) doi:10.1016/j.apenergy.2017.05.161.

38. Matsumoto, K., Sakikawa, N. & Miyata, T. Thermo-responsive gels that absorb moisture and ooze water. *Nat Commun* **9**, (2018).

39. Zhao, F. *et al.* Super Moisture-Absorbent Gels for All-Weather Atmospheric Water Harvesting. *Advanced Materials* **31**, (2019).

40. Qu, M., Abdelaziz, O., Sun, X. G. & Yin, H. Aqueous solution of [EMIM][OAc]: Property formulations for use in air conditioning equipment design. *Appl Therm Eng* **124**, 271–278 (2017).

41. Qu, M., Abdelaziz, O., Gao, Z. & Yin, H. Isothermal membrane-based air dehumidification: A comprehensive review. *Renewable and Sustainable Energy Reviews* **82**, 4060–4069 (2018).

42. Pesaran, A. A. Moisture Transport in Silica Gel Particle Beds. (University of California, Los Angeles, 1983).

43. Pesaran, A. A. & Mills, A. F. Moisture transport in silica gel packed beds-II. Experimental study. *Int J Heat Mass Transf* **30**, 1051–1060 (1987).

44. Intini, M., Goldsworthy, M., White, S. & Joppolo, C. M. Experimental analysis and numerical modelling of an AQSOA zeolite desiccant wheel. *Appl Therm Eng* **80**, 20–30 (2015).

45. Fumo, N. & Goswami, D. Y. Study of an aqueous lithium chloride desiccant system: Air dehumidification and desiccant regeneration. *Solar Energy* **72**, 351–361 (2002).

46. Gommed, K. & Grossman, G. A liquid desiccant system for solar cooling and dehumidification. *Journal of Solar Energy Engineering, Transactions of the ASME* **126**, 879–885 (2004).

47. Liu, X. H., Zhang, Y., Qu, K. Y. & Jiang, Y. Experimental study on mass transfer performances of cross flow dehumidifier using liquid desiccant. *Energy Convers Manag* **47**, 2682–2692 (2006).

48. Yin, Y. & Zhang, X. Comparative study on internally heated and adiabatic regenerators in liquid desiccant air conditioning system. *Build Environ* **45**, 1799–1807 (2010).

49. Qi, R., Lu, L. & Yang, H. Development of simplified prediction model for internally cooled/heated liquid desiccant dehumidification system. *Energy Build* **59**, 133–148 (2013).

50. Saman, W. Y. & Alizadeh, S. An experimental study of a cross-flow type plate heat exchanger for dehumidification / cooling. *Solar Energy* **73**, 59–71 (2002).

51. Kohno, Y. & Ohno, H. Temperature-responsive ionic liquid/water interfaces: Relation between hydrophilicity of ions and dynamic phase change. *Physical Chemistry Chemical Physics* **14**, 5063–5070 (2012).

52. Fukaya, Y., Sekikawa, K., Murata, K., Nakamura, N. & Ohno, H. Miscibility and phase behavior of water-dicarboxylic acid type ionic liquid mixed systems. *Chemical Communications* 3089–3091 (2007) doi:10.1039/b704992g.

53. Fukumoto, K. & Ohno, H. LCST-type phase changes of a mixture of water and ionic liquids derived from amino acids. *Angewandte Chemie - International Edition* **46**, 1852–1855 (2007).

54. Kohno, Y., Arai, H., Saita, S. & Ohno, H. Material design of ionic liquids to show temperature-sensitive lcst-type phase transition after mixing with water. *Aust J Chem* **64**, 1560–1567 (2011).

55. Saita, S., Kohno, Y. & Ohno, H. Detection of small differences in the hydrophilicity of ions using the LCST-type phase transition of an ionic liquid-water mixture. *Chemical Communications* **49**, 93–95 (2013).

56. Tian, S. *et al.* Fundamental and perspectives of thermo-responsive materials for dehumidification and water harvesting. *J Clean Prod* **412**, (2023).

57. Rao, A. K., Fix, A. J., Yang, Y. C. & Warsinger, D. M. Thermodynamic limits of atmospheric water harvesting. *Energy Environ Sci* **15**, 4025–4037 (2022).

58. Entezari, A., Esan, O. C., Yan, X., Wang, R. & An, L. Sorption-based Atmospheric Water Harvesting: Materials, Components, Systems, and Applications. *Advanced Materials* 2210957 (2023) doi:10.1002/adma.202210957.

59. Kocher, J. D., Menon, A. K. & Yee, S. K. An air conditioning cycle using lower critical solution temperature mixtures. in *Proceedings of the ASME 2023 Heat Transfer Summer Conference* (2023).

60. Longeras, O., Gautier, A., Ballerat-Busserolles, K. & Andanson, J. M. Deep Eutectic Solvent with Thermo-Switchable Hydrophobicity. *ACS Sustain Chem Eng* **8**, 12516–12520 (2020).

61. Flory, P. J. Thermodynamics of high polymer solutions. *Journal of Chemical Physics* **10**, 51–61 (1942).

62. Huggins, M. L. Theory of Solutions of High Polymers. *J Am Chem Soc* **64**, 1712–

1719 (1942).

63. Schweizer, K. S. & Curro, J. G. Integral equation theory of the structure and thermodynamics of polymer blends. *J Chem Phys* **91**, 5059–5081 (1989).

64. Yao, W., Hu, X. & Yang, Y. Modeling solubility of gases in semicrystalline polyethylene. *J Appl Polym Sci* **103**, 1737–1744 (2007).

65. Tambasco, M., Lipson, J. E. G. & Higgins, J. S. Blend miscibility and the Flory-Huggins interaction parameter: A critical examination. *Macromolecules* **39**, 4860–4868 (2006).

66. Ali, M. T. SI Psychrometric Chart (https://www.mathworks.com/matlabcentral/fileexchange/49154-si-psychrometric-chart), MATLAB Central File Exchange. Retrieved August 2, 2022 . Preprint at (2022).

67. Paulechka, Y. U., Kabo, A. G., Blokhin, A. V., Kabo, G. J. & Shevelyova, M. P. Heat capacity of ionic liquids: Experimental determination and correlations with molar volume. *J Chem Eng Data* **55**, 2719–2724 (2010).

68. Dai, Z. *et al.* Prediction and verification of heat capacities for pure ionic liquids. *Chin J Chem Eng* **31**, 169–176 (2021).

69. Fabre, E. & Murshed, S. M. S. A review of the thermophysical properties and potential of ionic liquids for thermal applications. *J Mater Chem A Mater* **9**, 15861–15879 (2021).

70. Oberg, V. & Goswami, D. Y. Performance of Simulation of Solar Hybrid Liquid Desiccant Cooling for Ventilation Air Preconditioning. in *Proceedings of the ASME International Solar Energy* 176–182 (1998).

71. Khalid Ahmed, C. S., Gandhidasan, P. & Al-Farayedhi, A. A. Simulation of a Hybrid Liquid Desiccant Based Air-Conditioning System. *Appl Therm Eng* **17**, 125–134 (1997).

72. Vrentas, J. S. & Vrentas, C. M. Sorption in Glassy Polymers. *Macromolecules* **24**, 2404–2412 (1991).

73. Bae, Y. H., Okano, T. & Kim, S. W. Temperature dependence of swelling of crosslinked poly(N,N′-alkyl substituted acrylamides) in water. *J Polym Sci B Polym Phys* **28**, 923–936 (1990).

74. Fox, T. G. Influence of Diluent and of Copolymer Composition on the Glass Temperature of a Polymer System. *Bull. Am. Phys. Soc* **1**, 123 (1956).

75. Smidsrod, O. & Guillet, J. E. Study of Polymer—Solute Interactions by Gas Chromatography. *Macromolecules* **2**, 272–277 (1968).

76. Chiantore, O., Costa, L. & Guaita, M. Glass Temperatures of Acrylamide Polymers. *Makromol. Chem., Rapid Commun* **3**, 303–309 (1982).

77. Capaccioli, S. & Ngai, K. L. Resolving the controversy on the glass transition temperature of water. *Journal of Chemical Physics* **135**, (2011).

78. Crank, J. The mathematics of diffusion. 2nd Edn. (1979) doi:10.1088/0031-9112/26/11/044.

79. Tanaka, T. KINETICS OF PHASE TRANSITION IN POLYMER GELS. *Physica* **140A**, 261–268 (1986).

80. Tanaka, T., Sato, E., Hirokawa, Y., Hirotsu, S. & Peetermans, J. Critical kinetics of volume phase transition of gels. *Phys Rev Lett* **55**, 2455–2458 (1985).

81. Radiator (engine cooling). *https://en.wikipedia.org/wiki/Radiator_(engine_cooling)#/media/File:Automobile_radiator.jpg* (2006).

82. ANSI/ASHRAE Standard 55. *Thermal Environmental Conditions for Human Occupancy*. (2020).

83. Fuller, J. J. & Marotta, E. E. Thermal Contact Conductance of Metal/Polymer Joints: An Analytical and Experimental Investigation. *J Thermophys Heat Trans* **15**, 228–238 (2001).

84. Ren, C. Q., Tu, M. & Wang, H. H. An analytical model for heat and mass transfer

processes in internally cooled or heated liquid desiccant – air contact units. *Int J Heat Mass Transf* **50**, 3545–3555 (2007).

85. Xiu-Wei, L., Xiao-Song, Z., Geng, W. & Rong-Quan, C. Research on ratio selection of a mixed liquid desiccant: Mixed LiCl- CaCl2 solution. *Solar Energy* **82**, 1161–1171 (2008).

86. Elmer, T., Worall, M., Wu, S. & Riffat, S. An experimental study of a novel integrated desiccant air conditioning system for building applications. *Energy Build* **111**, 434–445 (2016).

87. Koronaki, I. P., Christodoulaki, R. I., Papaefthimiou, V. D. & Rogdakis, E. D. Thermodynamic analysis of a counter flow adiabatic dehumidifier with different liquid desiccant materials. in *Applied Thermal Engineering* vol. 50 361–373 (2013).

88. Li, H. K., Cai, G. M., Fan, J. J. & Jin, Z. P. Subsolidus phase relations in CaO-In 2O 3-B 2O 3 system and crystal structure of CaInBO 4. *J Alloys Compd* **516**, 107–112 (2012).

89. Bourdoukan, P., Wurtz, E. & Joubert, P. Experimental investigation of a solar desiccant cooling installation. *Solar Energy* **83**, 2059–2073 (2009).

90. Kabeel, A. E. Solar powered air conditioning system using rotary honeycomb desiccant wheel. *Renew Energy* **32**, 1842–1857 (2007).

91. Mei, L., Infield, D., Eicker, U., Loveday, D. & Fux, V. Cooling potential of ventilated PV façade and solar air heaters combined with a desiccant cooling machine. *Renew Energy* **31**, 1265–1278 (2006).

92. Schweizer, K. S. & Curro, J. G. Integral equation theory of the structure and thermodynamics of polymer blends. *J Chem Phys* **91**, 5059–5081 (1989).

93. Tambasco, M., Lipson, J. E. G. & Higgins, J. S. Blend miscibility and the Flory-Huggins interaction parameter: A critical examination. *Macromolecules* **39**, 4860–4868 (2006).

94. Silke Rathgeber. Chapter 4- POLYMER SOLUTIONS AND MIXTURES.

Johannes Gutenberg-University Mainz 1–34 https://userpages.uni-koblenz.de/~rathgeber/Lectures/Chap4_Polymer_Solution.pdf (2021).

95. John L. Monteith and Mike H. Unsworth. *Principles of Environmental Physics: Plants, Animals, and the Atmosphere*. *Academic Press.* vol. 124 (Academic Press, 2013).

96. Callister Jr, W. D. & Rethwisch, D. G. *Materials Science and Engineering - An Introduction*. *Wiley* (Wiley, 2018).

APPENDIX A

SUPPORTING INFORMATION FOR CHAPTER 2

A.1.1. Flory-Huggins Theory of Mixing

The Flory Huggins theory[61,62] of mixing is a lattice theory in which the lattice points are occupied by the molecules of the two components that are mixed. This theory is most frequently used to model the mixing of the two polymers or a polymer with a small molecule solvent. Here we utilize this theory to describe the mixing of two small molecules (water and ionic liquid). Whether or not the mixture is miscible at a particular temperature is determined by Gibbs free energy of mixing, ΔG_{mix}.

We begin by considering the lattice shown in Figure A1, which shows lattice sites occupied by the two different molecules, A (white) and B (black). The number of lattice sites that a molecule occupies is determined by its size. In our case, we assume that since water and ionic liquid molecules are of similar sizes (relative to the frequently analyzed case of large polymer chains), and that they each occupy one lattice site per molecule of water or ionic liquid.

n_A = number of lattice sites for component A

n_B = number of lattice sites for component B

$n = n_A + n_B$ = total number of lattice sites

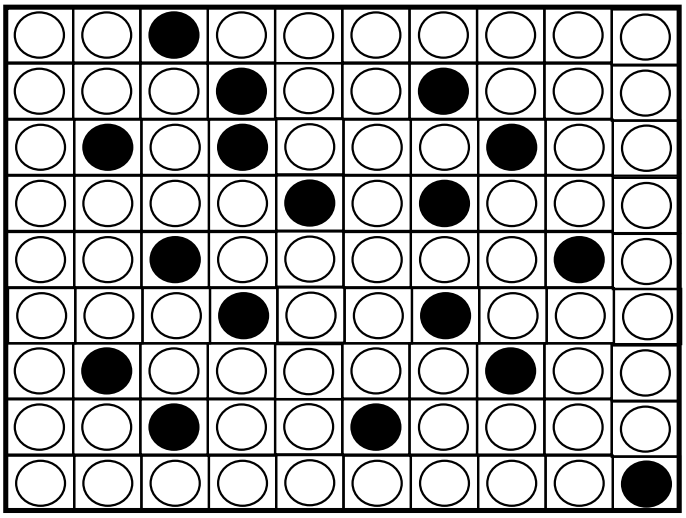

Figure A1: Lattice showing the arrangement of two solvents molecules like water and ionic liquid of similar sizes.

A.1.2. Calculating the Entropy of Mixing

In order to determine the entropy of mixing, we begin with the statistical mechanics definition of entropy:

$$\Delta S_{mix} = k_B ln\,(\Omega) \tag{A-1}$$

where Ω is the number of possible distributions of component A and B on the lattice sites. The number of possible permutations of arranging A and B in the lattice is given by

$$\Omega = \frac{n!}{n_A!\, n_B!} \tag{A-2}$$

With the approximation, $\ln x! \approx x \ln x - x$, we can write ΔS_{mix} as shown below

$$\Delta S_{\text{mix}} = -k_B \left[n_A \ln\left(\frac{n_A}{n}\right) + n_B \ln\left(\frac{n_B}{n}\right)\right] \tag{A-3}$$

The above Equation can also be written as follows by multiplying by n/n

$$\Delta S_{\text{mix}} = -nk_B \left[\frac{n_A}{n} \ln\left(\frac{n_A}{n}\right) + \frac{n_B}{n} \ln\left(\frac{n_B}{n}\right)\right] \tag{A-4}$$

Where $\frac{n_A}{n}$ and $\frac{n_B}{n}$ are the number fractions of *A* and *B*, ($\frac{n_A}{n} = c_A$ and $\frac{n_B}{n} = c_B$). When the two components are of similar sizes and occupy one lattice per molecule, volume fractions ($\phi_A \; and \; \phi_B$) are equal to number fractions (c_A and c_B). Also, since mole fraction (x_A and x_B) is equal to number fraction, it is also equal to volume fraction ($x_A = c_A = \phi_A \; and \; x_A = c_A = \phi_A$). From here on, the entropy of mixing will be expressed in terms of mole fraction, which is shown in Equation (A-5),

$$\Delta S_{mix} = -nk_B[x_A \ln(x_A) + x_B \ln(x_B)] \quad \text{(A-5)}$$

If the total number of the molecules is equal Avogadro's number ($n = N_A$), then the coefficient in Equation (A-5) become $N_A k_B = R$, where *R* is the universal gas constant. Writing the entropy on a molar basis, Equation (A-5) can then be rewritten as:

$$\Delta s_{mix} = -R[x_A \ln(x_A) + x_B \ln(x_B)] \quad \text{(A-6)}$$

A.1.3. Calculating the Enthalpy of Mixing,

The enthalpy will be a function of the coordination number, *z* (*i.e.*, the number of nearest neighbors) and the pairwise interaction energy between neighbors. In a binary mixture of *A* and *B*, there are three possible interaction energies, w_{AA}, w_{AB}, and w_{BB}. Within the mixture, every lattice site is on average surrounded by $c_A z$ neighbors of component *A* and by $c_B z$ neighbors of component B. The enthalpy for a mixture of A and B (H_{mix}) can then be written as

$$H_{mix} = H_A + H_B \quad \text{(A-7)}$$

$$H_A = \frac{1}{2} n c_A (c_A \, z \, w_{AA} + c_B \, z \, w_{AB}) \quad \text{(A-8)}$$

$$H_B = \frac{1}{2} n c_B (c_A \, z \, w_{AB} + c_B \, z \, w_{BB}) \quad \text{(A-9)}$$

where the ½ in the coefficient prevents double counting of the interactions between pairs. The reference states for the enthalpy of mixing correspond to the unmixed states:

$$H_{unmixed} = H_A^0 + H_B^0 \quad \text{(A-10)}$$

$$H_A^0 = \frac{1}{2} n c_A \, z \, w_{AA} \quad \text{(A-11)}$$

$$H_B^0 = \frac{1}{2} n c_B \, z \, w_{BB} \quad \text{(A-12)}$$

The enthalpy change due to mixing (ΔH_{mix}) corresponds to the difference between the mixed and unmixed states:

$$\Delta H_{\text{mix}} = H_{mix} - H_{unmixed} = \frac{1}{2} n z c_A c_B (2 \, w_{AB} - \, w_{AA} - \, w_{BB}) \quad \text{(A-13)}$$

We let $\Delta w_{AB} = \, w_{AB} - \frac{1}{2} (\, w_{AA} + \, w_{BB})$, which is the differential interaction energy between the two components. Equation (A-13) can then be rewritten as

$$\Delta H_{\text{mix}} = n z c_A c_B \, \Delta w_{AB} \quad \text{(A-14)}$$

If we let $n = N_A$ and also substitute mole fractions (x) for number fractions (c), Equation (A-12) can be written on a molar basis:

$$\Delta h_{\text{mix}} = z \, x_A x_B \Delta w_{AB} \quad \text{(A-15)}$$

Rather than using Δw_{AB} this Equation is often rewritten in terms of a dimensionless parameter called the Flory-Huggins interaction parameter, χ_{AB}, which is defined as:

$$\chi_{AB} = \frac{z\,\Delta w_{AB}}{RT} \tag{A-16}$$

If we substitute the Flory-Huggins parameter into Equation (A-15), we arrive at the following expression for the enthalpy of mixing as given by Equation (A-17).

$$\Delta h_{\text{mix}} = \chi_{AB}\ x_A x_B\ RT \tag{A-17}$$

A.1.4. The Gibbs Free Energy of Mixing

The Gibbs free energy per mole shown is obtained by combining Equations (A-6) and (A-17) to obtain the Equation below.

$$\Delta g_{mix} = \Delta h_{\text{mix}} - T\Delta s_{\text{mix}} = RT\left(x_A\, ln\, x_A + x_B\, ln\, x_B + \chi_{AB}\ x_A x_B\right) \tag{A-18}$$

where R is the universal gas constant, x_A and x_B are mole fractions of *A* and *B* respectively, *T* is absolute temperature and χ_{AB} is the Flory-Huggins interaction parameter between *A* and *B*.

The Flory-Huggins interaction parameter, χ_{AB}, is unitless and depends on temperature. This interaction is often expressed as the sum of two terms as shown in the equation below.[92] In this expression χ_S (unitless) is referred to as the entropic term and χ_H (units of temperature) is referred to as the enthalpic term.

$$\chi_{AB} = \chi_S + \frac{\chi_H}{T} \tag{A-19}$$

A positive value of χ_H is associated with mixtures that have an upper critical solution temperature (UCST) and a negative value of χ_H is associated with mixtures that have a

lower critical solution temperature (LCST).[93] The process of obtaining χ_S and χ_H is often done empirically.

This manuscript focuses on the case of LCST mixtures. Consequently, and for the purposes of this study, it is more intuitive to re-write these equations in terms χ_H and T_{LCST} as opposed to χ_H and χ_S. This is because T_{LCST} directly maps onto the phase diagram and conveniently ties into the engineering analysis of the dehumidification system. First, we rewrite Equation (A-18) by using the mole fraction of ionic liquid $x_B = x$ and mole fraction of water $x_A = 1 - x$. That gives us the Gibbs free energy change of mixing as shown in Equation (A-20).

$$\Delta g_{mix} = RT\big((1-x)\,ln(1-x) + x\,ln\,x + \chi_{AB}\,x(1-x)\big) \tag{A-20}$$

The stability of the mixture is determined by the mixing free energy of the mixture, Δg_{mix}. For the mixture to be stable the following two conditions need to be satisfied.

$$\Delta g_{mix} < 0 \tag{A-21}$$

$$\left(\frac{\partial^2 \Delta g_{mix}}{\partial x^2}\right)_{T,p} > 0 \tag{A-22}$$

Figure A2a shows a typical graph of the Gibbs free energy for mixing with mole fraction at a fixed temperature. The binodal points correspond to the points where the 1st derivative is zero, $\left(\frac{\partial \Delta g_{mix}}{\partial x}\right)_{T,p} = 0$. Figure A2a shows a case where there are two binodal points. In this case, the mixture is a stable and single phase in the region to the left of the

left binodal point. It is also stable and single phase in the region to the right of right binodal point.

Thermodynamics dictates that the region between the two binodal points will separate into two phases. These two phases correspond to an ionic-liquid-rich phase and a water-rich-phase, each of which will have concentrations corresponding to their respective binodal points. The region between the binodal points can be further divided into a metastable region and an unstable region. The spinodal points correspond to points where the 2nd derivative is zero, $\left(\frac{\partial^2 \Delta g_m}{\partial x^2}\right)_{T,p} = 0$. The region between the two spinodal points define the unstable region, in which phase separation occurs via spinodal decomposition and happens near instantaneously. The region between the binodal and spinodal points define the metastable region, where phase separation occurs via nucleation and growth.

Figure A2b illustrates how the LCST phase diagram is formed by the Gibbs free energy curves (Figure A2a). The Gibbs free energy curve is itself a function of temperature and the top half of Figure A2b illustrates this curve at several different temperatures. The bottom half of Figure A2b illustrates the resulting phase diagram. The phase diagram is created by creating a curve that consists of the locus of binodal points for all Gibbs free energy curves (*i.e.,* green curve in Figure A2b). This curve is called the immiscibility curve and it separates miscible and immiscible regions (single phase and two-phase regions) in the phase diagram.

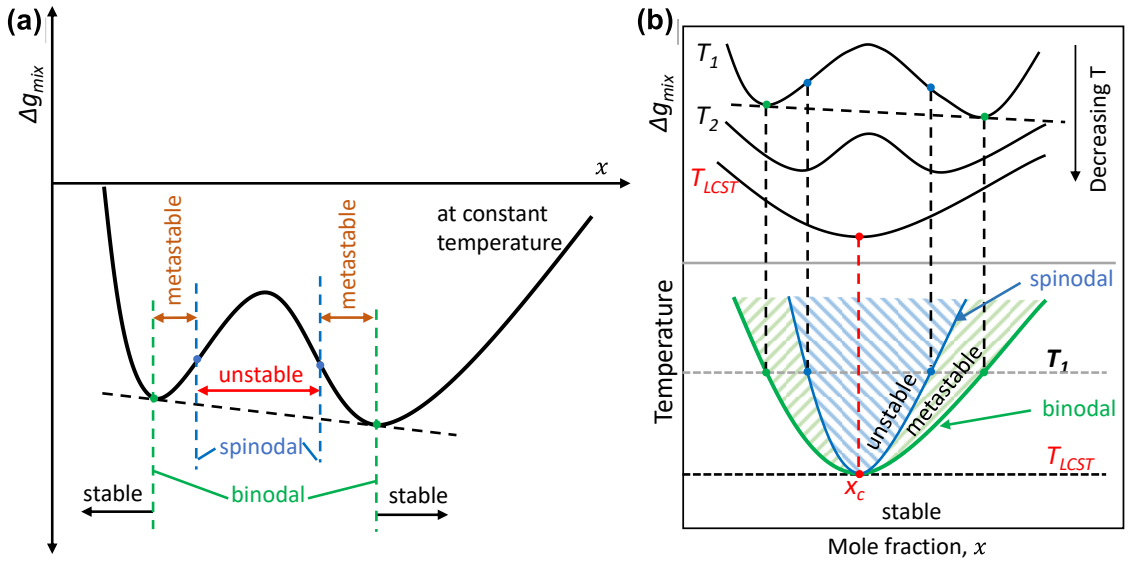

Figure A2: (a) Gibbs free energy of mixing as a function of mole fraction at a particular temperature. (b) Illustration of how the temperature dependence of Gibbs free energy leads to an immiscibility curve in the phase diagram. This figure is adapted from [94].

Since the curve separating miscible and immiscible is dictated by the binodal points, we can write a corresponding expression for the Flory-Huggins parameter by setting the first derivative of Equation (A-20) to zero, $\left(\frac{\partial \Delta g_m}{\partial x}\right)_{T,p} = 0$, and then solving for the Flory-Huggins parameter. We then arrive at the following relation.

$$\chi_{AB} = \left(\frac{1}{1-2x}\right) ln\left(\frac{1-x}{x}\right) \tag{A-23}$$

The spinodal points are given by the 2nd derivative of the Equation (A-20) and setting that to zero $\left(\frac{\partial^2 \Delta g_m}{\partial x^2}\right)_{T,p} = 0$, and then solving for the Flory-Huggins parameter. We then arrive at the following relation for the spinodal curve.

$$\chi_{AB} = \frac{1}{2}\left(\frac{1}{x} + \frac{1}{1-x}\right) \tag{A-24}$$

We can see in Figure A2b that there is a critical point when the spinodal and binodal points merge at a particular temperature. This temperature is the LCST temperature, T_{LCST}, and occurs when the 3rd derivative of the Gibbs free energy is equal to zero, $\left(\frac{\partial^3 \Delta g_m}{\partial x^3}\right)_{T,p} = 0$ (which is mathematically equivalent to the extremum of the 2nd derivative (Spinodal curve)). The critical point on the phase diagram is defined by the *LCST* temperature and a critical mole fraction, x_c. In the generalized Flory-Huggins solution, x_c is a function of the size ratio of the two component molecules (which can be very large in the case of polymer-solvent mixtures). However, in our case when the two components are of the same size, the critical mole fraction simplifies to $x_c = 0.5$.

The critical interaction parameter is calculated by substituting $x_c = 0.5$ into Equation (A-24), and in doing so, we find that χ_c = 2. By definition, the temperature at which the critical point is achieved is called the *LCST* temperature (T_{LCST}) for a curve that is concave upwards. At this critical point, the critical interaction parameter can be written as shown in Equation (A-25).

$$\chi_c = \chi_S + \frac{\chi_H}{T_{LCST}} \tag{A-25}$$

Assuming that χ_S and χ_H are constants, we can combine Equation (A-24) and Equation (A-25) and arrive at final equation for interaction parameter with two unknown variables χ_H and *T*.

$$\chi_{AB} = \chi_c + \chi_H \left(\frac{1}{T} - \frac{1}{T_{LCST}}\right) \tag{A-26}$$

Since Equation (A-23) and Equation (A-26) both represent interaction parameter, χ_{AB}, equating the two equations and setting χ_c = 2 gives us the *T*-x relation in terms of T_{LCST}, x and χ_H. This relation is then given by Equation (A-27) and graphically illustrated in Figure A2a and Figure A2b.

$$T = \frac{1}{\frac{1}{T_{LCST}} + \frac{\left(\frac{1}{1-2x}\right) ln\left(\frac{1-x}{x}\right) - 2}{\chi_H}} \tag{A-27}$$

The *T*-x relation shown in Equation (A-27) will determine the shape of the phase diagram at different LCST temperatures and enthalpic interaction parameters, χ_H. We can see in Figure A3a that when the T_{LCST} is kept constant and χ_H is varied, there is a change in curvature of the curve. Figure A3b shows that when T_{LCST} is varied, there is no change in curvature, but the vertex is vertically shifted.

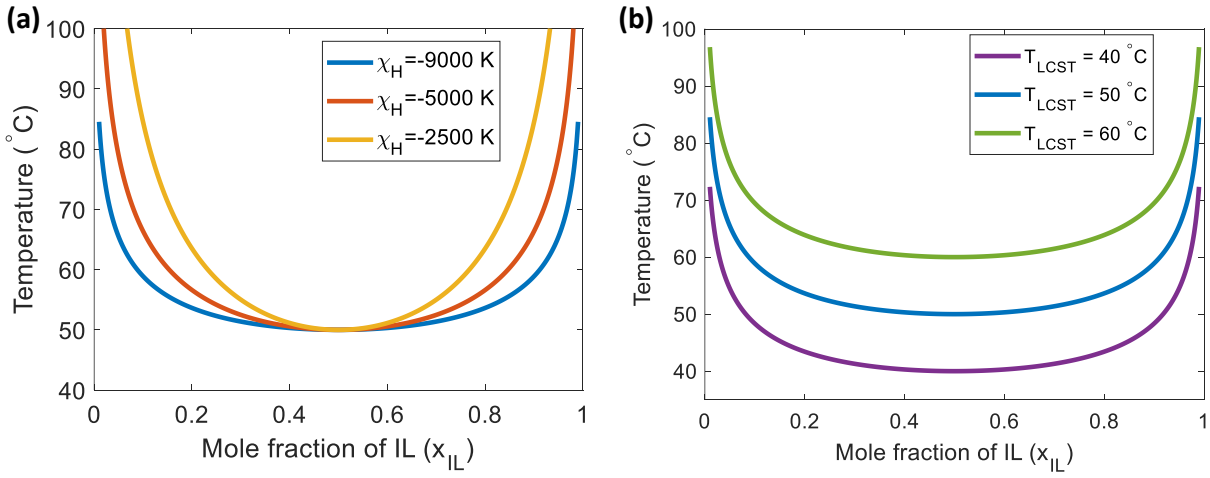

Figure A3: Phase diagram (T-x) at (a) T_{LCST}= 50 °C and different enthalpic interaction parameters, χ_H and at (b) χ_H=-9000 K and different LCST temperatures

We can now write Δh_{mix} as follows in Equation (A-28) by substituting the value of χ_{AB} from Equation (A-26)

$$\Delta h_{\text{mix}} = \left[\chi_c + \chi_H \left(\frac{1}{T} - \frac{1}{T_{LCST}}\right)\right] \; x_A x_B RT \tag{A-28}$$

Δh_{mix} is the enthalpy change due to mixing when the pure components *A* and *B* are mixed together to form a mixture with mole fractions x_A and x_B at temperature *T*. Since the beginning state is the unmixed state, we can simply write it as h_{mix} in the following Equation (A-29)

$$h_{\text{mix}} = \left[\chi_c + \chi_H \left(\frac{1}{T} - \frac{1}{T_{LCST}}\right)\right] \; x_A x_B \; RT \tag{A-29}$$

A.2.1. System modeling

The schematic for a single-stage liquid LCST dehumidification cycle is shown in Figure A4. The main components include the absorber that absorbs water vapor from moist air and the desorber (regeneration stage) that consists of a heater and a separator which regenerates the liquid desiccant. Other components include a heat exchanger that cools the regenerated liquid solution to a low (absorption) temperature, mixer that mixes the regenerated liquid solution and fresh added ionic liquid, and a recuperator that exchanges heat between cold liquid entering the Regeneration Stage and hot ionic liquid exiting the Regeneration Stage. The modeling of each component is described below in the following sections.

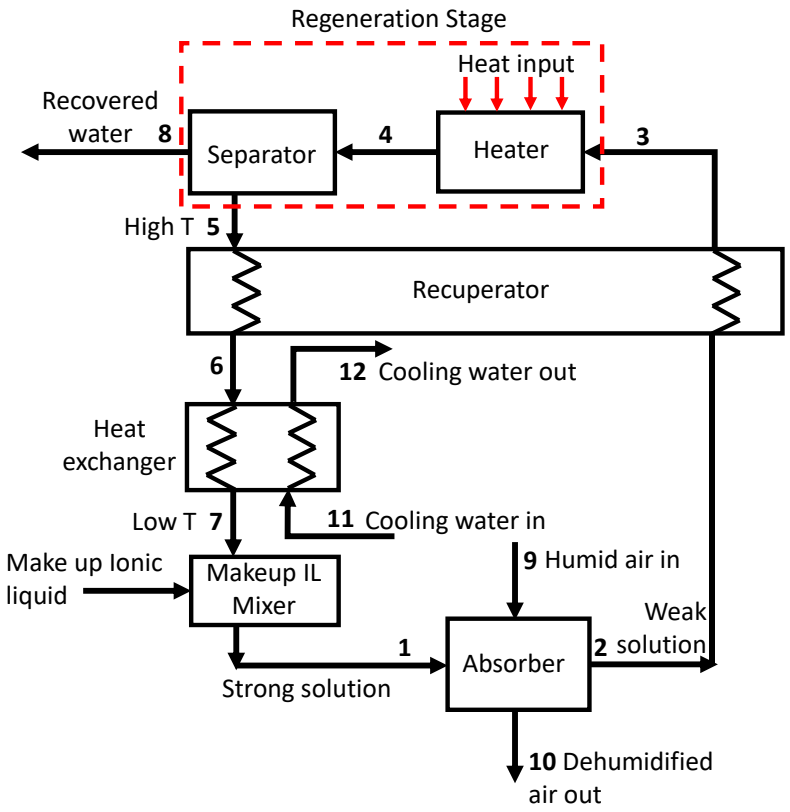

Figure A4: Schematic of a 1-stage LCST ionic liquid (IL) dehumidification cycle

A.2.2. Absorber Modeling

Figure A5 illustrates the absorber model used in our thermodynamic analysis. A strong ionic liquid solution (*i.e.*, solution that is rich in ionic liquid) enters the absorber and absorbs the water vapor from the humid air. We model the absorption process using moisture absorption effectiveness, ε_{ma}. The moisture absorption effectiveness relates the change in humidity ratio of the air that enters and exits the absorber and is denoted by Equation (A-30)

$$\varepsilon_{ma} = \frac{\omega_{a,9} - \omega_{a,10}}{\omega_{a,9} - \omega_{I,9}} \tag{A-30}$$

where $\omega_{a,9}$ is the humidity ratio of air entering the absorber

$\omega_{a,10}$ is the humidity ratio of air exiting the absorber

$\omega_{I,9}$ is humidity ratio of the air at air-solution interface at the absorber inlet

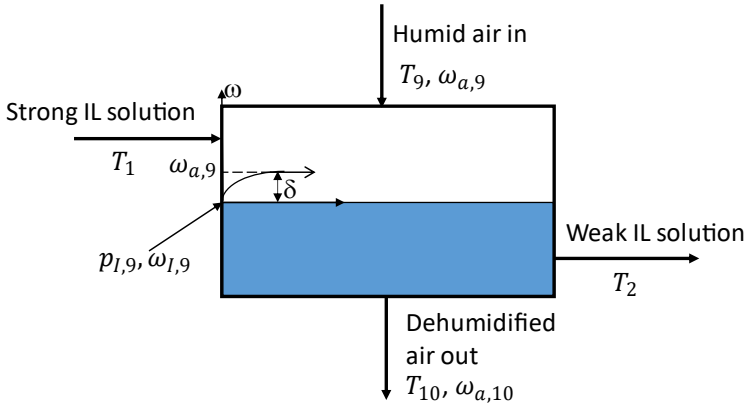

Figure A5: Schematic of the absorber model used for our thermodynamic analysis

To better understand the concept of $\omega_{I,9}$, Figure A5 shows the humidity ratio gradient (ω-gradient) near the air-solution interface at the absorber inlet. The air has its maximum water vapor content when it enters the absorber and the least when it exits. There is also an ω-gradient near the air-solution interface. As we approach the air-solution interface, ω starts decreasing and reaches a minimum value at it condenses on the interface. It is this gradient that drives the condensation of the water vapor. The maximum possible change in ω is $\omega_{a,9} - \omega_{I,9}$ and the actual change is $\omega_{a,9} - \omega_{a,10}$. Therefore, the moisture absorption effectiveness is defined at the ratio of maximum possible change over the actual change (*i.e.*, similar to how a heat exchanger effectiveness is defined).

The humidity ratios can be further related to the partial pressure of water vapor. Therefore, Equation (A-30) can be rewritten as:

$$\varepsilon_{ma} = \frac{p_{w,9} - p_{w,10}}{p_{w,9} - p_{I,9}} \tag{A-31}$$

Where $p_{w,9}$ is partial pressure of water in the air entering the absorber, $p_{w,10}$ is the partial pressure of water in the air exiting the absorber, and $p_{I,9}$ is the partial pressure of water at the air-solution interface at the inlet to the absorber.

At the interface, the air and ionic liquid solution are at equilibrium, and this is assumed to be at the inlet temperature of the ionic liquid solution, T_1. We know that $\omega_{I,9} = f(T_1, p_{I,9})$ and $p_{I,9}$ is dependent on the concentration of the ionic liquid in the solution at the absorber inlet. Therefore $p_{I,9}$ can be written as follows in Equation (A-31) using the Raoult's law for ideal mixtures.

$$p_{I,9} = x_{H2O}\, p_{H2O} + x_{IL}\, p_{IL} \tag{A-32}$$

Where x_{H2O} and x_{IL} are the mole fractions of the water and ionic liquid in the solution and p_{H2O} and p_{IL} are their respective partial pressures at the temperature T_1. Since the partial pressure of an ionic liquid is much less than that of water, $p_{IL} << p_{H2O}$, the 2nd term in Equation (A-32) can be neglected. In addition, we will often refer to concentration in terms of mass fractions instead of mole fractions. In this scenario, Equation (A-32) is

rewritten in terms of mass fraction, *C*, and molecular weight *M*, in Equation (A-33)

$$p_{I,9} = \frac{C_{H2O}\, M_{IL}}{C_{H2O}\, M_{IL} + C_{IL}\, M_{H2O}}\, p_{H2O} \tag{A-33}$$

The vapor pressure of water, p_{H2O} was estimated using Tetens equations by Monteith and Unsworth [95] for temperature greater than 0 ℃ shown below in Equation (A-34)

$$p_{H2O} = 0.61078\ \exp\left(\frac{17.27T}{T + 237.3}\right) \tag{A-34}$$

Where *T* is in ℃ and p_{H2O} is in *kPa*

A.2.3. Recuperator Modeling

The recuperator shown in Figure A6 is added so that the regeneration input heat can be reduced. The recuperator transfers heat from the strong ionic liquid solution leaving the Regeneration Stage and the weak ionic liquid solution entering the Regeneration Stage. This decreases the amount of heat needed during regeneration and it also reduces the cooling load on the heat exchanger. We assume the effectiveness of the recuperator, ε_{rec}, to be 70%. The exit temperatures leaving the recuperator can be written as shown in Equations (A-35) and (A-36). In these equations, T_5 is the regeneration temperature and known and T_2 is the solution temperature leaving the absorber, which is also known.

$$T_3 = T_2 - \varepsilon_{rec}(T_2 - T_5) \tag{A-35}$$

$$T_6 = T_5 - \varepsilon_{rec}(T_5 - T_2) \tag{A-36}$$

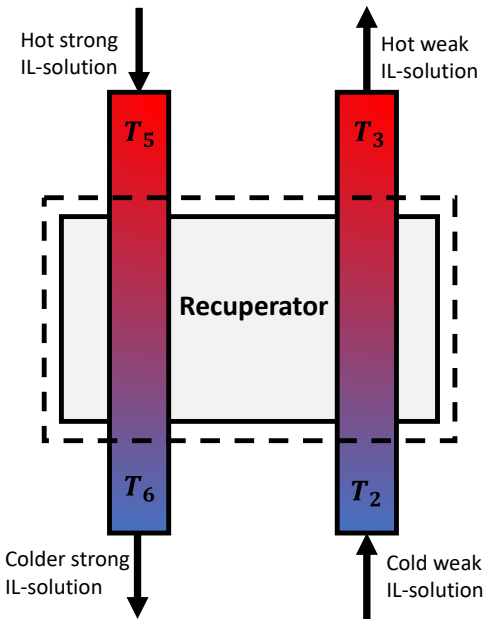

Figure A6: Recuperator diagram illustrating preheat of the weak ionic liquid solution and precooling of the strong ionic liquid solution

A.2.4. Heater Modeling

The heater makes up the first component of the Regeneration Stage. It heats the ionic liquid solution to a temperature above the *LCST* temperature, where it can be separated into two distinct phases (a water-rich-phase and an ionic-liquid-rich-phase). The masses of the two phases are determined using the lever rule for binary mixtures.[96]

The heat input rate into the heater is given by Equation (A-37), where $c_{p,s}$ is the specific heat of the IL-solution and $\dot{m}_2$ is the mass flow rate of the IL solution through the heater. T_4 is the regeneration temperature which is indirectly chosen by choosing excess regeneration temperature ($\Delta T_{reg,exs}$) within our model. The enthalpy of mixing (Equation (A-38)) is calculated in accordance with the Flory-Huggins theory.

$$\dot{Q}_{reg} = \dot{m}_3 c_{p,s}(T_4 - T_3) + \Delta\dot{H}_{demix} \quad \text{(A-37)}$$

$$\Delta\dot{H}_{demix} = \dot{m}_4 h_{4,mix} - (\dot{m}_5 h_{5,mix} + \dot{m}_8 h_{8,mix}) \quad \text{(A-38)}$$

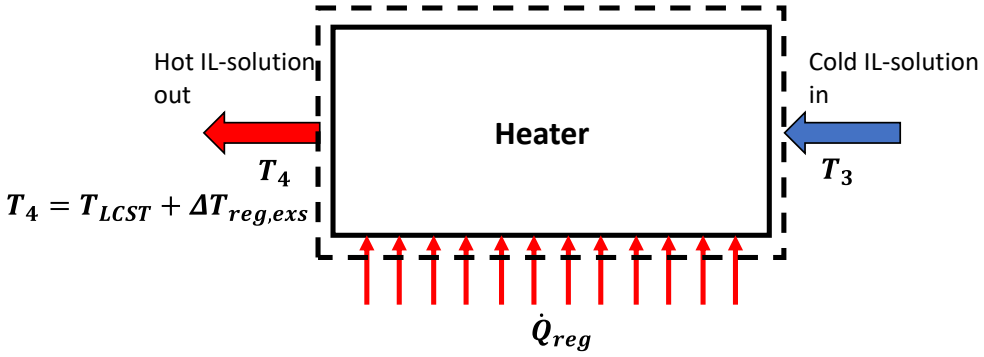

Figure A7: Heater schematic for regeneration of the ionic liquid solution

A.2.5. Separator Modeling

For the purposes of modeling the separator, we assume that gravity and the density difference between the water-rich and ionic-rich solutions are sufficient to obtain the desired separation. In this limit, there is no work input into the separator. We acknowledge that in practice such a process might be too slow and methods of speeding the process up (*i.e.*, a centrifugal extractor) and a corresponding work input (which may or may not be negligible compared to the thermal energy input) may be needed. However, since this study focuses on thermodynamics (as opposed to transport kinetics), we consider the case of no work input into the separator.

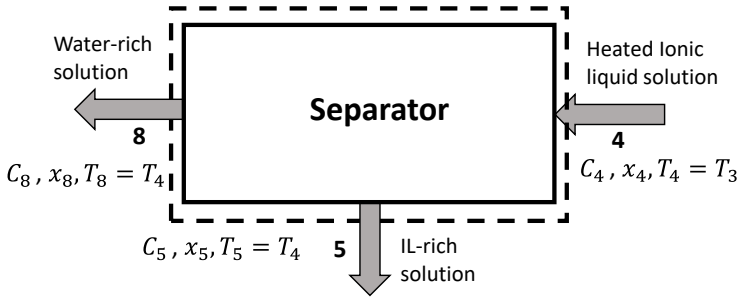

Figure A8: Schematic of a separator separating the heated ionic liquid solution into water-rich and IL-rich phases

A.2.6. Heat Exchanger Modeling

The ionic liquid solution after the Regeneration Stage is still at high temperature and so it needs to be cooled to a temperature below the LCST temperature so it can absorb fresh water from the humid air in the absorber. A representative model for this heat exchanger is shown in Figure A9. In our simulation, we set T_7 to be the absorption temperature ($T_1 \approx$ 32℃). This implicitly assumes that the cooling water flow rate and/or the cooling water inlet temperature can achieve the necessary amount of heat removal. Presumably, the cooling water loop rejects its heat to the outdoors and so the outdoor temperature represents a lower limit to the cooling water temperature (T_{11}). In our simulation, we set the inlet air temperature to the absorber ($T_9 = 30℃$) and so our choice of setting $T_7 \approx 32℃$ is consistent with this.

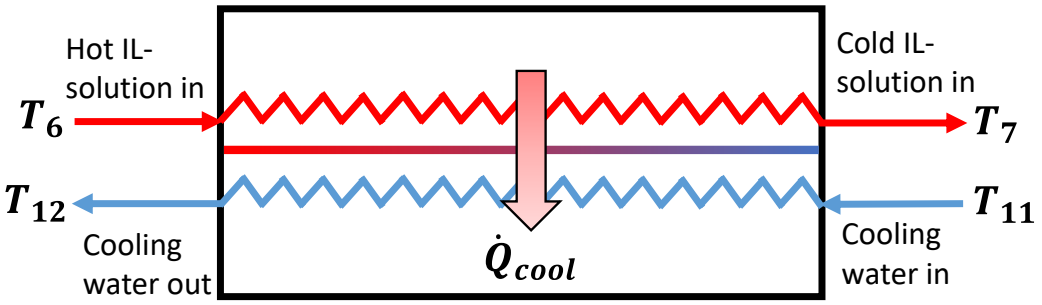

Figure A9: Heat exchanger schematic showing cooling of ionic liquid solution to absorption temperature using cooling water

A.2.7. Mixer Modeling

Our single-stage system has only one mixer that is used to supply makeup-IL, however multi-stage systems have multiple mixers and so we present a mixer model that can be used for the generalized case.

In general, a mixer mixes two IL-solutions at different concentrations and temperatures to give a uniformly mixed solution with a uniform temperature and concentration. This requires us to also consider the enthalpy of mixing (Flory-Huggins theory explained above). We consider a mixer mixing two ionic liquid solutions, *a* and *b* with different concentrations and temperatures to give a mixed solution *c* as shown in Figure A10. The resulting temperature of the mixed solution is calculated by applying an energy balance on the mixer as shown in Equation (A-39). The enthalpy of mixing, $\Delta\dot{H}_{mix}$ is obtained from Flory-Huggins theory given the temperature and the mole fraction of the solution as shown in Equation (A-40). The specific heat of the solution is determined by applying the

weighted average of specific heat of ionic liquid and water concentration in the solution as shown in Equation (A-41).

Equation (A-42) shows how the mass fraction (C_c) of ionic liquid in the mixed solution (denoted with a subscript *c*) is calculated given the incoming masses and concentration of the incoming streams (denoted with subscripts *a* and *b*). The mole fraction, x_c can be obtained from mass fraction and molecular weight of water and ionic liquid using Equation (A-43).

$$T_c = \frac{\dot{m}_a c_{pa}\, T_a + \dot{m}_b c_{pb} T_b + \Delta\dot{H}_{mix}}{\dot{m}_c\, c_{pc}} \tag{A-39}$$

$$\Delta\dot{H}_{mix} = \dot{m}_c h_{mix}(x_c, T_c) - \dot{m}_a h_{mix}(x_a, T_a) - \dot{m}_b h_{mix}(x_b, T_b) \tag{A-40}$$

$$c_{pc} = c_{p,IL} C_c + c_{p,w}(1 - C_c) \tag{A-41}$$

$$C_c = \frac{\dot{m}_a C_a + \dot{m}_b C_b}{\dot{m}_a + \dot{m}_b} \tag{A-42}$$

$$x_c = \frac{1}{1 + \left(\frac{M_{IL}}{M_w}\right)\left(\frac{1}{C_c} - 1\right)} \tag{A-43}$$

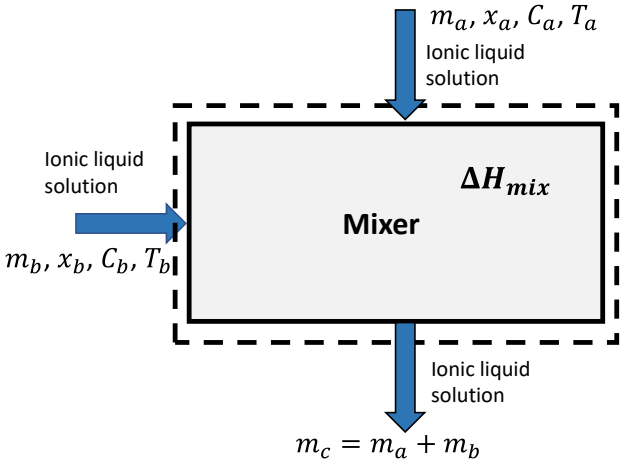

Figure A10: Mixer used to mix the regenerated ionic liquid solution and make-up ionic liquid

A.2.8. Multi-Stage Modeling

A single stage dehumidification cycle involves regeneration with a single regeneration stage (*i.e.*, one heater and one separator). However, system coefficient of performance can often be improved by using multiple regeneration stages. Figure A11 shows the schematic of an *n*-stage regeneration dehumidification cycle. In our *n*-stage regeneration configuration, the water-rich phase leaving the previous regeneration stage is further heated to a higher temperature. For example, Figure A11 shows that the water-rich phase exiting Separator-1 (Point 8) is heated in Heater-2 which and then subsequently separated out into IL-rich phase and water-rich phase in Separator-2. This process continues again for subsequent regeneration stages.

For our multi-state regeneration configurations, all of the IL-rich phase solutions from all of the regeneration stages are mixed in a Multi-stage Mixer (Point 14) and modeled as described in the previous section (but with a slight modification). In this case, the regeneration heat is the sum of all the input heat from all the heaters in all of the stages as shown in Equation (A-44).

$$\dot{Q}_{reg,IL} = \dot{m}_3 c_{p,s1}\left(T_{regen,1} - T_3\right) + \Delta\dot{H}_{demix,1} + \dot{m}_8 c_{p,s2}\left(T_{regen,2} - T_{regen,1}\right) + \Delta\dot{H}_{demix,2} + \cdots + \dot{m}_n c_{p,sn}\left(T_{regen,n} - T_{regen,n-1}\right) + \Delta\dot{H}_{demix,n} \quad \text{(A-44)}$$

In Equation (A-44) shown above, $\dot{m}_3$, $\dot{m}_8$, $\dot{m}_n$ are the mass flow rates of the IL-solution going into Regeneration Stage-1, Stage-2, and Stage-*n*, respectively. Similarly, $T_{regen,1}$, $T_{regen,2}$, $T_{regen,n}$ are regeneration temperatures for Stage-1, Stage-2, and Stage-*n*, respectively. $\Delta\dot{H}_{demix,1}$, $\Delta\dot{H}_{demix,2}$, $\Delta\dot{H}_{demix,n}$ correspond to the enthalpy of the demixing in each respective stage.

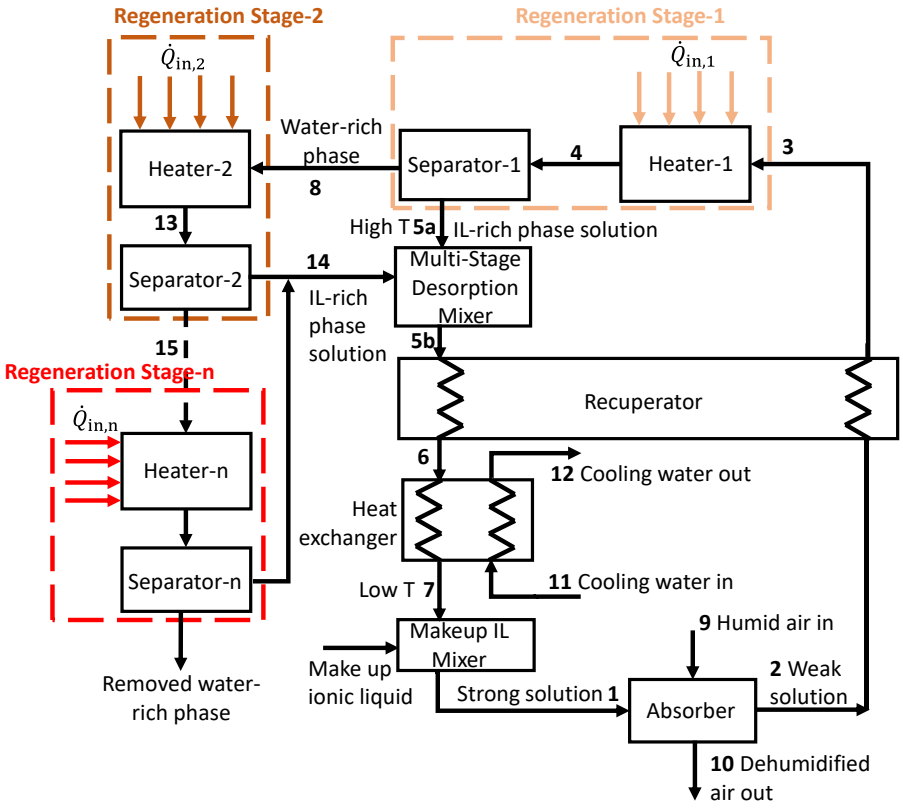

Figure A11: A multi-stage regeneration dehumidification cycle

A.3. Second Law Entropy Balance Analysis for the LCST Dehumidification Cycle

To understand and quantify the irreversibility's in our system, we have performed entropy balance for our dehumidification cycle. By doing an entropy balance, we can identify where irreversibilities occur, such as in heat transfer, mixing, demixing etc. For any given control volume entropy balance is described by the following equation.

$$\frac{dS_{CV}}{dt} = \sum \frac{\dot{Q}_k}{T_k} + \sum \dot{m}_e s_e - \sum \dot{m}_i s_i + \dot{S}_{gen} \quad \text{(A-45)}$$

In the above equation, $\frac{dS_{CV}}{dt}$ is the entropy change within the control volume which is zero for steady state, $\sum \frac{\dot{Q}_k}{T_k}$ is the entropy changed dure to heat transfer across the control volume, $\sum \dot{m}_e s_e$ and $\sum \dot{m}_i s_i$ is the sum of entropy of the streams leaving and entering the control volume and $\dot{S}_{gen}$ is the total entropy generation. In these following subsections, entropy balance is performed separately for each component and the entropy generation is summed up to obtain the entropy generated in the entire dehumidification system cycle.

1. Entropy Balance of the Absorber

In the absorber, the assumption is that there is no heat transfer to or from the absorber to the surrounding. So, the entropy balance (Equation 6.45) reduces to

$$\dot{S}_{gen,abs} = (\dot{m}_2 s_2 - \dot{m}_1 s_1) + (\dot{m}_{10} s_{10} - \dot{m}_9 s_9) \quad \text{(A-46)}$$

where s_{10} and s_{10} are specific entropy of moist air at absorber inlet and exit respectively and s_{10} and s_{10} are specific entropy of the ionic liquid solutions at absorber inlet and exit

respectively. The specific entropy of moist can be easily found given that we know the temperature and the relative humidity of air and the specific entropy of the IL-solution can be found using the ideal entropy that is used in Flory-Huggins solution theory.

2. Entropy Balance of the Desorber (Heater + Separator)

The desorber (regeneration stage) consists of both the heater and the separator and we calculate the entropy generation of these two components together as a single unit. We assume the heat is supplied at a boundary temperature of T_{heat}, and assume that this boundary temperature is 10 °C greater than the outgoing temperature of the IL-solution from the heater.

$$\dot{S}_{gen,des} = (\dot{m}_8 s_8 + \dot{m}_5 s_5) - \dot{m}_3 s_3 - \frac{\dot{Q}_{reg}}{T_{heat}} \tag{A-47}$$

Where s_3, s_5 and s_8 are specific entropy of are specific entropy of the ionic liquid solutions at heater inlet, IL-rich separator exit, and water-rich separator exit respectively. The specific entropy of the IL-solution can be found using the ideal entropy that is used in Flory-Huggins solution theory.

3. Entropy Balance of the Recuperator

The recuperator is assumed to exchange heat between hot and cold IL-solutions but is adiabatic with the environment. The entropy generation in the recuperator is given by the following equation.

$$\dot{S}_{gen,rec} = \dot{m}_2(s_3 - s_2) + \dot{m}_5(s_6 - s_5) \quad \text{(A-48)}$$

The specific entropies of s_2, s_3, s_4, and s_6 are found using the ideal entropy that is used in Flory-Huggins solution theory given the temperature and concentration of the IL in the IL-solution.

4. Entropy Balance of the Heat Exchanger

The heat exchanger cools the generated IL-rich solution to a low temperature with cooling water. In our model, the cooling water mass flow rate and temperature is calculated. The rate of heat required to cool the IL-solution ($\dot{Q}_{cool}$), is given off to the cooling water. The boundary temperature if at which heat is removed is taken as 10 °C smaller than the temperature of the IL-solution exiting the heat exchanger. The entropy generation is given by the following equation.

$$\dot{S}_{gen,HE} = \dot{m}_6(s_7 - s_6) + \frac{\dot{Q}_{cool}}{T_{cool}} \quad \text{(A-49)}$$

where s_6 and s_7 are specific entropy of the ionic liquid solutions at heat exchanger inlet and exit respectively. They are calculated using ideal entropy that is used in Flory-Huggins solution theory.

5. Entropy Balance of the Makeup IL Mixer

In the mixer, makeup ionic liquid is mixed with the cooled IL-rich solution to makeup for the lost water-rich IL-solution. We assume negligible heat exchange with the

surrounding and therefore the entropy generation equation is given by the following equation.

$$\dot{S}_{gen,Mixer} = \dot{m}_7 s_7 - (\dot{m}_1 s_1 + \dot{m}_{add} s_{add}) \quad \text{(A-50)}$$

where s_1, s_7 and s_{add} are specific entropy of the ionic liquid solutions that are calculated using ideal entropy that is used in Flory-Huggins solution theory.

The total entropy generation for the entire cycle can be obtained by summing the entropy generation for each of the components and is given by the following equation.

$$\dot{S}_{gen,tot} = \dot{S}_{gen,abs} + \dot{S}_{gen,des} + \dot{S}_{gen,HE} + \dot{S}_{gen,rec} + \dot{S}_{gen,Mixer} \quad \text{(A-51)}$$

The entropy generation is calculated for the different input conditions shown in Table A-1 and entropy generation for different components and total entropy generation in the cycle is shown in Table A-2. The first condition is the default condition and the LCST, χ_H and $\Delta T_{reg,exs}$ are changed from the default in condition 2, condition 3 and condition 4 respectively.

Table A-1: Input conditions for the different parameters

Input Condition	$LCST$ (℃)	χ_H (K)	$\Delta T_{reg,exs}$ (℃)	$T_{s,in}$ (℃)	$T_{air,in}$ (℃)	$RH_{air,in}$ (%)	ε_{ma}
1	50	-9000	30	32	30	70	0.8
2	60	-9000	30	32	30	70	0.8
3	50	-5000	30	32	30	70	0.8
4	50	-9000	20	32	30	70	0.8

Table A-2: Entropy generation for different components for the LCST dehumidification cycle

Input Condition	$\dot{S}_{gen,abs}$ (kW/K)	$\dot{S}_{gen,des}$ (kW/K)	$\dot{S}_{gen,HE}$ (kW/K)	$\dot{S}_{gen,rec}$ (kW/K)	$\dot{S}_{gen,Mixer}$ (kW/K)	$\dot{S}_{gen,tot}$ (kW/K)

1	0.0115	0.0265	0.0608	0	9.3×10^{-7}	0.0988
2	0.0114	0.0336	0.0840	0	1.2×10^{-6}	0.1293
3	0.0101	0.0245	0.0667	0	1.0×10^{-5}	0.1013
4	0.0106	0.0179	0.0429	0	4.9×10^{-6}	0.0714

We see in Table A-2 that total entropy generation, increases as the LCST temperature is increased (Condition 1 vs. Condition 2). This means that in order to minimize the losses and increase the efficiency of the cycle, a smaller LCST is preferrable. Similarly, an increase is χ_H (less negative) also increases the total entropy generation and hence an ionic liquid with flatter curvature of the immiscibility curve near LCST is preferred (Condition 1 vs. Condition 3). An examination of Table 6-1 and 6-2 suggests that proper selection of LCST is more important than proper selection of χ_H from an entropy generation point of view. This was also true from an efficiency standpoint in Chapter 2 (Figure 2-9). We do note that while the difference between -9000 K and -5000 K for χ_H yields a relatively small effect on entropy generation, the region between -5000 K and -500 K will likely have a much larger effect (see inset of Figure 2-8c) and corresponded χ_H-ranges in Figure 2-9. Finally, when the excess regeneration temperature ($\Delta T_{reg,exs}$) is decreases from 30 °C to 20 °C, we see a decrease in total entropy generation due to decrease in regeneration temperature and hence reduction in total heat added ($\dot{Q}_{reg}$) in the heater.

A.4. Additional Results

In addition to the two-performance metrics, COP_{deh} and r_{makeup}, another common

metric to evaluate the overall impact of our system on air is thermal coefficient of performance. Thermal coefficient of performance, $COP_{thermal}$ is defined in Equation (A-52). The first term in the numerator denotes the moisture removal from air, which is the primary objective of the dehumidification system. The 2nd term in the numerator represents the sensible heat transfer to/from the air during the absorption process (this is an unintended effect of moisture removal process and depends on the relative temperatures of the air and the desiccant solution). A reduction in air temperature is considered a positive effect and tends to increase the overall $COP_{thermal}$ whereas an increase in air temperature is considered a negative effect and tends to reduce the overall the $COP_{thermal}$.

$$COP_{thermal} = \frac{\dot{m}_{abs} h_{fg} + \dot{m}_9 c_{p,air} (T_9 - T_{10})}{\dot{Q}_{reg}} \quad \text{(A-52)}$$

In the following figures, we have plotted the two types of *COPs* namely dehumidification COP (COP_{deh}) and thermal COP ($COP_{thermal}$). COP_{deh} accounts for only moisture removal from the incoming air whereas the $COP_{thermal}$ takes into the moisture removal as well as sensible heating/cooling on air by the absorber.

Figure A14 show a comparison of COP_{deh} and $COP_{thermal}$ for varying T_{LCST}, χ_{H}, and $\Delta T_{reg,exs}$. In all cases, the $COP_{thermal}$ trends closely follow the COP_{deh}, but with a small offset to the downside. This is because we have fixed our inlet solution temperature, T_1, to be 32 ℃ and this is hotter than the inlet humid air ($T_9 = 30$ ℃). This causes a detrimental

heating effect with respect to $COP_{thermal}$ ($i.e.$, $(T_9 - T_{10})$ in Equation (A-52) is a negative number), and hence $COP_{thermal}$ is slightly less than COP_{deh}.

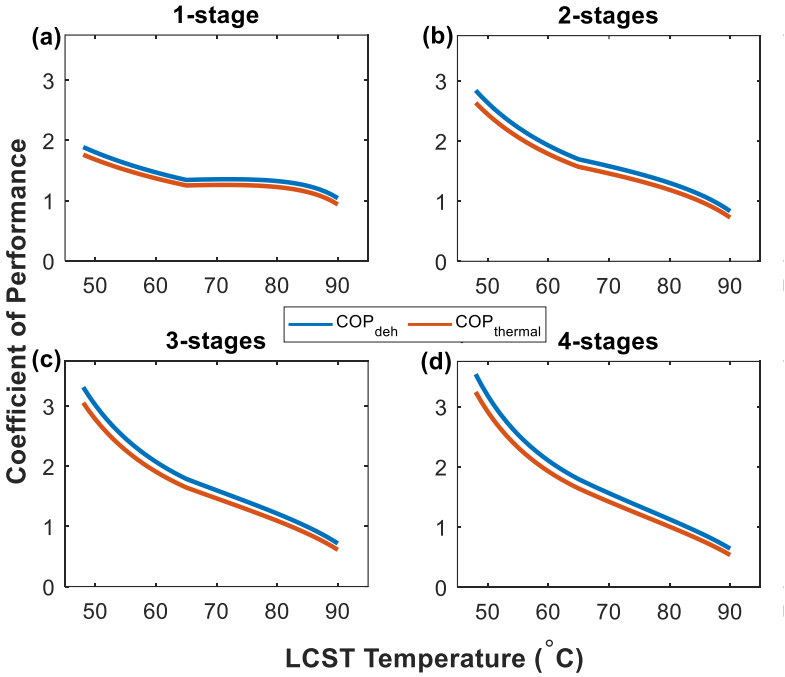

Figure A12: Effect of $LCST$ temperature on coefficient of performance (COP_{deh} and $COP_{thermal}$) when the air temperature at the absorber inlet is 30 ℃ and IL-solution temperature at the absorber inlet is 32 ℃

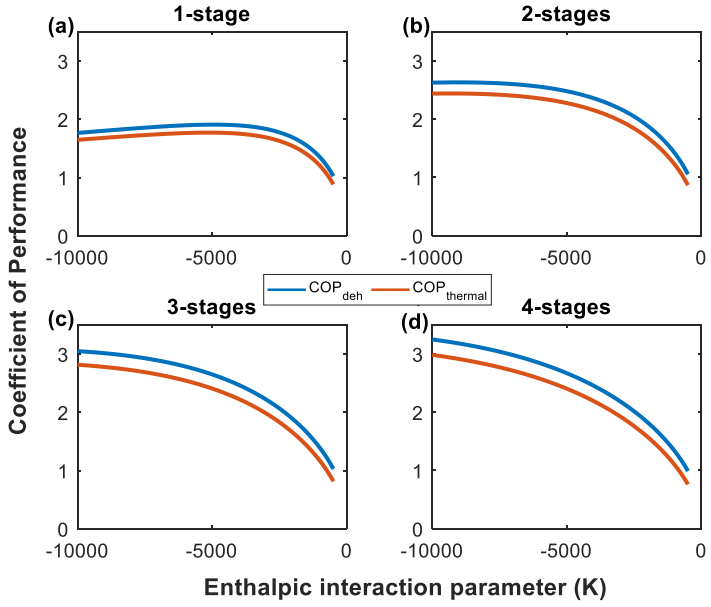

Figure A13: Effect of enthalpic interaction parameter (χ_H) on coefficient of performance when the air temperature at the absorber inlet is 30 ℃ and IL-solution temperature at the absorber inlet is 32 ℃

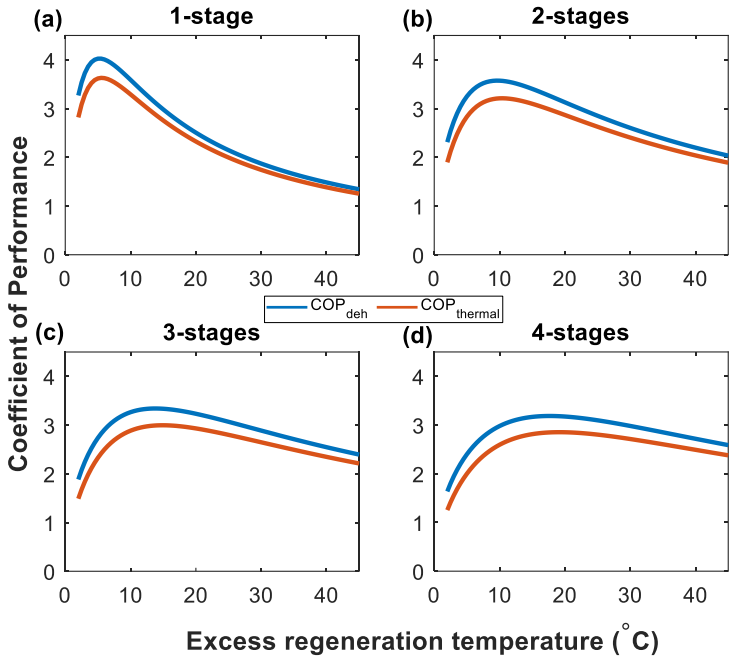

Figure A14: Effect of excess regeneration temperature on coefficient of performance when the air temperature at the absorber inlet is 30 ℃ and IL-solution temperature at the absorber inlet is 32 ℃

APPENDIX B

SUPPORTING INFORMATION FOR CHAPTER 3

B1. Background on Vrentas-Vrentas Model

The absorption behavior of glassy polymers can be modelled using Vrentas-Vrentas model [72]. This model is a modified version of Flory-Huggins theory [61] that works well for absorption by rubbery polymers. The model considers the effects of structural arrangements in the polymer matrix on sorption and volumetric behavior.

The schematic shown in the Figure B1 illustrates mixing of two components during absorption process. The absorption of water into polymer matrix changes the structure of the polymer matrix and it expands on absorption. The glass transition temperature of the polymer-water mixture, T_{gm} is critical in the determining the amount of water that is absorbed. The glass transition temperature of the mixture is determined using Fox equation [74] shown in Equation (B-1). T_{gm} decreases as more water is absorbed.

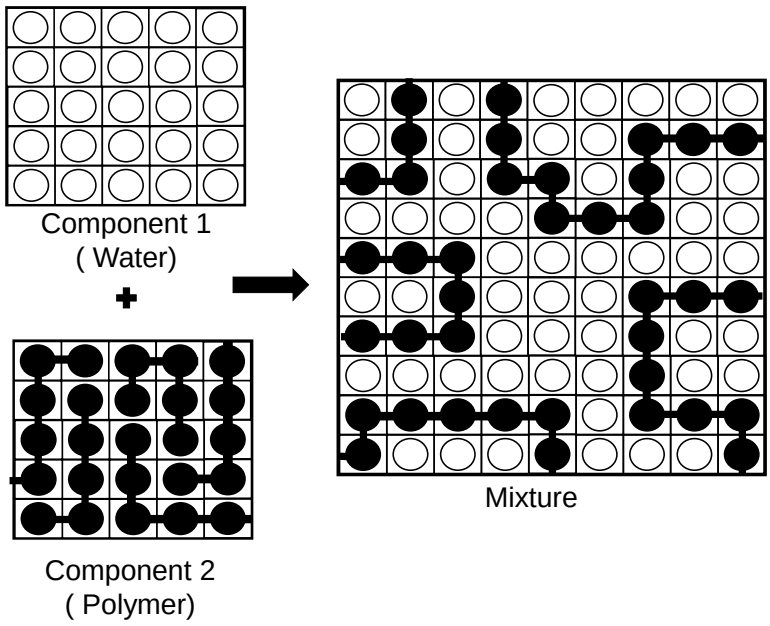

Figure B1: Schematic of the mixing of the polymer and penetrant

$$\frac{1}{T_{gm}} = \frac{\omega_1}{T_{g1}} + \frac{\omega_2}{T_{g2}} \tag{B-1}$$

Assumptions of the Model

The following assumptions are used to formulate a theory for the volumetric and sorption behavior of glassy polymer-penetrant systems:

1. The pure polymer is characterized by four important thermodynamic variables: α_2, α_{2g} , $\hat{c}_p$ and $\hat{c}_{pg}$. Here, α_2 and α_{2g} are the thermal expansion coefficient for the equilibrium liquid polymer and for the glassy polymer respectively. Similarly, $\hat{c}_p$ and $\hat{c}_{pg}$ are the specific heat capacity for the equilibrium liquid polymer and the glassy polymer respectively. Also, the rapid changes in the thermal expansion coefficient and in the specific heat near T_{g2} will be idealized as step changes from α_{2g} to α_2 and from $\hat{c}_{pg}$ to $\hat{c}_p$, at T_{g2}.

The expansion coefficients used in the theory and for the temperature intervals of interest, it is assumed that approximations of the form shown in Equation (B-2)

$$exp\left[\alpha_2\left(T - T_{g2}\right)\right] = 1 + \alpha_2\left(T - T_{g2}\right) \tag{B-2}$$

2. At a given penetrant concentration, the polymer penetrant mixture exists as a nonequilibrium liquid structure at temperatures below T_{gm}. We assume that, once this structure is formed at a given penetrant concentration and temperature, the structure remains effectively invariant during any experiments carried out on the polymer-penetrant mixture until the concentration level is changed. This behavior is analogous to what happens when a pure polymer is cooled below T_{g2}. At some temperature *T* below T_{g2}, the polymer assumes a glassy volume higher than that of the equilibrium liquid polymer at *T,* and this volume relaxes only very slowly toward the equilibrium value for the polymeric liquid.

3. The specific volume, $\hat{V}$, of the equilibrium liquid mixture of polymer and penetrant at a given concentration for a given temperature. For temperature above the glass transition temperature, T_{g2}, and below it Equation (B-3) and Equation (B-4) respectively.

$$\hat{V} = \omega_1 \hat{V}_{1^0} + \omega_2 \hat{V}_2^0 \tag{B-3}$$

$$\hat{V} = \omega_1 \hat{V}_{1^0} + \omega_2 \hat{V}_{2g}^0 \tag{B-4}$$

4. The specific Gibbs free energy of a liquid polymer penetrant mixture, $\hat{G}$, can be expressed as Equation (B-5)

$$\hat{G} = \omega_1 \hat{G}_1^0 + \omega_2 \hat{G}_{2g}^0 + \Delta \hat{G}_m \tag{B-5}$$

Here, $\hat{G}_1^0$ is the specific Gibbs free energy of the penetrant in the liquid state, $\hat{G}_{2g}^0$ is the appropriate specific Gibbs free energy (defined below) of the glassy polymer below T_{gm}. $\hat{V}_2^0$ and $\hat{G}_2^0$ are functions of only temperature and pressure whereas $\hat{V}_{2g}^0$ and $\hat{G}_{2g}^0$ are functions of temperature, pressure and configuration of the polymer matrix. Gibbs free energy of mixing per mass of mixture, $\Delta \hat{G}_m$ at some temperature, T is obtained using Flory-Huggins expression[61] in Equation (B-6).

$$\hat{G}_m = RT \left[\frac{\omega_1}{M_1} ln\, \phi_1 + \frac{\omega_2}{M_2} ln\, \phi_2 + \frac{\chi\, \omega_1 \phi_2}{M_1} \right] \tag{B-6}$$

Where R is the gas constant, ϕ_1 is the volume fraction of component 1 (water in our case), M_1 is the molecular weight of component 1, and χ is the interaction parameter of the Flory-Huggins theory. The parameter χ can be a function of temperature but not of concentration. The mixing term for the Flory-Huggins theory is formulated by assuming that same lattice structure can be used at all concentrations and equilibrium liquid polymer volume is considered. Therefore, the volume fractions of the water and polymer are related to weight fractions as shown in Equation (B-7) and Equation (B-8) respectively.

$$\phi_1 = \frac{\omega_1}{\omega_1 + q\omega_2} \tag{B-7}$$

$$\phi_2 = \frac{q\omega_2}{\omega_1 + q\omega_2} \tag{B-8}$$

Where ω_1 and ω_2 are weight fraction of the water and polymer respectively and q is

the ratio of lattice volume occupied by polymer ($\hat{V}_{2^0}$) and water ($\hat{V}_{1^0}$). It is given by Equation (B-9)

$$q = \frac{\hat{V}_{2^0}}{\hat{V}_{1^0}} \tag{B-9}$$

Sorption Behavior

At sorption equilibrium at constant and uniform temperature and pressure, the following equation must be satisfied by the penetrant (water in our case):

$$\hat{G}_1 = \hat{G}_1^g \tag{B-10}$$

Here, $\hat{G}_1$, is the partial specific Gibbs free energy of the penetrant in the polymer-penetrant mixture and $\hat{G}_1^g$ is the specific Gibbs free energy of the essentially pure gas phase of the penetrant (water vapor in our case) at temperature *T* and pressure p_1.

For ideal gases:

$$\hat{G}_1^g = \hat{G}_1^{g0} + \frac{RT}{M_1} ln\left(\frac{p_1}{p_1^0}\right) \tag{B-11}$$

Where $\hat{G}_1^{g0}$ is the specific Gibbs free energy of gaseous penetrant (Water vapor) at *T* and p_1^0. p_1^0 is taken as reference pressure.

Also, Gibbs free energy of the mixture is given by

$$\hat{G} = \omega_1 \hat{G}_1 + \omega_2 \hat{G}_2 \tag{B-12}$$

Where $\hat{G}_2$ is the partial specific Gibbs free energy of polymer in the mixture

$\hat{G}_1$ can be written from by differentiating the above equation can written as:

$$\hat{G}_1 = \hat{G} + \omega_2 \left(\frac{\partial \hat{G}}{\partial \omega_1}\right)_{T,p_1} \tag{B-13}$$

For a liquid polymer-penetrant mixture (above $T > T_{gm}$), $\hat{G}$ is given by the following expression:

$$\hat{G} = \omega_1 \hat{G}_1^0 + \omega_2 \hat{G}_2^0 + \Delta \hat{G}_m \tag{B-14}$$

Where is the $\Delta \hat{G}_m$ mixing enthalpy of the polymer-penetrant mixture. This is obtained from the Flory-Huggins theory[61,62]:

$$\Delta \hat{G}_m = RT \left[\frac{\omega_1}{M_1} ln\, \phi_1 + \frac{\omega_2}{M_2} ln\, \phi_2 + \frac{\chi\, \omega_1 \phi_2}{M_1}\right] \tag{B-15}$$

Where M_1 and M_2 are the molar masses of the penetrant and polymer receptively and ω_1 and ω_2 are weight fractions of the penetrant and polymer respectively.

Combining the Equations (B-13), (B-14) and (B-15) and assuming that M_2 (polymer molar mass will be much bigger than the water molar mass) is sufficiently large gives:

$$\hat{G}_1 = \hat{G}_1^0(T,p) + \frac{RT}{M_1}\left[ln\, \phi_1 + \phi_2 + \chi\, {\phi_2}^2\right] \tag{B-16}$$

The Equation (B-16) is the result of the Flory-Huggins theory for a rubbery polymer-penetrant mixture. But for Glassy polymer-penetrant mixture ($T < T_{gm}$), the above equation is of the form shown below Equation (B-17). In this case the specific Gibbs free energy of the polymer depends on the concertation of the penetrant in the mixture.

$$\hat{G}_1 = \hat{G}_1^0(T,p) + {\omega_2}^2 \left(\frac{\partial \hat{G}_{2g}^0}{\partial \omega_1}\right)_{T,p_1} + \frac{RT}{M_1}\left[ln\, \phi_1 + \phi_2 + \chi\, {\phi_2}^2\right] \tag{B-17}$$

The only difference between the Equation (B-16) and Equation (B-17) is the dependence of $\hat{G}_{2g}^{0}$ on ω_1. $\hat{G}_{2g}^{0}$ may be written as shown below in Equation (B-18)

$$\hat{G}_{2g}^{0} = \hat{G}_{2}^{0} + (\hat{c}_{pg} - \hat{c}_{p})\left[\left(T - T_{gm}\right) - T\ln\left(\frac{T}{T_{gm}}\right)\right] \tag{B-18}$$

The first derivative of the $\hat{G}_{2g}^{0}$ can then be written as,

$$\left(\frac{\partial \hat{G}_{2g}^{0}}{\partial \omega_1}\right)_{T,p_1} = (\hat{c}_{pg} - \hat{c}_{p})\frac{dT_{gm}}{d\omega_1}\left(\frac{T}{T_{gm}} - 1\right) \tag{B-19}$$

Substituting this equation in Equation (B-17) gives:

$$\begin{aligned}\hat{G}_1 = \hat{G}_1^{0}(T,p) + {\omega_2}^2(\hat{c}_{pg} - \hat{c}_{p})\frac{dT_{gm}}{d\omega_1}\left(\frac{T}{T_{gm}} - 1\right) \\ + \frac{RT}{M_1}\left[ln\,\phi_1 + \phi_2 + \chi\,{\phi_2}^2\right]\end{aligned} \tag{B-20}$$

From usual thermodynamics relations, we know that

$$\hat{G}_1^{0}(T,p) = \hat{G}_1^{0}(T,p_1^{0}) + \hat{V}_1^{0}(p_1 - p_1^{0}) \tag{B-21}$$

Where $\hat{V}_1^{0}$ is the specific volume of the penetrant. The second term in the above equation may be ignored because its contribution is very small. Hence the above equation can be written as Equation (B-22):

$$\hat{G}_1^{0}(T,p) = \hat{G}_1^{0}(T,p_1^{0}) = \hat{G}_1^{g0} + \frac{RT}{M_1}\,ln\left(\frac{p_1}{p_1^{0}}\right) \tag{B-22}$$

Combination of the all the above equations leaves us with the absorption isotherm equation for a glassy polymer show in Equation (B-23)

$$\phi_1 \, exp\left(\phi_2 + \chi {\phi_2}^2 + F\right) = \frac{p_1}{p_1^0} \tag{B-23}$$

$$F = M_1 \omega_2^2 \left(c_{pg} - c_p\right) \left(\frac{\mathrm{d}T_{gm}}{\mathrm{d}\omega_1}\right) \left(\frac{T}{T_{gm}} - 1\right) / RT \tag{B-24}$$

F parameter accounts for elastic energy stored in the polymer during absorption. Clearly $F = 0$ at $T = T_{gm}$ and $F < 0$ for $T < T_{gm}$. For rubbery polymers ($T > T_{gm}$), $F = 0$ and the above equation is reduced to given by Flory-Huggins theory.

Glassy temperature of the polymer water mixture, T_{gm} is determined using Fox equation[63]:

$$\frac{1}{T_{gm}} = \frac{\omega_1}{T_{g1}} + \frac{\omega_2}{T_{g2}} \tag{B-25}$$

From Equation (B-24), we can write the differential as shown below in Equation (B-26)

$$\frac{\mathrm{d}T_{gm}}{\mathrm{d}\omega_1} = {T_{gm}}^2 \left(\frac{1}{T_{g2}} - \frac{1}{T_{g1}}\right) \tag{B-26}$$

APPENDIX C

SUPPORTING INFORMATION FOR CHAPTER 4

Governing Equations for Absorption/ Regeneration Process in COMSOL.

C1. Heat Transfer

The unit cells consist of three types of materials- (i) Solid which consists of outer casing which is assumed to be made of the stainless steel and aluminum sheet on which the polymer film is grown. (ii) Porous material consists of only polymer film and (iii) moist air that flows through the air gap. The heat equations associated with different materials assume slightly different forms which are explained in the following subsections.

1.1. Heat Transfer Equations in Solid

The heat equation for heat transfer in solids is given by the following equation. In the equation, ρ_s is the density of the solid, $c_{p,s}$ is its density and k_s is its thermal conductivity. The source term is 0 because there is no heat generation within the volume.

$$\rho_s c_{p,s} \frac{\partial T}{\partial t} - \nabla \cdot (k_s \nabla T) = 0 \tag{C-1}$$

The boundary conditions and the assumptions for solid are as follows:

1. In the unit cell, periodic boundary conditions are applied as shown in Equation (4-1). In the equation, L/2 is the half-length of the unit cell.

$$T_{x=-L/2} = T_{x=L/2} \tag{C-2}$$

2. There is the convective heat flux at applied at the top of casing by cooling fluid (water) at temperature T_{cf} given by thet following equation where H is the height of the unit cell.

$$q'' = h(T - T_{cf}) \text{ at y = 0 and z = H} \quad \text{(C-3)}$$

3. The interface between the steel casing the aluminum sheet is modelled by setting layer conductance to $h_{cont,metal}$ =1000 W/m^2-K which is typical value for two metal contact that are machined well. Similarly for aluminum sheet and the polymer interface a typical value for layer conductance between a metal and polymer was used and the set to 100 W/m^2-K.

1.2. Heat Transfer Equation for the Polymer (Porous Medium) Film

The heat transfer within the polymer film is governed by the following equation for a porous medium.

$$\left(\rho c_p\right)_{eff} \frac{\partial T}{\partial t} + \rho_w c_{p,w}(\vec{u}.\nabla T) - \nabla \cdot \left(k_{eff} \nabla T\right) = Q_s \quad \text{(C-4)}$$

In the above equation, $\left(\rho c_p\right)_{eff}$ is the effective the heat capacity of the combined polymer matrix consisting of the polymer and the absorbed water and is given by Equation (C-5) where ϕ_s is solid volume fraction, ε_p is porosity of the polymer and ρ_s and ρ_w far ethe respectively the densities and the $c_{p,s}$ and $c_{p,w}$ are specific heat capacity of polymer and water respectively. Similarly, the effective thermal conductivity is given by Equation (C-6) where k_s and k_w are the thermal conductivity of the polymer and the water respectively.

The second term in the above equation is the advection term *i.e.* heat transfer due to

the movement of the water inside the polymer film. The contribution from this term is almost negligible because heat transfer happens time constant is many orders of magnitude bigger than the mass transfer time constant and hence it can be neglected.

The source term on the right-hand side comes from water vapor condensation process in the polymer during absorption as shown in Equation (C-7) where is L_v is the latent heat of vaporization (J/kg), and the G_{evap} (kg/m^3-s) is the moisture absorption rate per volume. This term comes from the mass transfer module. G_{evap} is a function of the volume fraction of the solid polymer, ϕ_s.

$$\left(\rho c_p\right)_{eff} = \phi_s \rho_s c_{p,s} + \varepsilon_p \rho_w c_{p,w} \tag{C-5}$$

$$k_{eff} = \phi_s k_s + \varepsilon_p k_w \tag{C-6}$$

$$Q_s = L_v G_{evap} \tag{C-7}$$

So, the unknown in the above equations are velocity vector $\vec{u}$, volume fraction of polymer, ϕ_s and temperature, T. These parameters are obtained by solving the coupled fluid flow, heat transfer and the mass transfer equations in COMSOL Multiphysics.

The boundary conditions the polymer-aluminum sheet is applied by using the layer conductance for the interface the as explained in the previous section. On the other side, polymer is left to interact with moist air.

1.3. Heat Transfer Equations for Moist Air

The heat transfer Equations for moist air is given by the following equation.

$$\rho_{ma} c_{p,ma} \left(\frac{\partial T}{\partial t} + \vec{u}.\nabla T \right) + \nabla \cdot (-k_{ma} \nabla T) = Q_p + Q_H + Q_{vd} \quad \text{(C-8)}$$

In the above equation, ρ_{ma}, $c_{p,ma}$ and k_{ma} are density, specific heat capacity, and the thermal conductivity of the moist air. They each are a function of atmospheric pressure, temperature, water vapor concentration in air (c_v) and the individual properties of dry air and water vapor. Hec they can be written as in the following equations.

$$\rho_{ma} = f(\rho_a, \rho_v, T, p_A, c_v) \quad \text{(C-9)}$$

$$c_{p,ma} = f(c_{p,a}, c_{p,v}, T, p_A, c_v) \quad \text{(C-10)}$$

$$k_{ma} = f(k_a, k_v, T, p_A, c_v) \quad \text{(C-11)}$$

The first term on the RHS is the work done by pressure changes and is the result of heating under adiabatic compression as well as some thermoacoustic effects. For low Mach numbers, it tends be a small. It can be written as shown in Equation (C-12) where p is pressure and the $\vec{u}$ is the velocity vector.

The 2nd term accounts for the thermal enthalpy change in moist air due to the diffusion of water vapor in air and can be written as shown in Equation (C-13). In the equation $c_{p,a}$ and the $c_{p,v}$ are specific heat capacity of the dry air and water vapor respectively. And g_w (kg/m^2-s) is the diffusion heat flux that can be obtained by coupling with the mass transfer module. The 3rd term on the RHS is the heat generation due to viscous diffusion (Q_{vd}) is ignored in the interest of the simplifying the equation and that it is negligible compared to the other terms.

$$Q_p = \frac{\partial p}{\partial t} + \vec{u}.\nabla p \tag{C-12}$$

$$Q_H = -(c_{p,v} - c_{p,a}) g_w.\nabla T \tag{C-13}$$

Boundary conditions:

1. Initial temperature of the polymer and air is set at $T_{air,ini}$ = 25 °C, at t < 0.

2. Inlet temperature of air at the inlet, T_{air} = 35 °C, at z = 0, x=x, y=y;

3. Periodic boundary conditions: $T_{x=-L/2} = T_{x=L/2}$

C2. Mass Transfer

2.1. Mass transfer in air

The mass transfer equation governing the water vapor in moist air given by the following equation.

$$\rho_g \frac{\partial \omega_v}{\partial t} + \rho_g \vec{u}.\nabla \omega_v + \nabla \cdot \vec{g}_w = G \tag{C-14}$$

Where $\vec{u}$ is the velocity filed for air, $\vec{g}_w$ (kg/m^2-s) is the water vapor mass flux (analysis to heat flux in heat transfer) which can further be expanded to shown in Equation (C-15). In this equation ρ_g is density of the vapor phase, D_a- water vapor diffusivity in air and ω_v is mass fraction of moisture in air. ω_v can be further written in terms of the molecular mass of the water (M_v), relative humidity (RH), gas phase density (ρ_g) and saturation water vapor concentration in air (c_{sat}).

$$\vec{g}_w = -\rho_g D_a.\nabla \omega_v \tag{C-15}$$

$$\omega_v = \frac{M_v(\phi_w c_{sat})}{\rho_g} \tag{C-16}$$

Where D_a- is moisture diffusivity in air, ρ_g is density of the vapor phase, ω_v is mass fraction of moisture in air, ϕ_w is relative humidity, c_{sat} is saturated water concentration in air, M_v is molar mass if water.

G (kg/m^3-s) in Equation (C-14) is the source term for moisture source or sink

2.2. The Mass Transfer for Water within the Porous Polymer

The polymer is treated as porous polymer, mass transfer equation for which is given by the following Equation (C-17). It is assumed that atmospheric pressure around the polymer film is constant and the vapor ($\boldsymbol{u_g}$) and liquid velocity ($\boldsymbol{u_l}$) within the polymer are small and those terms can be neglected.

$$\frac{\partial w(\phi_w)}{\partial t} + \rho_g \boldsymbol{u_g} \cdot \nabla \omega_v + \nabla \cdot g_w + \boldsymbol{u_l} \cdot \nabla \rho_l + \nabla \cdot g_{lc} = G \tag{C-17}$$

The modified equation is then shown below in Equation (C-18)

$$\frac{\partial w(\phi_w)}{\partial t} + \nabla \cdot g_w + \nabla \cdot g_{lc} = G \tag{C-18}$$

In the above equation, $w(\phi_w)$ (kg/m^3) is the moisture storage function which depends on the temperature and the relative humidity surrounding the polymer. This term is an input to COMSOL and basically another form of isotherm of the polymer.

g_w is vapor flux within the polymer and is given by Equation (C-19) In this equation, ρ_g is the moist air density, D_{eff} (m^2/s) is the effective vapor diffusion coefficient in the porous

medium, computed from the diffusion coefficient in a free medium, and accounting for the porosity and tortuosity of the porous medium. ω_v is the vapor mass fraction in moist air

$$\vec{g}_w = -\rho_g D_{eff} \nabla \omega_v \tag{C-19}$$

Similarly, g_{lc} is liquid water flux which is shown in equation (C-20). In the equation D_w (m^2/s) is the moisture diffusivity in the polymer

$$\vec{g}_{lc} = -\frac{\partial w(\phi_w)}{\partial \phi_w} D_w \nabla \phi_w \tag{C-20}$$

The right-hand side term is the moisture source term. In the absence of the any other moisture source, this just becomes a source term due to the evaporation/condensation.

$$G_{evap} = -\frac{\partial w(\phi_w)}{\partial \phi_w} D_w \nabla \phi_w \tag{C-21}$$

The corresponding latent heat source term is then given by the following equation. This can be used in the heat transfer equation.

$$Q_{evap} = L_v G_{evap} \tag{C-22}$$

C3. Fluid Flow

The moist air flow through the channel is given by the following equations. The first equation is the continuity equation shown in Equation (C-23). Where ρ_{ma} is the moist air density, and $\vec{\boldsymbol{u}}$ is the velocity field for the fluid.

$$\frac{\partial \rho_{ma}}{\partial t} + \nabla \cdot (\rho \vec{\boldsymbol{u}}) = 0 \tag{C-23}$$

The second equation shown below is the momentum equation (Navier -Stokes equation)

that describes moist air flow through the channel.

$$\rho_{ma}\frac{\partial \vec{u}}{\partial t} + \rho_{ma}(\vec{\boldsymbol{u}}.\nabla\vec{\boldsymbol{u}}) = -\nabla p + \mu\nabla^2\vec{\boldsymbol{u}} + \boldsymbol{f}] \quad \text{(C-24)}$$

Where μ is the viscosity of moist air, $\vec{\boldsymbol{u}}$ is its velocity field, ∇p represents pressure gradient, $\mu\nabla^2\vec{\boldsymbol{u}}$ represents the viscous forces in the fluid and $\boldsymbol{f}$ represents any external body force such as gravity which has been ignored in this case.

Boundary conditions and assumptions:

1. There is no body force acting on the fluid, *i.e.* $\boldsymbol{f}$ = 0.

2. Initial boundary conditions at $t < 0$, u_x = 0, u_y = 0, u_z = 0

3. The inlet boundary conditions is set for the velocity, at u_x = 0, u_y = 0, u_z = -1 m/s

4. At walls, no slip boundary conditions is applied, u_{wall} = 0.

5. Periodic boundary conditions at x = -L/2 and x=L/2 => $u_{x=-L/2}$= $u_{x=L/2}$

C4. Solid Mechanics

The absorption of moisture can cause deformation in the polymer. The deformation (swelling /shrinking) is modelled using the following equation.

$$\epsilon_{hs} = \beta_h M_{H_2O}\left(c_{mo} - c_{mo,ref}\right) \quad \text{(C-25)}$$

Where ϵ_{hs} - hygroscopic strain which can be converted to displacement. The displacement equation can then be written as the following Equation (C-26). In the equation s_t is the position of the polymer at any given time t and s_0 is the initial position of the polymer.

$$\frac{s_t - s_0}{s_0} = \epsilon_{hs} \tag{C-26}$$

M_{H_20}- molar mass of water (kg/mol),

c_{mo} – moisture concentration in polymer matrix (mol/m^3) at any given time. It is determined from the mass transfer module.

$c_{mo,ref}$- reference moisture concentration (mol/m^3). This is the often taken as 0 when the polymer has not observed aby water and it is completely dry

β_h is hygroscopic coefficient (m^3/kg). It is dependent on the polymer and its hygroscopic nature. For us β_h is the determined by the Vrentas-Vrentas model. Vrentas-Vrentas model gives use the volume fraction of water in the polymer matrix ($\phi_{1\infty} = \frac{V_{1\infty}}{V_{2\infty}}$) which can be converted to the hygroscopic coefficient. The Equation (C-27) below shows how β_h is related to volume fraction, $\phi_{1\infty}$. It must be noted that we calculated with the saturated volume fraction and use that constant value and not the dynamic value that would change for different times.

$$\beta_h = \frac{V_{1\infty}}{m_{2\infty}} \rho_2 = \phi_{1\infty} \tag{C-27}$$

Assumptions and boundary conditions:

1. The area of the polymer film in contact with aluminum substrate is fixed and undergoes no deformation.

2. Only the surface exposed to air is undergoing deformation (swelling/shrinking).